Title
Parametric Oscillation and Microwave Optomechanics with cm-sized SRF Cylindrical Cavities

Author
Martinez, Luis Alberto

Publication Date
2014

Peer reviewed|Thesis/dissertation

Parametric Oscillation and Microwave Optomechanics with cm-sized SRF Cylindrical Cavities

Luis A. Martinez
School of Natural Science
University of California Merced

A thesis submitted for the degree of
PhilosophiæDoctor (PhD), Physics

2014 August

The Dissertation of Luis A. Martinez is approved by:

1._____

Professor Jay Sharping

2. _____

Professor Michael Scheibner

3._____

Professor Boaz Ilan

Signature from Chair of Ph.D committee: _____

Professor Kevin Mitchell

Signature from Ph.D advisor: _____

Professor Raymond Chiao

Day of the defense: Friday August 8, 2014

Abstract

Parametric devices have become a stepping stone in our development of modern technology and new scientific discoveries. They play a role in making astronomical observations with the use of parametric amplifiers as high-sensitivity low-noise first stage amplifiers, or in modern communications as amplifiers of optical frequency light. In addition, parametric devices have been successfully implemented in optomechanics to "cool" or "heat" mechanical motion. In fact, with such systems it has been possible to "cool" the motion of a mirror down to its quantum ground state [1], which is the lowest state of motion obtainable due to the quantum limit. The most common systems of the time consist of optical systems using optical cavities and fiber optics, or micro systems using planar superconducting strip resonators. In this dissertation parametric devices with cm-scaled RF cavities and oscillators are considered. The approach is to show that the same underlying effects that exist in optical systems also exist in with microwave cavities, and with the development of high-Q superconducting RF cavities feasible threshold for parametric effects are obtainable.

Dedicated to my family; Ana Anaya-Martinez, Rogelio Martinez, Zuly Tello, Anita Martinez, Johanna Gomez, Hector and Delia Estrada, Guillermo and Guadalupe Jimenez, Hector, Adrian, Lawrence, and Serena Estrada, and Antonia and Armando Martinez for their unconditional support, motivation, inspiration, and above all, their patience during my long educational journey. Finally, and most importantly I dedicate this to my daughter Hailey I Martinez, whose curiosity and imagination is a beautiful proof of the natural origin of science.

Acknowledgements

I would like to express my deepest gratitude to my mentor and advisor, Professor Raymond Chiao, who has thought me the essence of physics. In addition to teaching me "the way of the physicist", he has been an incredible source of knowledge, support, inspiration, and encouragement during my studies.

I would also like to acknowledge Professors Jay Sharping, Kevin Mitchell, Boaz Ilan, Michael Schiebner, my friends and colleagues, specially Mark Kerfoot, Al Castelli, Robert Haun, Bong Soo Kang, Nathen Inan, Xiuhoa Deng, Stephen Minter, Carrie King, Elyse Ozamoto, Stephanie Stepp, Tony Van Ryte, Diana Lizarraga, the Graduate division, and the University of California Merced. Finally, I would also like to give a special thanks to Mr. Ernesto Limon and his family for the continual support.

Contents

List of Figures

LIST OF FIGURES

1

Introduction

1.1 Mechanical Oscillators

As an example of a mechanical oscillator take a pendulum in which a massive bob is attached to the end of a string that is hung vertically. A small deflection away from the equilibrium position causes a restoring force that opposes the displacement of the bob. The pendulum will oscillate at a natural frequency that is related to the gravitational force and mass of the bob. In general the physical mechanism behind this oscillation follows from Hooke's law where the size of the restoring force is proportional to the displacement from equilibrium. In the absence of damping the pendulum is better known as a simple harmonic oscillator that in principle would oscillate perpetually. In this sense the essence of a mechanical oscillator lies in the existence of a restoring force when it is displaced from its equilibrium position, and natural characteristic frequency of oscillation which in general is related to the ratio of the stiffness and mass of the oscillator.

Given our definition of a mechanical oscillator it is easy to see that many examples of mechanical oscillators or mechanical resonators exist. The relevant question then becomes how "good" of a mechanical oscillator is it? In particular, what parameters make a mechanical oscillator a "good" one? Although the specifications for these parameters may vary by application, we desire general parameters which allow for a comparison among different mechanical oscillators. With this in mind, the important parameters of any mechanical oscillator are 1) its natural resonant frequency of oscillation, and 2) the quality factor of the resonator. The quality factor is a general measure of how

well an oscillator oscillates. For example, suppose one excites a mechanical oscillator and decides to measure how long it takes for the oscillator to stop oscillating. If the oscillator takes an extremely long time to stop oscillating relative to the time it takes the oscillator to complete one cycle, then we can say it has a high quality factor (Q). In contrast, if the oscillator stops shortly after a few cycles then we can say it has a low or poor quality factor. This is the basic idea behind the quality factor, and it basically is a measure of how many times the oscillator will oscillate relative to its natural frequency.

Recently is has been realized that mechanical oscillators play an important role in the study of fundamental quantum processes. In particular, systems coupling electromagnetic fields with mechanical oscillators have become a platform for exploring quantum mechanics, parametric amplifiers and oscillators, phononic, and nanomechanical systems [2, 3, 4, 5, 6, 7, 8, 1, 9, 10, 11]. These applications and scientific breakthroughs outline the importance of high-Q high-frequency mechanical oscillators and have pushed forward the development for more sophisticated mechanical oscillators.

1.2 Parametric Oscillators and Optomechanics

In general a parametric oscillator is a device that can amplify or generate existing or new degrees of freedom by the transfer of energy from an external source which is usually denoted as the pump. To best illustrate this concept, lets us consider the classic example of a child on a swing[1]. First, note that the swing is a mechanical oscillator with a natural resonance that depends on the length of the swing. Suppose that initially the swing's amplitude of oscillation is zero [2]. We now ask how can the child get the swing to oscillate? The obvious answer is for someone else to give him a push. In this case, the person pushing the child would give a small kick at a frequency which is equal to the resonant frequency of the swing. Indeed, in this case is nothing more than the typical driving of the swing at resonance, or more formally known as a driven harmonic oscillator.

[1] The reader should be warned that this analogy has been questioned as to whether a child-swing system is really a parametric oscillator [12]. The modeled used in [12] leads to the conclusion that the child-swing system is primarily a driven oscillator with negligible parametric terms. However, a more appropriate model in which the length of the swing varies sinusoidally leads to the correct analogy [13].

[2] If you have a hard time seeing this, you can picture a minute amplitude of oscillation, but it takes away from the main point of parametric oscillation.

To parametrically oscillate the swing imagine now that the child begins to squat and stand on the swing at a frequency that is twice the natural resonance frequency of the swing. Effectively the child's motion will begin to modulate the length of the swing which in turn will modulate its resonant frequency. When the child's repetitive squatting and standing motion reaches a particular amplitude the swing will begin to oscillate; as the child continues this motion the swing's oscillation amplitude will grow exponentially, and parametric oscillation is achieved. In light of this, we say that the frequency at which the child squats and stands is the pump frequency, and the frequency of the swing's motion is the signal frequency. The minimum amplitude of oscillation of the child's motion required to begin oscillation of the swing is the called the threshold.

The example above for the degenerate parametric amplifier highlights some of the important characteristics of parametric oscillators. In particular, a modulation above the threshold condition of a specific physical parameter, such as the resonance frequency, is required to achieve parametric oscillation. In practice, modulation can effectively be achieved by introducing non-linear elements. For example, in optical systems non-linear fiber optics introduce a modulation of the refractive index which is dependent on the intensity of the pump beam. In electrical systems parametric oscillation can be achieved by varying the capacitance or inductance of an electrical circuit. Finally, we add that parametric oscillators/amplifiers play an important role in many areas of physics. For example, in optics parametric devices can lead to frequency conversion processes in which a pump signal is used to generate optical sidebands [14], or in electronics where parametric amplification can be used create to low noise amplifiers [15]. It is of our interest to create a superconductive microwave cavity parametric oscillator that can generate microwaves from vacuum fluctuations as will be discussed.

The field of optomechanics uses the radiation pressure of light to control the motion of mechanical oscillators. The motion of mechanical oscillators can be "heated" or "cooled" via the interaction with light under proper conditions. In particular, when light reflects from a moving boundary (e.g., a mirror) energy is transferred, due to the de-acceleration (friction) of the boundary, to the reflected light. This energy transfer leads to the concept that light creates friction on the moving boundary (the *friction of light*), and in the process energy is transferred from the boundary to the reflected light. In a more practical view, the effect can be seen to originate from the Doppler frequency

shift experienced by the the re-radiated light at the moving boundary. Furthermore, if the motion of the boundary is harmonic in time, the reflected light will consist of a pair of sidebands; one with slightly higher frequency, and one with slightly lower frequency. One can then imagine that in a similar fashion, due to time reversal symmetry, energy can be extracted from the light and imparted into the moving boundary. Hence, the possibility to push ("heat") or slow ("cool") the motion of the boundary exist. The combination of the effect of the *friction of light* with high quality resonant cavities leads to a large enhancement of the interaction. This mechanism has been successfully implemented in optical microcavity optomechanics to cool the motion of a mechanical oscillator down to its ground state, which corresponds to the quantum limit for the motion of the oscillator [1]. Alternatively, this mechanism can also be used to parametrically amplify the motion of the oscillator, a process that has been coined with the name of *parametric instability* [16].

1.3 Purpose of this Dissertation

Our ultimate goal is to develop a superconductive microwave cavity parametric oscillator for microwaves that can have potential experimental applications in the detection and generation of gravitational waves as described in [17, 18]. Given the complexity and technical challenges involve in the completion of this project we do not expect that this thesis will address all the issues that will surely arise along the way. Instead this thesis will focus on preliminary work towards that goal, including theoretical, technical, and experimental milestones. The main purpose being to establish a convincing and motivating start of this project.

2

Parametric Oscillator

This chapter develops the main idea behind the proposed microwave parametric oscillator. It begins with a short physical description of the underlying mechanism for the proposed oscillator. In section 2.2 the transient solution for a Fabry-Perot is derived. Section 2.3 outlines the method for calculating the frequency splitting in the double Fabry-Perot. The solution for the threshold of oscillation is presented in section 2.4. Finally, a remark is made on the feasibility of achieving an effective high-Q high-frequency mechanical oscillator in section 2.5

2.1 Motivation

Parametric oscillators for generating electromagnetic microwaves might be possible, based upon the idea that a moving mirror is like a moving piston that can perform work *nonadiabatically* on radiation contained within a cavity. Above a certain threshold, the parametric action of the moving mirror will exponentially amplify this radiation until it can become a large-amplitude, classical wave [17].

Consider the opto-mechanical configuration sketched in figure 2.1 [17], in which a laser beam from the right is incident on a moving mirror (e.g., a flat SC mirror with a multilayer dielectric optical coatings deposited on its right side). When this moving optical mirror is combined with a fixed optical mirror in an optical Fabry-Perot-cavity configuration, a production of Doppler sidebands will arise which can then be utilized either for the laser cooling of the moving mirror by means of a *red-detuned* laser tuned to the lower Doppler sideband [19], or for the parametric oscillation of the moving

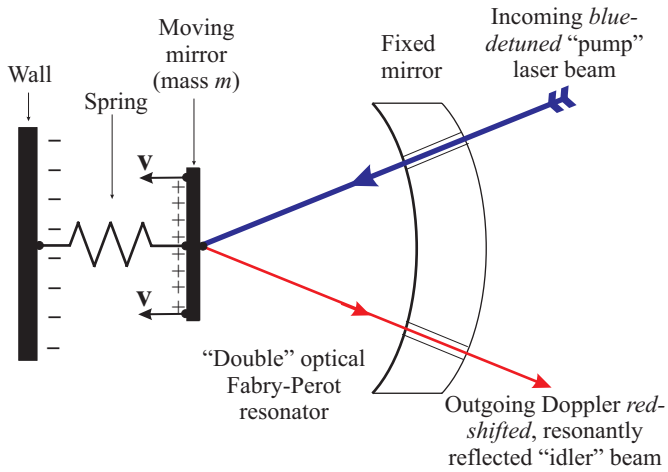

Figure 2.1: Simplified model of a triple cavity microwave parametric amplifier. The left side consist of a high Q superconducting RF cavity, while the right side is a Fabry-Perot resonator with two resonances.

mirror excited in an elastic mode at acoustical frequencies by means of a *blue-detuned* laser tuned to the upper Doppler sideband [16, 20]. Above the threshold for parametric oscillation of the moving mirror within the SC resonator, a "signal" wave begins to build up, growing exponentially with time, starting from the injected "seed" microwave radiation. However, once parametric oscillation above threshold occurs, one could turn off the source of the "seed" radiation, and the SC resonator would then continue to oscillate as an autonomous source of the same microwaves.

In a simple quantum picture the incoming pump photon is Doppler shifted by the moving mirror. When the pump photon of energy $\hbar\omega_p$ is red-shifted to $\hbar\omega_i$ upon reflection from the moving mirror, the energy lost by the pump photon $\Delta E = \hbar(\omega_i - \omega_p) < 0$ must be gained by the moving mirror. This example illustrates the fundamental process underlying parametric amplification of the moving mirror. Similarly this also holds for the blue-shifted photon. In this case, the exiting photon gains energy $\Delta E = \hbar(\omega_i' - \omega_p) > 0$, which may lead to parametric cooling as energy must be extracted from the moving mirror. Both cases have been well studied and experimentally verified, see [16, 20, 21] and references there-in.

Chiao et. al. have proposed a scheme for the parametric amplification of microwaves using a microwave SC cavity in conjunction with a "Double" optical Fabry-Perot resonator, see figure 2.2 [17]. In this scheme a SC microwave cavity is coupled to an optical "Double" Fabry-Perot resonator via a charged mechanical membrane (pellicle). The

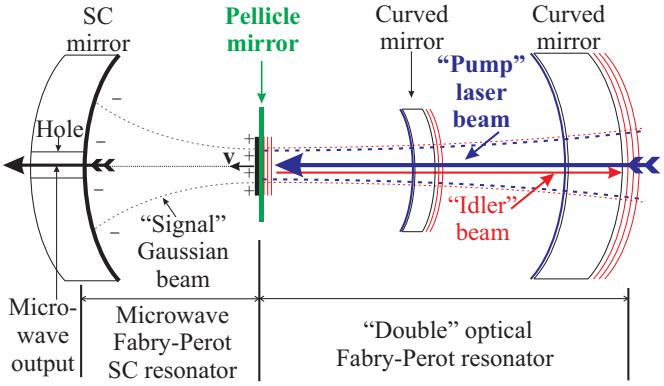

Figure 2.2: Double Fabry-Perot coupled to a microwave cavity via a mechanical membrane coated with a SC Nb film. The left sides acts as a effective high-Q mechanical oscillator at GHz frequency. The right side is tuned to excite the membrane into motion parametrically as discussed in the text.

microwave cavity couples to the mechanical charged membrane in a way that effectively enhances the Q of the mechanical resonator. In this sense, the left side of figure 2.1 is effectively realized. The "Double" optical Fabry-Perot resonator on the right hand side, which is depicted in more detail in figure 2.3, can simultaneously resonate both the strong, incoming *blue-detuned* laser (i.e., the "pump" laser) and the weak, Doppler red-shifted "idler" light wave produced upon reflection from the moving mirror, but it also serves as a rejection filter to reject any undesirable Doppler blue-shifted (or "anti-Stokes") light.

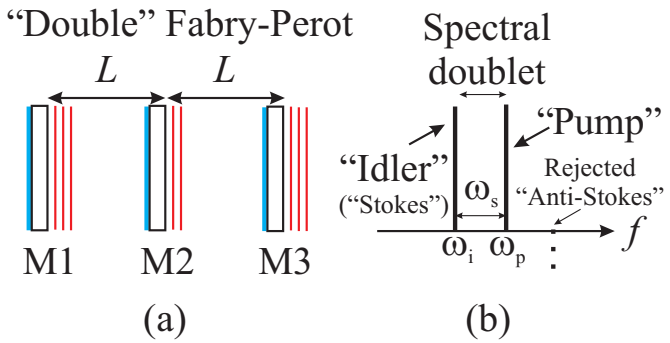

Figure 2.3: Detail schematic of the triple Fabry-Perot Microwave system proposed as a microwave parametric amplifier.

2.2 "Charging" and "Discharging" of a Fabry-Perot Resonator

We solve for the time dependent electric field amplitude in a Fabry-Perot resonator of length L consisting of two mirrors with reflection coefficients r_1 for the left mirror and r_2 for the right mirror. To avoid confusion with the time variable t we denote the transmission coefficient as $\mathcal{T}$. Let E_P be an right traveling incoming plane wave so that it enters the FP through the left mirror defined as the $x = 0$ point,

$$E_P(x = 0, t) = E_{0P} e^{-i\omega t}, \tag{2.1}$$

where E_{0P} is a constant amplitude, and ω is the frequency of the field. Let us denote the internal right traveling field at the left mirror by E_1^+ which can be expressed by

$$E_1^+(x = 0, t) = E_{01}^+ e^{-i\omega t}. \tag{2.2}$$

A general recursion relation can be made from the right traveling field at the left mirror. The internal right traveling field at the left mirror at any given time is related to the incident incoming external beam at that time and the previous field in the FP a round trip earlier. The propagating factor P_f accounts for the proper phase shift gained by the field that has undergone one round trip. This phase shift is due to the traveled path and is related to the length of the cavity. The recursion relation is

$$E_1^+(t + \tau) = \mathcal{T} E_P(t + \tau) + r_1 r_2 P_f E_1^+(t), \tag{2.3}$$

where r_1 and r_2 account for the fact that the beam has reflected from both mirrors once, $\mathcal{T}$ account for the transmission of the incoming external beam, and the propagation constant for one round trip is

$$P_f = e^{2ikL - \omega\tau}. \tag{2.4}$$

With the above definitions for the electric fields equation (2.3) becomes

$$E_{01}^+(t + \tau) = \mathcal{T} E_{0P} + r_1 r_2 e^{2ikL} E_{01}^+(t). \tag{2.5}$$

Because the round trip time $\tau = 2L/c$ is a small quantity we can expand the left hand side

$$E_{01}^{+}(t) + \tau \frac{d}{dt} E_{01}^{+}(t) = \mathcal{T} E_{0P} + r_1 r_2 e^{2ikL} E_{01}^{+}(t). \tag{2.6}$$

Rearranging terms

$$\frac{d}{dt} E_{01}^{+}(t) = \frac{\mathcal{T}}{\tau} E_{0P} - \frac{1}{\tau}\left(1 - r_1 r_2 e^{2ikL}\right) E_{01}^{+}(t), \tag{2.7}$$

where E_{0P} is a constant under the assumption that the external beam power is kept fixed. Equation (2.7) is a ordinary differential equation that can be solve with an integrating factor. We assume that the FP is tuned to resonance so that $2kL = 2m\pi$ and $\exp[i2kL] = \exp[2im\pi] = 1$ for $m = 0, 1, 2 \ldots$. Let

$$\Gamma \equiv \frac{2}{\tau}(1 - r_1 r_2), \quad \text{and} \tag{2.8}$$

$$\beta \equiv \frac{\mathcal{T}}{\tau}, \tag{2.9}$$

equation (2.7) becomes

$$\frac{d}{dt} E_{01}^{+}(t) = \beta E_{0P} - \frac{\Gamma}{2} E_{01}^{+}(t). \tag{2.10}$$

Defining

$$\mu(t) = e^{\int \frac{\Gamma}{2} dt} = e^{\frac{\Gamma}{2} t} \tag{2.11}$$

and multiplying equation (2.7) by $\mu(t)$ gives

$$\begin{aligned} \frac{d}{dt}(\mu(t) E_{01}^{+}(t)) &= \mu(t) \beta E_{0P} \Rightarrow \\ E_{01}^{+}(t) &= \frac{1}{\mu(t)} \left[\beta E_{0P} \left(\frac{2}{\Gamma} \mu(t) + A\right)\right], \end{aligned} \tag{2.12}$$

where A is an integration constant. Plugging in the explicit expression for $\mu(t)$ we have

$$E_{01}^{+}(t) = \beta E_{0P} \left(\frac{2}{\Gamma} + A e^{-\frac{\Gamma}{2} t}\right). \tag{2.13}$$

The constant A can be solved with the following initial condition $E_{01}^{+}(t=0)=0$, i.e. no field in the Fabry-Perot at $t=0$,

$$A = -\frac{\Gamma}{2}. \tag{2.14}$$

The full solution for the "charging" Fabry-Perot is summarized as

$$E_{01}^{+}(t) = \frac{\beta E_{0P}}{\Gamma}\left(1 - e^{-\frac{\Gamma}{2}t}\right), \quad \text{where} \tag{2.15}$$

$$\Gamma \equiv \frac{2}{\tau}(1 - r_1 r_2), \quad \tau = \frac{2L}{c}, \quad \text{and} \quad \beta \equiv \frac{\mathcal{T}}{\tau}. \tag{2.16}$$

Similarly the "discharging" of a Fabry-Perot follows by setting E_{0P} to zero in equation (2.7),

$$E_{01}^{+}(t) = E_{01}^{+} e^{-\frac{\Gamma}{2}t}, \tag{2.17}$$

where at $t=0$, $E_{01}^{+} \sim 2\beta E_{0P}/\Gamma$. A plot of the solutions for both cases is illustrated in figure 2.4a and figure 2.4b.

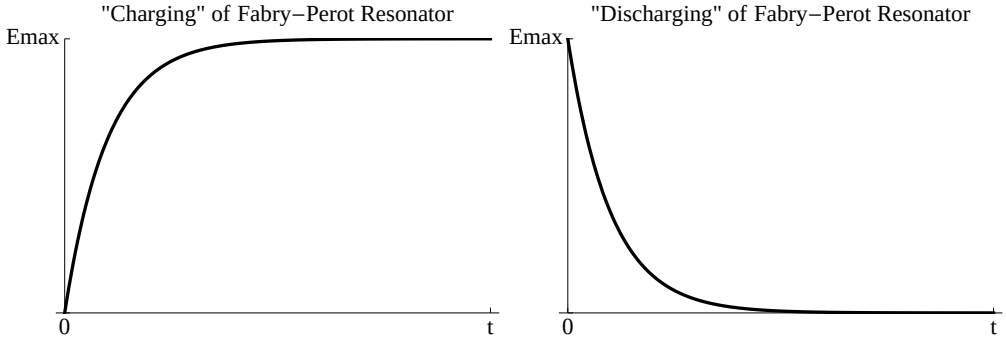

(a) Charging a Fabry-Perot resonator, plot of equation (2.15).

(b) Discharging a Fabry Perot resonator, plot of equation (2.17)

Figure 2.4: Transient solution to electric field amplitude in a Fabry-Perot cavity.

2.3 Double Fabry-Perot Resonator and High-Reflectance Layers

The transmission of the "Double" Fabry-Perot has been studied in [22, 23] and is illustrated in figure 2.5. The splitting between the double peaks depends on the values

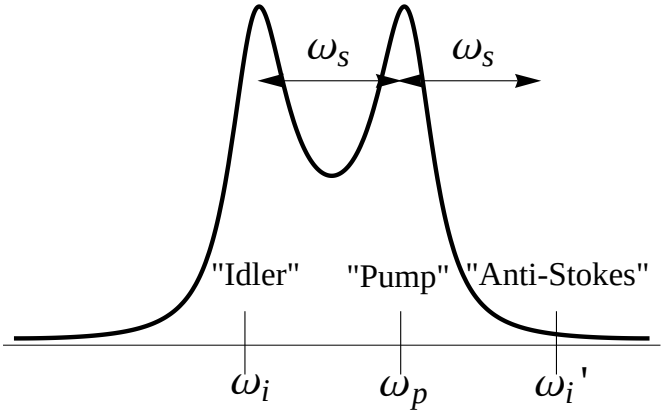

Figure 2.5: Triple mirror Fabry-Perot spectrum has two closely spaced resonances which should coincide with the pump and ilder modes for parametric oscillation of the membrane.

of the reflection coefficients. Consider the case with $r_1 = r_3 \equiv r$ and $r_2 < r$, where r corresponds to the amplitude reflection coefficient of the two end mirrors, and r_2 to the middle mirror labeled M2 in figure 2.3. The procedure for calculating the transmission and frequency splitting of a triple mirror Fabry-Perot interferometer as illustrated in figure 2.5 is outline as follows. The transmission through a triple mirror FP is given by [22]

$$T = \frac{(1-r^2)^2(1-r_2^2)}{\{(1-r^2)^2(1-r_2^2) + [r_2(1-r^2) + 2rx]^2\}}, \tag{2.18}$$

where $x = \cos(2\phi)$, ϕ is the phase related to length of the cavity by $\phi = 2\pi L/\lambda$, λ is the wavelength, L is the distance between the mirrors which are assumed to be equally spaced in order to satisfied the assumption that $\phi_1 = \phi_2$. The peak transmission occurs when $T = 1$ which leads to the following condition

$$\cos(2\phi) = -\frac{r_2(1+r^2)}{2r}. \tag{2.19}$$

The frequency spacing for some given reflection coefficients follows from

$$\Delta\omega = \omega_2 - \omega_1 = \frac{c}{L}\Delta\phi = \frac{c}{L}(\phi_1 - \phi_2), \tag{2.20}$$

where c is the speed of light. To find solutions to equation (2.19) the following observations are made

$$\phi_1 = \frac{1}{2}\cos^{-1}\left(-\frac{r_2(1+r^2)}{2r}\right); \quad \frac{\pi}{4} < \phi_1 < \frac{\pi}{2}, \tag{2.21}$$

and similarly for ϕ_2

$$\phi_2 = \frac{1}{2}\cos^{-1}\left(-\frac{r_2(1+r^2)}{2r}\right); \quad \frac{\pi}{2} < \phi_2 < \frac{3\pi}{4}. \tag{2.22}$$

In this fashion the frequency splitting can be calculated when the amplitude reflection coefficients are known. For convenience to conform to the domain of the arccosine the solution for ϕ_2 can be found from

$$\phi_2 = \pi - \phi_1; \quad \text{where} \quad \frac{\pi}{2} < \phi_2 < \frac{3\pi}{4}, \text{ if } \frac{\pi}{4} < \phi_1 < \frac{\pi}{2}, \tag{2.23}$$

and ϕ_1 is given by equation (2.21).

High reflectance (R) mirrors can be achieved by the use of high-reflectance stacks, commonly known as dielectric mirrors. Dielectric mirrors are made by stacking double layer films composed of high-and-low refractive indices n. For example, some of the films used are made from dielectric materials such as ZnS ($n = 2.35$), MgF_2 ($n = 1.38$), SiO_2 ($n = 1.46$), and mylar ($n = 1.6$). The mechanism behind high-reflectance dielectric mirrors is to have several stacks of high-low refractive indices films. The reflectance from such dielectric structures is given by [24]

$$R_{max} = \left[\frac{(n_0/n_s)(n_L/n_H)^{2N} - 1}{(n_0/n_s)(n_L/n_H)^{2N} + 1}\right], \tag{2.24}$$

where n_0 is the index of refraction outside the dielectric structure (typically air), n_L is the "low" index of refraction, n_H is the "high" index of refraction, and N is the number of high-low layers (stacks) used in the mirrror. We remind you that the reflectance is related to the reflection coefficient $R = |r|^2$.

2.4 Fabry-Perot with a Harmonically Moving End-Mirror in Quasi Steady State: The Parametric Oscillator.

An estimate of the threshold for parametric amplification of the membrane (pellicle) mirror parametric oscillator shown in figure 2.2 is presented. It is assumed that the microwave cavity on the left side of the parametric amplifier can be modeled as a mirror with a spring attached to a fixed wall as illustrated in figure 2.1 so that it forms a simple harmonic oscillator with resonant frequency ω_s, effective mass m, and quality factor Q_s. It is noted that this analysis holds in general where a high-Q high-frequency mechanical oscillator can be integrated into such a scheme, so long the system remains under the given limitations. The right half of the parametric oscillator is regarded as a "Double" optical Fabry-Perot resonator with two resonances at ω_i and ω_p. Furthermore, the "Double" Fabry-Perot allows for the selection of the two desired optical modes ω_i and ω_p. Since the "Double" Fabry-Perot acts as a single Fabry-Perot with two closely spaced resonances, the parametric amplifier is treated as a single Fabry-Perot cavity with a harmonically moving end mirror as illustrated in figure 2.1.

Consider a Fabry-Perot (FP) cavity of length L under quasi steady state conditions, and ignore transients during the build up of the modes as those discussed in [25]. Note that this problem has been solved by Braginsky et. al. [26], however, the solution presented here leads to the same results in a slightly more intuitive approach. The FP is pumped at the pump frequency ω_p, and due to the motion of the mirror two sidebands ω_i and ω_i' ("Stokes" and "anti-Stokes", respectively) are generated [27]. The "anti-Stokes" is suppressed via the "Double" Fabry-Perot scheme as shown in figures 2.3 and 2.5, and therefore negligible in the analysis.

The radiation force is given by

$$F(t) = \frac{1}{2}\epsilon_0 |E|^2 \mathcal{A} \tag{2.25}$$

where ϵ_0 is the permitivity of free space, $\mathcal{A}$ is the cross sectional area of the beam which has been assumed to be uniform over the mirror, and E is the total electric field in the Fabry-Perot. By modeling the moving end-mirror as a simple harmonic oscillator as depicted in figure 2.1, we have

$$\ddot{x} + 2\gamma_s \dot{x} + \omega_s^2 x = \frac{F(t)}{m}, \tag{2.26}$$

where x is the displacement of the simple harmonic oscillator from equilibrium, ω_s is the natural oscillator frequency, m is its mass, and $2\gamma_s$ is the FWHM. Using the slowly varying amplitude approximation in quasi steady state

$$x = X(t)e^{-i\omega_s t} + \text{c.c.} \tag{2.27}$$

the left side of (2.26) becomes

$$-2i\omega_s \left(\frac{dX}{dt} + \gamma_s X \right) e^{-i\omega_s t} + \text{c.c.} \tag{2.28}$$

where we assume that $2(\gamma_s - i\omega_s) \approx -2i\omega_s$. The right hand side can be expanded in terms of the fields

$$E_i = \mathcal{E}_{0i}(t)e^{-i\omega_i t} + \text{c.c.}, \quad E_p = \mathcal{E}_{0p}e^{-i\omega_p t} + \text{c.c.} \tag{2.29}$$

where the former is the "Stokes" or "idler" term and the latter is the "pump" mode, $\mathcal{E}_{0i}(t)$ being a slowly varying amplitude in quasi steady state, but $\mathcal{E}_{0p}$ being a constant in the "undepleted pump" approximation. Taking the beat terms and neglecting the nonresonant terms $|E_i|^2$ and $|E_p|^2$ gives

$$\begin{aligned} F(t) =& \epsilon_0 \mathcal{A}[\mathcal{E}_{0i}^* \mathcal{E}_{0p} e^{-i(\omega_p - \omega_i)t} \\ &+ \mathcal{E}_{0i}\mathcal{E}_{0p}e^{-i(\omega_p + \omega_i)t} + \text{c.c.}]. \end{aligned} \tag{2.30}$$

Equating both sides and multiplying by $e^{i\omega_s t}$ it follows

$$\begin{aligned} & -2i\omega_s \left(\frac{dX}{dt} + \gamma_s X \right) + \text{c.c.}(\propto e^{2i\omega_s t}) \\ = & \frac{\epsilon_0 \mathcal{A}}{m}[\mathcal{E}_{0i}^* \mathcal{E}_{0p} e^{-i(\omega_p - \omega_i - \omega_s)t} + \mathcal{E}_{0i}\mathcal{E}_{0p}e^{2i\omega_i t} \\ & + \text{c.c.}(\propto e^{i2\omega_s t}, e^{i2\omega_p t})], \end{aligned} \tag{2.31}$$

where $\omega_p - \omega_i \approx \omega_s$. Note that driven mechanical oscillator is a linear system and only the force at resonance will be the main driving force of the mechanical oscillator; hence, we can neglect off-resonance terms (in the rotating-wave approximation), and write the

driven oscillator equation as

$$\frac{dX}{dt} + \gamma_s X = \frac{i\epsilon_0 \mathcal{A}}{2\omega_s m} \mathcal{E}_{0i}^* \mathcal{E}_{0p} e^{-i(\omega_p - \omega_i - \omega_s)t}. \tag{2.32}$$

Following the convention used by Braginsky et. al. [26], let us define the fields as

$$E_i(t) = A_i (D_i(t)\, e^{-i\omega_i t} + \text{c.c.}) \tag{2.33}$$

$$E_p = A_p (D_p e^{-i\omega_p t} + \text{c.c.}), \tag{2.34}$$

where A_i, A_p are normalized so that the total energy stored in each mode is $U_{p,i} = 2\omega_{p,i}|D_{p,i}|^2$, and $D_i(t)$ is a slowly varying complex amplitude, but D_p is a constant, in the "undepleted pump" approximation. With this normalization the energies in each mode are

$$U_{p,i} = \frac{\mathcal{V}}{2}\epsilon_0 \left\langle E^2 \right\rangle = A_{p,i}^2 \epsilon_0 |D_{p,i}|^2 \mathcal{A}L = 2\omega_{p,i}^2 |D_{p,i}|^2, \tag{2.35}$$

where $\mathcal{V} = \mathcal{A}L$ is the volume of the cavity, and solving for $A_{p,i}$ gives

$$A_{p,i} = \omega_{p,i}\sqrt{\frac{2}{\epsilon_0 \mathcal{V}}}. \tag{2.36}$$

Inserting the normalization

$$\mathcal{E}_{0i}^* = A_i D_i^* \text{ and } \mathcal{E}_{0p} = A_p D_p \tag{2.37}$$

into equation (2.32) we arrive at the coupled differential equation

$$\frac{dX}{dt} + \gamma_s X = \frac{i\omega_p \omega_i}{m\omega_s L} D_p D_i^* e^{-i\Delta\omega t} \tag{2.38}$$

,where $\Delta\omega \equiv \omega_p - \omega_i - \omega_s$. To arrive at the equation for the "Stokes" or "idler" field in the cavity note that the "Stokes" mode is generated from the main "pump" mode so that the "Stokes" field is proportional to the oscillator amplitude. The electric field reflected from a moving mirror is given by [27]

$$E_p = \mathcal{E}_{0p} e^{-i\omega_p t} e^{2ik_p x} + \text{c.c.} \tag{2.39}$$

For small x, we find

$$E_p = \mathcal{E}_{0p} e^{-i\omega_p t}(1 + 2ik_p x) + \text{c.c.}. \tag{2.40}$$

where the last term leads to the Doppler-generated electric field

$$E_{\text{Doppler}} \equiv 2ik_p x\mathcal{E}_{0p}e^{-i\omega_p t} + \text{c.c.}. \tag{2.41}$$

In quasi steady state conditions, the "pump" optical mode is the main source of the "Stokes" optical mode. Using the FP recursion relation for the cavity's electric field [28, 25]

$$E_i(t+\tau) = E_{\text{Doppler}}(t+\tau) + RP_f E_i(t), \tag{2.42}$$

where $\tau = 2L/c$ is the round trip time, R is the power reflectivity (i.e., the absolute square of the reflection coefficient) of the end mirrors, P_f is the propagation factor [28, 25] which accounts for the phase accumulated by the beam one round trip earlier, E_{Doppler} is the Doppler electric field generated from the "pump" mode, along with in the slowly varying displacements and fields,

$$x = X(t)\,e^{-i\omega_s t} + \text{c.c.} \tag{2.43}$$

$$E_i = \mathcal{E}_{0i}(t)\,e^{-i\omega_i t} + \text{c.c.} \tag{2.44}$$

$$E_p = \mathcal{E}_{0p}e^{-i\omega_p t} + \text{c.c.}, \tag{2.45}$$

and finally taking the resonant terms, we arrive at

$$\frac{d\mathcal{E}_{0i}}{dt} + \gamma_i\mathcal{E}_{0i} = \frac{i}{\tau}X^*\mathcal{E}_{0p}e^{-i\Delta\omega t}, \tag{2.46}$$

where $\Delta\omega \equiv \omega_p - \omega_i - \omega_s$. Inserting the defined normalization

$$\frac{dD_i}{dt} + \gamma_i D_i = \frac{i}{L}\frac{\omega_p^2}{\omega_i}X^*D_p e^{-i\Delta\omega t}, \tag{2.47}$$

where $\tau = 2L/c$, and $k_p c = \omega_p isused.$ With the approximation that

$$\frac{\omega_p^2}{\omega_i} = \frac{\omega_p^2}{\omega_p - \omega_s} \approx \frac{\omega_p^2}{\omega_p} = \omega_p \tag{2.48}$$

(i.e. $\omega_p \gg \omega_s$) the coupled differential equation for the idler field becomes,

$$\frac{dD_i}{dt} + \gamma_i D_i = \frac{iX^*D_p\omega_p}{L}e^{-i\Delta\omega t}. \tag{2.49}$$

This result is consistent with Braginsky's [26] equation (1). Equations (2.38) and (2.49)

form a system of linear differential equations which can be solved simultaneously. For the detailed solutions to the coupled differential equations (2.38) and (2.49) and the condition for parametric amplification the reader is referred to [26]. The threshold condition is

$$\frac{2U_pQ_iQ_s}{mL^2\omega_s^2} > 1 \tag{2.50}$$

where U_p is the energy stored in the "pump" mode, L is the length of the Fabry-Perot, m is the effective mass, Q_i is the Q of the idler mode, and Q_s is the effective Q of the mechanical oscillator.

2.5 Remark on Effective high-Q Mechanical Oscillator: SHO model for the Microwave Cavity-Pellicle Mirror System

In the previous section we made a crucial assumption that the microwave cavity coupled to a charged membrane will effectively behave like a high-Q high-frequency mechanical oscillator. This indeed is a vital assumption, and although there are hurtles to overcome in suscessfully implementing such a high-Q high-frequency mechanical oscillator, the analysis holds independently. Some support is presented for as why a high-Q superconducting microwave cavity coupled to a mechanical oscillator may be modeled as a simple harmonic oscillator (SHO) whose quality factor Q_{loaded} is approximately given by the quality factor of the SC cavity Q_s. First, let us treat the mechanical membrane as a one dimensional simple harmonic oscillator (SHO). This is a valid assumption because the mechanical membrane's equation of motion is of the same form as a one-dimensional SHO along the direction of vibration, the only difference stems from mode shape functions which account for the transverse directions, in the plane of the membrane. Hence, the only insight gained in the two dimensional analysis of the membrane are the mode profiles (shapes).

Let the pellicle end-mirror (membrane) consist of a thin SC film deposited on a thin, light, flexible diaphragm, which is sufficiently thin so that it can easily be driven into mechanical motion. Furthermore, suppose that the SC film is electrostatically charged with a net DC charge q. Assume that the charge q which resides on the surface of the film is so tightly bound (via the Coulomb force) to the metallic film that when the

charge q moves, the film will co-move with it [1]. Then the longitudinal electric field $\mathbf{E}_z$ at the surface of the SC film will lead to the instantaneous force

$$\mathbf{F}_z\left(t\right) = q\mathbf{E}_z(t) + \mathbf{F}_{\text{rad}}\left(t\right), \tag{2.51}$$

where $\mathbf{E}_z$ is a longitudinal electric field at the surface of the SC film, and where the force on the film due to radiation pressure is given by

$$\mathbf{F}_{\text{rad}}\left(t\right) = \frac{1}{2}\varepsilon_0 \mathbf{E}_z(t)^2 \mathcal{A} \propto \mathbf{E}_z(t)^2, \tag{2.52}$$

where ϵ_0 is the permittivity of free space, and $\mathcal{A}$ is the area of the film over which $\mathbf{E}_z(t)$ is nonvanishing. Since the radiation force $\mathbf{F}_{\text{rad}}\left(t\right)$ scales quadratically with the electric field at the surface of the film, while the Coulomb force $q\mathbf{E}_z(t)$ scales linearly, there exists a maximum electric field strength $E_{\max}$ such that if $|E_z\left(t\right)| < E_{\max}$, then the Coulomb force $q\mathbf{E}_z(t)$ dominates over the radiation force $\mathbf{F}_{\text{rad}}\left(t\right)$. Comparing (2.51) and (2.52), one finds that

$$E_{\max} = \frac{2q}{\epsilon_0 \mathcal{A}}.$$

For the rest of this analysis assume that we are in the regime where the electric field in the cavity is sufficiently less than $E_{\max}$, so that the radiation force is negligible, and (2.51) becomes

$$\mathbf{F}_z\left(t\right) \approx q\mathbf{E}_z(t). \tag{2.53}$$

With the approximation that at high (i.e., microwave) frequencies the pellicle end-mirror behaves like a free mass, the equation of motion for the pellicle mirror becomes

$$m\frac{d^2x}{dt^2} = qE(t), \tag{2.54}$$

where we drop the subscript z from $\mathbf{E}_z(t)$ for convenience, and we switch from z to the variable x to denote the displacement of the oscillating mass m from equilibrium. The time-dependent part of the longitudinal electric field at the surface of the SC film can

[1] This is justified because the binding energy of the net charge of electrons to the surface of the metal is on the order of tens of eV, whereas the simple harmonic motion of the mirror corresponds to an energy on the order of meV.

be described as a harmonically time-varying field given by

$$E(t) = \mathcal{E}(t)e^{-i\omega t} + \text{c.c.},$$

where $\mathcal{E}(t)$ is a slow varying amplitude. It follows that the displacement of the charged mirror is given by

$$x(t) = -\frac{q}{m\omega^2}E(t). \tag{2.55}$$

Observe that the displacement $x(t)$ is *linear* with the longitudinal electric field $E(t)$ evaluated at the surface of the flat mirror in the SC resonator. It is also required that the displacement of the mirror be small enough as to not significantly perturb the Q of the SC cavity. Now suppose that the SC resonator is in steady state and filled with some constant input power from some external microwaves so that the pellicle end-mirror displacement is given by (2.55). If the injected microwave power is shut off, the SC resonator's electric field will decay exponentially with time. Hence, the displacement of the pellicle end-mirror will also decay exponentially with time. It now suffices to show that the electric field $E(t)$ in the resonator can be described by a simple harmonic oscillator. The equation of motion for the undriven simple harmonic oscillator is

$$\frac{d^2x}{dt^2} + 2\gamma\frac{dx}{dt} + \omega^2 x = 0, \tag{2.56}$$

where γ is the decay parameter of the oscillator. Using (2.55) the equivalent simple harmonic motion equation for the field in the cavity becomes

$$\frac{d^2E}{dt^2} + 2\gamma\frac{dE}{dt} + \omega^2 E = 0, \tag{2.57}$$

where E is the electric field evaluated at the surface of the moving mirror, 2γ is interpreted as the FWHM of the SC cavity resonance, and ω is the resonance frequency of the SC resonator. (Note that (2.57) also follows from the Helmholtz analysis for a lossy resonator.) In the slowly varying amplitude approximation, (2.57) reduces to a first order linear differential equation for the slowly varying amplitude

$$\frac{d\mathcal{E}}{dt} + \gamma\mathcal{E} = 0 \tag{2.58}$$

and the solution is

$$\mathcal{E}(t) = E_0 e^{-\gamma t} = E_0 e^{-\omega t/2Q_s}, \tag{2.59}$$

where E_0 is the initial electric field amplitude at the surface of the mirror, and $Q_s = \omega/2\gamma$ is the SC resonator's intrinsic quality factor. Therefore, the field in the SC microwave resonator decays like a simple harmonic oscillator with a time constant that is proportional to the quality factor of the cavity. Furthermore, since the displacement of the pellicle end-mirror is linear with the field inside the resonator, it must also decay like a simple harmonic oscillator. Note that with (2.59) the field inside the resonator is

$$E(t) = E_0 e^{-\omega t/2Q_s} e^{-i\omega t} + \text{c.c.} \tag{2.60}$$

which is the well-known exponentially decaying solution with the ringdown time

$$\tau_r = 2Q_s/\omega$$

of the resonator.

Finally, lets consider the effect that driving the pellicle end-mirror with external radiation has on the quality factor Q_s of the SC resonator. The loaded quality factor Q_{loaded}, where the loading refers to the power loss due to the simple harmonic motion of the charged mirror, is given by

$$Q_{\text{loaded}} = \frac{\omega U_0}{\mathcal{P}_{\text{loss}}}, \tag{2.61}$$

where U_0 is the energy stored in the cavity, and $\mathcal{P}_{\text{loss}}$ is the total power loss in the cavity given by

$$\mathcal{P}_{\text{loss}} = \mathcal{P}_c + \mathcal{P}_{\text{mirror}}, \tag{2.62}$$

where $\mathcal{P}_c$ is the intrinsic power loss of the SC resonator and is related to the resonator's intrinsic quality factor by $Q_s = \omega U_0/\mathcal{P}_c$, and where $\mathcal{P}_{\text{mirror}}$ is the average power loss due to the motion of the charged pellicle end-mirror. From (2.61) one finds that

$$Q_{\text{loaded}} = \frac{Q_s Q_{\text{SHM}}}{Q_s + Q_{\text{SHM}}}, \tag{2.63}$$

where $Q_{\text{SHM}} \equiv \omega U_0/P_{\text{mirror}}$ is the contribution to the quality factor arising from simple harmonic motion. Although it is possible that some or all of the power loss that goes

into the simple harmonic motion of the charged mirror is converted into electromagnetic radiation power which goes back into the SC resonator, it is instructive to account for it. The average power loss due to the moving pellicle end-mirror is

$$\mathcal{P}_{\text{mirror}} = \langle \mathbf{F} \cdot \mathbf{v} \rangle = \frac{q^2 E_0^2}{2m\omega}. \tag{2.64}$$

The electric field is calculated by assuming some externally applied microwave power $\mathcal{P}_{\text{ext}}$ is injected into the SC resonator. In steady state, the energy in the cavity U_0 is [29]

$$U_0 = \frac{4\beta \mathcal{P}_{\text{ext}}}{(1+\beta)^2} \frac{Q_s}{\omega}, \tag{2.65}$$

where β is a input/output coupling parameter and is assumed to be unity, $\beta \equiv 1$. It follows that the amplitude of the electric field inside the cavity E_0 is given by

$$E_0^2 = \frac{8\mathcal{P}_{\text{ext}} Q_s}{m\omega \mathcal{V} \epsilon_0}, \tag{2.66}$$

where $\mathcal{V}$ is the effective volume of the SC resonator. Hence, the average power loss from the pellicle end-mirror is

$$\mathcal{P}_{\text{mirror}} = \frac{4q^2 \mathcal{P}_{\text{ext}} Q_s}{m\omega^2 \mathcal{V} \epsilon_0}. \tag{2.67}$$

Assuming an external applied microwave power of $\mathcal{P}_{\text{ext}} = 500$ pW, $q = 20$ pC, $Q_s = 10^{10}$, $m = 2$ mg, $\omega = 2\pi \times 12$ GHz, and an effective volume of $\mathcal{V} = 1.25$ cm^3, one finds

$$\mathcal{P}_{\text{mirror}} \approx 6 \times 10^{-20} \text{ W} \tag{2.68}$$

This power yields

$$Q_{\text{SHM}} \approx 4 \times 10^{21}. \tag{2.69}$$

Since $Q_s \ll Q_{\text{SHM}}$, it follows from (2.63) that to an extremely good approximation

$$Q_{\text{loaded}} \approx Q_s.$$

Hence, the cavity's quality factor will not be severely affected by driving a mechanical membrane into motion, and because the membrane is tightly coupled to the electric field in the cavity it will oscillate with the same ringdown time as the fields. Finally,

this analysis is speculative and some other assumptions made include the effective mass of the oscillator being approximately given by the actual mass. In addition, one very important issue not discussed here is the damping associated with modulating the length of the microwave cavity, thus, is has been assumed that the motion of the membrane is small enough as to not perturb the cavity's Q factor. More on this effect is discussed in chapter 7, by re-examining some of Brangiskys earlier work on the ponderomotive effects [30, 31].

3

Superconductivity

We develop an important understanding of type I and type II superconductivity. Using the classical Drude model of conductivity, and the Ginzburg-Landau theory it is possible to discover some of the fundamental properties of superconductors. In particular we begin by introducing the nature of coherence length, penetration depth, and finally give a short motivation for cooper pairing. Finally we discuss experimental and measurement techniques.

3.1 Superconductivity

The concept of current flow with zero resistance came to light during the early 1900's. James Dewar in 1904 believed that resistance could approach zero value with decreasing temperature [32]. If we consider the nature of resistance due to collisions of the conduction electrons with impurities, phonons, and electrons, current flow with zero resistance can be conceived by the electron collision model (Drude model). In 1911 Kammerling Onnes and his research group tested the Drude model at low temperatures. Using Mercury due to its high purity, they found that the resistivity suddenly jumped from a finite value to zero when they reached temperatures near 4K [1], a phenomena which was not expected from the Drude model. This discovery brough forward a new phase of matter whose physical consequence was to produce current flow with no

[1] The temperature at which a normal metal becomes superconducting is known as the critical temperature T_c

resistance, superconductors [2]. A superconductor is not just a material that can have zero resistivity, we will see that indeed a superconductor is a new phase of matter and with it come many interesting properties.

Superconductors can have many applications, but primarily they are of extreme interest simply because they give the possibility of transmitting current with no ohmic loss[3]. Our interests in superconductors is focused on producing extremely high quality superconducting radio frequency cavities (SRF) and SC membranes. In addition, its been speculated that superconductors might entail a lot more than dissipationless current transmission. Due to their macroscopic quantum nature, superconductors might be a possible avenue for understanding gravity in quantum mechanics [33].

3.1.1 Drude Model

In the Drude model the current density is derived from the assumption that resistivity arises due to collision of electrons. To arrive at an expression for the current density consider the flow of electrons through a cross sectional area A with velocity v, and average lifetime τ for free motion of electrons between collisions, it follows that

$$j = \frac{ne^2\tau}{m}E \tag{3.1}$$

where n is the number density of conduction electrons, m is the mass of an electron, and E is a DC electric field. The resistivity ρ and conductivity are defined σ as

$$\rho = \frac{m}{ne^2}\frac{1}{\tau} \quad , \ \sigma \equiv \frac{1}{\rho}. \tag{3.2}$$

With the above definitions the current can be expressed in a more common form known as Ohms law

$$j = \sigma E. \tag{3.3}$$

[2]Sudden jumps usually are associated with a phase transition of matter, which was not predicted by the Drude model. The Drude model only accepted zero resistivity as a 'smooth' function of temperature.

[3]The interest is really in high temperature superconductors, as they would have a significant impact on our technological advances and energy consumption

If the resistivity should have any temperature dependence it should lie in the average lifetime between collisions (everything else is constant). We can interpret τ as a scattering rate which is compose of the sum of all scattering events;

$$\frac{1}{\tau} = \frac{1}{\tau_{im}} + \frac{1}{\tau_{el-el}} + \frac{1}{\tau_{el-ph}} \tag{3.4}$$

each which may independently depend on temperature. The subscripts above represent; impurites, electron-electron, and electron-phonon interactions, respectively. For a normal metal at low temperature the Drude model is adequate and fits a smooth function;

$$\rho \sim \rho_0 + \rho(T). \tag{3.5}$$

The first observation using the Drude model is that inside a superconductor the electric field must be zero so that the current density j remains finite, i.e., from Ohms law

$$j = \frac{1}{\rho}E = \frac{1}{0}E \Rightarrow E = 0. \tag{3.6}$$

This also implies that if a superconductor is to have zero resistivity then it must have an infinite conductivity since $\sigma = 1/\rho = \infty$. There has been substantial proof that indeed a superconductor has zero resistivity, among the most convincing is the fact that persistent currents have been observed.

Another interesting property of superconductors can be partially explained by the Drude model. Consider a superconducting metal block in the normal metal stage which is cooled below its critical temperature so that it becomes superconducting. If we now add a small magnetic field we will find that the field is completely expelled from the interior of the superconductor. This effect can be explained with classical electrodynamics by an application of Faraday's law and it is not a unique characteristic of superconductors as it can apply to perfect conductors as well. Thus, because the electric field must be zero inside the superconductor, a change in magnetic flux is not allowed by Faraday's law

$$-\frac{d\Phi}{dt} = \oint \vec{E} \cdot d\vec{r} = 0. \tag{3.7}$$

. Nevertheless, there is a more subtle effect occurring here which is unique to superconductors. To illustrate, suppose a constant magnetic field is applied to our superconducting metal block at all times during the cooldown from the normal state to the superconducting state. In this case classical electrodynamics predicts no expulsion of the magnetic field, however as it turns out, the magnetic field is also expelled in this situation. This effect cannot be explained with classical physics and it is known as the *Meissner-Ochsenfeld Effect*. The Meissner effect is a unique phenomena that provides the definition of a superconductor. In principle a normal metal with zero resistivity would not exhibit a Meissner effect, whereas a superconductor expels small magnetic fields applied to it and can be thought as a perfect diamagnet.

3.1.2 London Equation, Penetration depth

The London brothers were some of the first pioneers in developing a theory for superconductivity. Their approach was simple and analogous to superfluids. The main idea is the assumption that a fraction of the electrons in the superconductor undergo a superfluid transition while the other fraction remain in a normal state. In the *two-fluid model* the superfluid electrons can move without dissipation, while the normal electrons continue to act with finite resistance. For such a system the number density is a sum of both normal and superconducting electron densities

$$n = n_n + n_s. \tag{3.8}$$

Extending the DC Drude model to include time dependent fields (AC Drude model) yields a *complex* frequency dependant conductivity

$$\sigma(\omega) = \frac{ne^2\tau}{m}\frac{1}{1 - iw\tau} \tag{3.9}$$

with the *real* part given by

$$Re[\sigma(\omega)] = \frac{ne^2}{m}\frac{\tau}{1 + w^2\tau^2}. \tag{3.10}$$

In a perfect conductor the mean collision time approaches infinity which is equivalent to the limit as $1/\tau \to 0$ in equation 3.10

$$\lim_{1/\tau \to 0} \sigma(\omega) = -\frac{ne^2}{im\omega}. \tag{3.11}$$

The *real* part of the conductivity corresponds to currents in phase with the applied electric field (known as the resistive element), while the *imaginary* part corresponds to out of phase currents (known as the inductive element). In the limit where the resistivity approaches zero the conductivity is a purely imaginary quantity, thus, there is no energy dissipation in a perfect conductor. To arrive at the London brother's results observe that the *real* part of the conductivity must vanish in a SC while the integral of it must remain constant,

$$\int Re[\sigma(\omega)]d\omega = \frac{\pi ne^2}{m} = \text{constant}. \tag{3.12}$$

Hence, its is convenient to introduce the Dirac Delta Function, and the London brothers speculated

$$\sigma(\omega) = \frac{\pi n_s e^2}{m}\delta(\omega) - \frac{n_s e^2}{i\omega m} \tag{3.13}$$

This model correctly interprets the delta function, however it fails to explain the fact that the resistivity becomes finite after some energy value, in other words the energy gap observed in superconductors.

Using the AC Drude model the London equation follows from[4]

$$(\nabla \times j)e^{-i\omega t} = \sigma(\omega)(\nabla \times E)e^{-i\omega t} = \sigma(\omega) - \frac{d}{dt}Be^{-iwt}. \tag{3.14}$$

Simplifying and in the limit of zero resistivity gives

$$\nabla \times j = -\frac{n_s e^2}{m}B, \tag{3.15}$$

or more compactly

$$j = -\frac{n_s e^2}{m}A, \tag{3.16}$$

[4]We will drop the vector signs as it should be apparent which quantities represent vectors

where A is the magnetic vector potential. This equation was a significant accomplishment by the London brothers and it correctly predicts the London Penetration Depth

$$\lambda \equiv (\frac{m}{\mu_0 n_s e^2})^{1/2}. \tag{3.17}$$

The London penetration length is the distance inside the surface of a SC over which an external magnetic field is screened out to zero. As a simple illustration of the London Penetration Depth consider a superconducting slab placed in the y-z plane with an external magnetic field along the positive z direction. From the solution to equation (3.15) the magnetic field inside the superconductor is

$$B = B_0 e^{-\frac{x}{\lambda}}. \tag{3.18}$$

from which it is apparent that the applied magnetic field decays exponentially, thus, penetrating the superconductor a very small distance beyond the surface.

3.1.3 Ginzburg-Landau Model (GL), Coherence Length

The GL model was the next step to advance the understanding of superconductivity. It was obvious after some time that a superconductor was indeed a new phase of matter due to its peculiar transition at the critical temperature. The GL theory is postulated on the basis of defining an order parameter ψ which is zero above the critical temperature and non-zero below the critical temperature. In addition, GL assumed that the free energy must depend "smoothly" on the order parameter ψ. Because the order parameter can be a *complex* quantity, it follows that the energy must depend strictly on $|\psi|$

$$-\frac{\hbar^2}{2m}\nabla^2\psi(r) + (a + b|\psi(r)|^2)\psi(r) = 0, \tag{3.19}$$

where a and b are functions of temperature and must satisfy $|\psi|^2 = -a(T)/b(T)$. To obtain the physical significance of the order parameter consider the solution to equation (3.19) for the simple case of a supercoducting slab placed in the y-z plane. The solution is

$$\psi_0 \tanh\left(\frac{x}{\sqrt{2}\xi(T)}\right); \qquad \xi(T) = \left(\frac{\hbar^2}{2m|a(T)|}\right)^{1/2}, \tag{3.20}$$

where ξ is the GL coherence length and $\psi_0 = \sqrt{|a|/b}$. The GL coherence length should not be confused with the BCS coherence length ξ_0 which relates to the physical size of a single Cooper pair. Here the GL coherence length (ξ) represents a measure of the distance from the surface over which the order parameter (ψ) has recovered back to its bulk value. Note that in taking the quantum prescription to equation (3.19) and adding the magnetic vector potential we can recover the London equation, which hints at the connection of the order parameter with a macroscopic wave function whose norm is equal to the density of Cooper pairs. Hence, the Ginzburg-Landau theory describes the macroscopic behavior of the electron superfluid. A superconductor is a macroscopic quantum coherent object, and it follows that the order parameter ψ can be directly associated with the flow of superelectrons [34]

$$-\nabla \cdot J = \frac{\partial |\psi|^2}{\partial t}, \tag{3.21}$$

and

$$J = \frac{1}{m}\mathrm{Re}(\psi^*(\frac{\hbar}{i}\nabla - qA)\psi). \tag{3.22}$$

3.1.4 The Cooper Pair

Finding the correct theory for superconductivity was not a trivial task due to the electron high energies near the Fermi energy, and thus high electron velocities. It was not until the 1950's that Cooper postulated that superconductivity was a consequence of electron-electron bound states near the Fermi energy. That is, Cooper believed that two electrons in the Fermi surface could form a bound state. Although this may seem counterintuitive given that (1) electrons have a Coulomb repulsion and (2) they have high kinetic energies at the Fermi surface, Cooper showed that indeed it is possible for two electrons to form a bound state. In 1957 Bardeen Cooper and Schieffer published two remarkable papers for the Theory of Superconductivity [35, 36]. This work took the idea of a Cooper pair into a full developed theory and in detailed explained the nature of Cooper pairs. In short, Cooper pairs are possible due to the electron-phonon interaction that exist in a solid. And, indeed a superconductor is a new state of matter whose properties are described by a macroscopic wave function (BCS wave function).

A superconductor is in essence a condensate, but unlike our usual Bose Einstein condensate, or the traditional Fermi condesate, a superconductor is a dynamic condensate of electron-electron pairs all with energy slightly greater than the Fermi energy.

It can be shown that two electrons at the Fermi surface will form a bound state because of the simple fact that the formation of Cooper pairs lowers the system's energy. For a simple two electron system the phonon interaction in the weak coupling limit ($V_0 D(E_F) \ll 1$) leads to a decrease in energy given by [34]

$$E \approx -2\hbar\omega_D \exp\left(-\frac{2}{V_0 D(E_F)}\right), \tag{3.23}$$

where $\hbar\omega_D$ is a typical phonon energy, V_0 is an interaction potential, and $D(E_F)$ is the density of states at the Fermi surface. This result shows that the pair state will always have a lower energy than the normal ground state no matter how small the interaction V_0. This indeed is a surprising result as it shows that the formation of Cooper pairs is favorable. Although Cooper pair formation lowers the energy of the ground state their interaction is a lot more complicated as described by the BCS theory of superconductivity. Nevertheless, the superconducting state is a highly correlated many-electron state.

3.2 Type I Conventional Superconductivity

Type I superconductors mainly consist of natural elements such as aluminum, lead, and tin, however, alloys, intermetallic compounds and ionic compounds also may exhibit superconductivity. In the *boson condensation* representation the Cooper pair binding energy E_g is shared by 2 electrons so that the gap energy $\Delta = \frac{1}{2}E_g$ is the binding energy per electron. This means that in order to break a Cooper pair we must add at least $E = 2\Delta$ amount of energy. that will then excite a Cooper pair into two quasi-particles, see figure 3.1. In general the total density of conduction electrons is given by

$$n = n_n(T) + n_s(T), \tag{3.24}$$

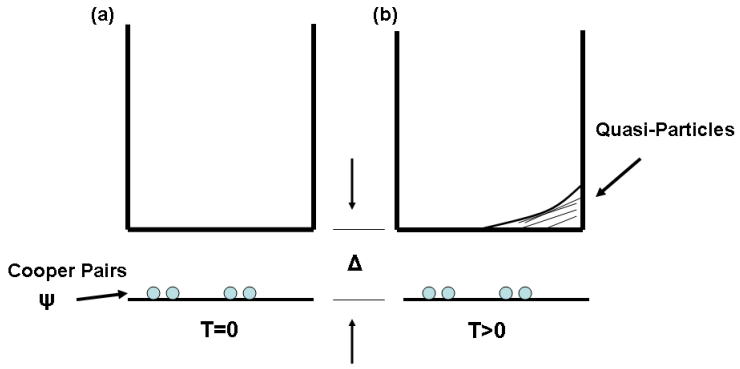

Figure 3.1: Electron occupancy at different temperatures as given by the Fermi-Dirac distribution. Shaded region indicates electron occupancy. At T=0 all electrons exist as Cooper pairs and occupy the same ground state (a). At T > 0 some Cooper pairs are broken and excited to the quasi-particle state (b)

where at T=0 we have $n_n(0) = 0$ and $n_s(0) = n$. It can be shown that [34]

$$n_s \approx n\left[1 - \left(\frac{T}{T_c}\right)^4\right], \tag{3.25}$$

and

$$E_g \approx 3.52 k_B T_c \left[1 - \frac{T}{T_c}\right]^{1/2}. \tag{3.26}$$

All Cooper pairs are in a coherent zero-momentum ground state [5]. However, excitation of Cooper pairs into the quasi particle state can occur. This is how the first experiments confirmed the existence of a band gap [37].

[5] We are assuming conventional superconductors in which their ground state is a zero momentum eigenstate, L=S=0.

3.3 Type II superconductivity

Type II superconductivity was discovered around the 1930's when niobium (Nb) was determined to be a superconductor. Niobium seems to be the only pure element superconductor that exhibits type II superconductivity. Most type II superconductors exhibit higher transition temperatures than type I. By the 1950's scientist had realized the technological advances that a room temperature superconductor could yield and the race to find this superconductor had well been on its way, and its still ongoing today. Its interesting to note that most of the beginning history of high temperature superconductivity (HTS) has been forgotten about due to the fact that thousands of different complicated compounds have been discovered since. For example, Bernd T. Matthias alone is said to have made some 3000 different alloys in his heroic attempt to achieve hight-Tc superconductivity during the 1950's and 1960's [38]. Surely keeping track of all made compounds would be a great task. Nevertheless, certain types of compounds stood-out among the myriad, and these compounds today form their own classes of high Tc superconductors. Unfortunately, the theory has not been able to keep up with the fast pace of the experimentalist, and type II or more specifically high Tc superconductivity is not well understood.

Type II superconductivity exhibits a peculiar phenomena called the mixed state. The mixed state exist when an applied magnetic field exceeds a value referred to as the lower critical field, B_{c1} but does not exceed the upper critical field, B_{c2} (i.e. $B_{c1} < B_{app} < B_{c2}$). In the mixed state a type II superconductor traps flux by forming cylindrically symmetric domains called vortices. Each vortex has a fundamental unit of trapped flux given by $\Phi_0 = h/2e$, and the density of vortices is proportional to the applied magnetic field. Hence, it is possible to adjust the number of vortices by simply adjusting the applied magnetic field. Near the upper critical field B_{c2} the vortices form a triangular lattice known as a Abrikosov vortex lattice, their spacing is given by $d = 2\xi(\pi/\sqrt{3})^{1/3} \approx 2.69\xi$ [34]. The order parameter (κ) of type II superconductors is defined by $\kappa = \lambda/\xi > 1/\sqrt{2}$, and all type II superconductors must obey this inequality. Superconductors with $\kappa < 1$ are type I SCs. At sufficient low temperatures the vortices are characterized by a normal core of radius ξ within a shielding current of radius λ.

3.3.1 Classes of Type II

Its important to emphasize the fact that type II superconductivity is, in a phenomenological sense, understood as explained by the London and Ginzburg Landau theories. It was A.A. Abrikosov along with V. Ginzburg and A.J. Leggett who receive the nobel prize in 2003 for there explanation of the phenomena observed in type II superconductors. Namely, the creation of vortices and the Abrikosov vortex lattice in type II SCs. Many classes of type II SC exist. Among the first are the so called A15 compounds. This group consist of binary alloys such as NbN, BnC, V_3Si, Nb_3Sn, NbTi, and Nb_3Ge. Out of this group two compounds have allowed for successful production of superconducting magnets, Nb_3Sn and NbTi with $T_c = 18K$, and $T_c = 9K$ respectively. Organic superconductors were also discovered. The first polymer superconducting material was found in $(Sn)_x$ in 1975. Since then, a long list of organic superconductors has been synthesized.

3.4 SC Measurement Techniques

Cold temperature measurement are an integral part of our work. In particular we are interested in SC transition temperature measurements, critical current measurements, and resistance measurements. At the Chiao lab we implement a four lead measurement technique (see 3.4.1 below) for determination of the desired quantities. In addition, we have also used a simple flux trapping technique when the sole purpose is determination of a superconducting transition. There are a few important factors that must be taken into consideration when making low level voltage measurements. For example, thermoelectric voltages which arise when temperature gradients exist between joints of two different metals should be minimized by taking the proper precautions during wiring the experimental set up [39]. Typically this occurs at solder points and care must be taken to reduce this effect.

3.4.1 4-lead measurement

In a four lead measurement configuration two wire leads are used to drive a current through the sample and two additional voltage sensing leads are used to measure the voltage drop across the sample. Typically voltmeters have a very high input impedance

(>10 MΩ) so that they draw very little current. The voltage across a sample with resistance R_s in a four lead measurement configuration is given by

$$\Delta V_m = R_s(I - I_s) - 2R_L I_s, \tag{3.27}$$

where I_s is the sample current drawn by the voltmeter, R_L is the resistance of the wire leads, and I is the total current output from the power supply. In the limit where $I >> I_s$ we find

$$\Delta V_m \approx I R_s \tag{3.28}$$

which is the voltage drop strictly through the sample under test. In this fashion the wire leads do not contribute to the resistance under test and a true value for the resistance of the sample can be extracted.

For our purposes we use a Keithley 2400 source meter which can measure resistances up to a few tens of micro-Ohms. Typically, for superconductors one must be capable of measuring resistances down to a few nano-ohms. However, we can use the source readback and offset compensation features on the Keithley 2400 source meter to determine when a particular superconducting sample has undergone a SC transition. For very good samples this transition is very fast and a good estimate for the transition temperature can be made as displayed in figure 3.2. As an example of this method

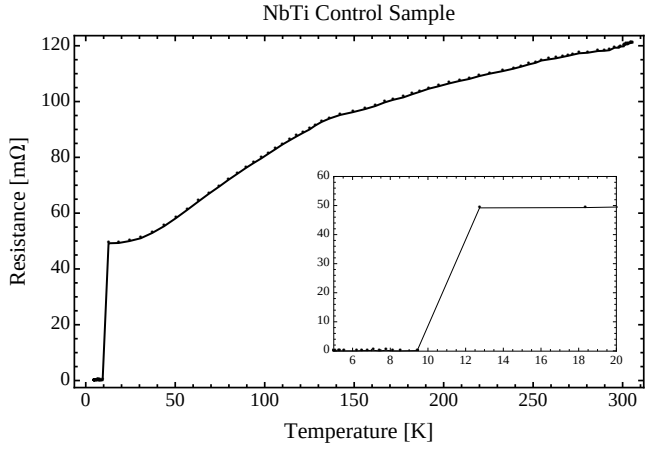

Figure 3.2: Measurement of a superconducting transition of a NbTi single filament wire with the Keithley 2400 source meter.

figure 3.2 shows a control run with a NbTi SC single filament wire, a clear transition

is visible in the region between 8-11 K.

3.4.2 Critical Current, Offset Method

Measurement of the critical current of thin SC films can also be preformed with the Keithley 2400 source meter and the aid of an oscilloscope. The source meter can supply very accurate currents and has a step sweeping feature. The V-I curves can then be recorded with a digital oscilloscope. The procedure for determination of the critical current using the offset method involves fitting the V-I curve data to [39]

$$V = c(I - I_0)^n \tag{3.29}$$

which allows us to determine the value for c and n. We then define a critical voltage V_c which allows us to calculate the critical current using the electric field criterion

$$I_c^{\text{el field}} = \left(\frac{V_c}{c}\right)^{1/n} + I_0. \tag{3.30}$$

Once these values are known, the critical current using the offset method is

$$I_c^{\text{offset}} = I_c^{\text{el field}} - n^{-1}(I_c^{\text{el field}} - I_0), \tag{3.31}$$

and the tangent line at V_c passing through this point is

$$y = mx + b,\ m = \frac{nV_c}{(I_c^{\text{el field}} - I_0)}. \tag{3.32}$$

This technique is best illustrated in figure 3.3 where the critical current was measured of a 50 nm Nb film under the presence of an external magnetic field of 0.1 Tesla.

3.5 SC thin films

Superconducting thin films play an important role in modern day applications. In particular the use of SC films in optomechanic allows for coupling of mechanical resonators with superconducting microresonators [40, 41]. In such systems one may add a thin SC film on an elastic membrane, usually silicon nitride (SiN) in order to couple it to a SC microresonator circuit capacitively. The quality of the SC film is essential to achieve

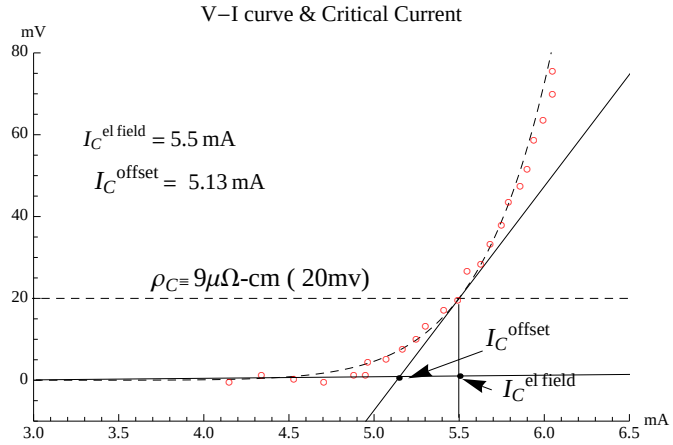

Figure 3.3: Illustration of the offset method for determination of the critical current of a thin Nb film. Dashed line is a fit to equation (3.29), data points are in red circles.

the necessary high quality factors required. Some common materials used in such films are Nb, Al, and TiN which are usually deposited by magnetron sputtering techniques.

Making good quality SC thin films is not a trivial task. Films as thin as 1.2 nanometers deposited on sapphire via molecular beam-epitaxy (MBE) have been achieved in the past [42] . It is generally found that the critical temperature decreases inversely with the thickness of the film for high purity (crystalline) films [43]. However, for typical sputtered Nb films, impurities and film structure contribute to the suppression of the critical temperature [44]. The critical temperature is inversely dependent on the residual resistance [45], and also inversely dependent on the sheet resistance [44]. Thus, in general a good film is one that has a high SC transition temperature. Ideally we would like the film's transition temperature to be as close as possible to the bulk value of the material. A typical figure used in practice is the residual resistance ratio (RRR) which is the ratio of the resistivity at room temperature to the value of resistivity at the transition temperature for the bulk material (about 10K for Nb).

In practice some basic signs of a good film are: resilience, shine, and substrate adhesion. For better chances of a achieving a good quality sputtered SC film one should increase the thickness of the film as much as possible. In addition, there are other factors that have a significant impact such as, sputtering pressure, vacuum capabilities, impurity elimination within the sputtering chamber, ac/dc sputtering, sputtering rate (power), and film substrate. Alternatively, if possible one might also consider molecular beam-epitaxy (MBE), or film evaporation techniques.

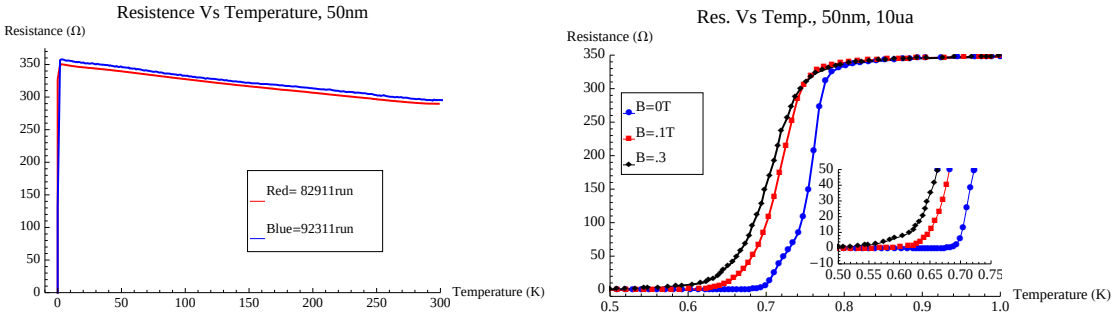

Figure 3.4: (Color) (a) Resistance as a function of temperature for a 50nm Nb film. (b) Resistance as a function of temperature near the transition for different applied external magnetic fields. Critical temperature suppression is a key signature of SC. See section 3.4 for measurement techniques

3.5.1 Nb Films on Microscope Slides

Preliminary efforts in sputtering SC Nb films on standard microscope slides at the Chiao lab have proven successful. The experiments consisted of 50 nm Nb films sputtered at the Chiao lab with a 208HR sputtering system from Ted Pella. Although this sputtering system is not really designed for sputtering Nb SC films, SC films were achieved by reducing the sputtering pressure to about .005 mbar and using the maximum power setting (80ma). It was found that temperature stabilization was an important factor in determining whether the films display SC properties. Figure 3.4 shows the measured resistance as function of temperature and the suppression of the critical temperature due to the presence of an applied external magnetic field, the 50 nm Nb film displayed signs of superconductivity at temperatures just below 1K (measurement techniques as discussed in section 3.4). In addition, some of the first films sputtered at the Chiao lab were observed to become transparent over time. This effect is believed to be due to impurities and poor deposition of Nb film over the substrate which then lead to oxidation of the film when exposed to air. An optical transmission measurement was used to monitor the transmittance through 90 nm films. The transmittance was observed to increase with time. For the films that displayed SC properties, this transmittance saturated over the course of a week as shown in figure 3.5.

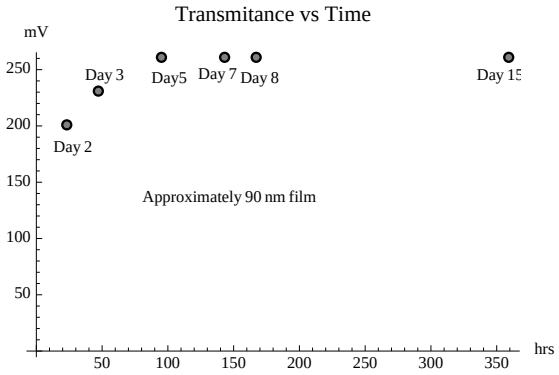

Figure 3.5: Transmisstance of 90nm Nb film sputtered with the 208 HR system monitored for two weeks. The biggest effects take place within the first 48 hrs.

3.5.2 SC Measurement on Thin Films deposited on elastic substrates

Preliminary efforts to obtain good quality SC films on elastic substrates have been made at the Chiao lab in collaboration with the Sharping group at UC Merced. To expedite the test process we have implemented a *dip-stick* four-lead measurement technique that allows us to rapidly test samples for superconductivity. The *dip-stick* method uses our custom made wide-mouth liquid helium cyrofab dewar and is capable of rapidly cooling a small sample to about 4.2K. For electrical contacts we use pogo pins (spring loaded spring contacts) made with berylium copper springs.

The four-lead in-square measurement is used to denote the geometry of the four pressure contacts in a configuration where each contact can be thought to be at a corner of a square. In the past this has worked with the addition of a uniform thin gold film as a equipotential contact surface, however, it is strongly believed that without the addition of a gold film this configuration is not good for testing thin film samples. Figure 3.6 shows the results of a Comsol simulation for the four lead in-square geometry configuration for a resistive Nb film. It is clear that the two voltage sensing leads (near x=y=0, and x=y=1 in figure 3.6) would not only be at an equipotential (assuming film is isotropic) but also in a region of minimum current flow. The potential as a function of displacement from the stimulating input (near x=0,y=1) to the diagonal ground point (near x=1,y=0) is illustrated in figure 3.7a. It is clear that along this diagonal it is the ideal location to place voltage sensing leads. In contrast, figure 3.7b displays the potential as function of displacement from the diagonal formed by the points (x=y=0 to x=y=1), as expected it is constant indicating an equipotential line.

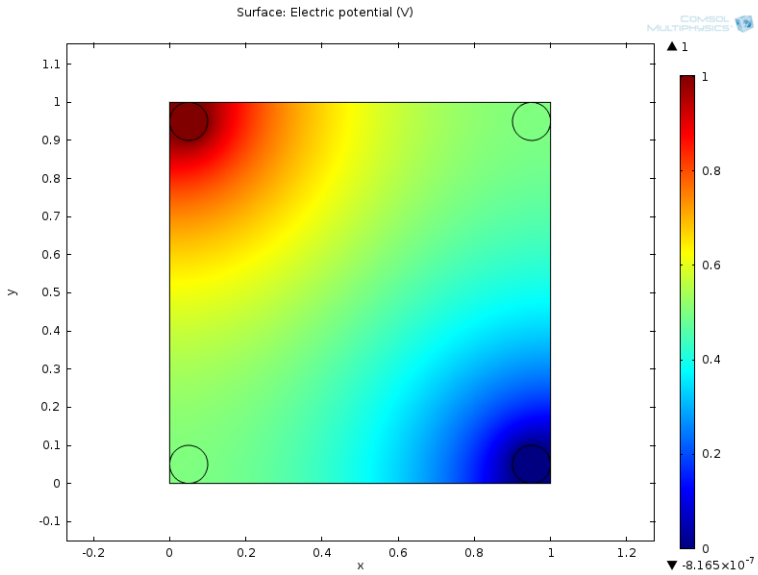

Figure 3.6: Comsol four-lead in-square simulation of a thin film stimulated at the corners with a circular contact. Two sensing leads located near x=y=0 and x=y=1 cannot detect a potential difference and are in a region of minimum current flow.

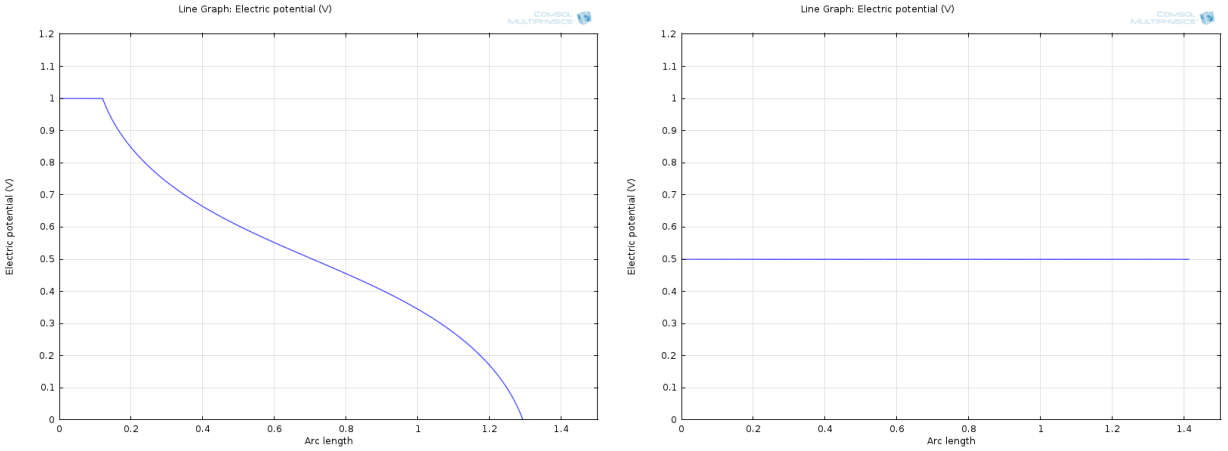

(a) Potential along the diagonal from point (0,1) to (1,0) in figure 3.6.

(b) Potential along the diagonal from point (0,0) to (1,1) in figure 3.6.

Figure 3.7: Plots of potential for a thin isotropic Nb film with a circular electrical contacts along the two diagonals.

Experiments testing three thin Nb films for SC above 4.5K were preformed using our 100L cryofab dewar at the Chiao lab. The four-lead resistance measurements were preformed with a Keithley 2400 source meter and a Labview VI. Note that the Keithley

2400 source meter is not technically capable of measuring resistance below micro-ohm levels, which is required to fully indicate a superconductive state. Nevertheless, a transition can be inferred from the abrupt change in the resistance of the sample as discussed in section 3.4.1.

The first measurement with a 300nm Nb film deposited on a silicon wafer did show evidence of superconductivity. With the in-line wiring configuration a transition was observed somewhere between 6-9K for the 300 nm Nb sample as shown in figure 3.8.

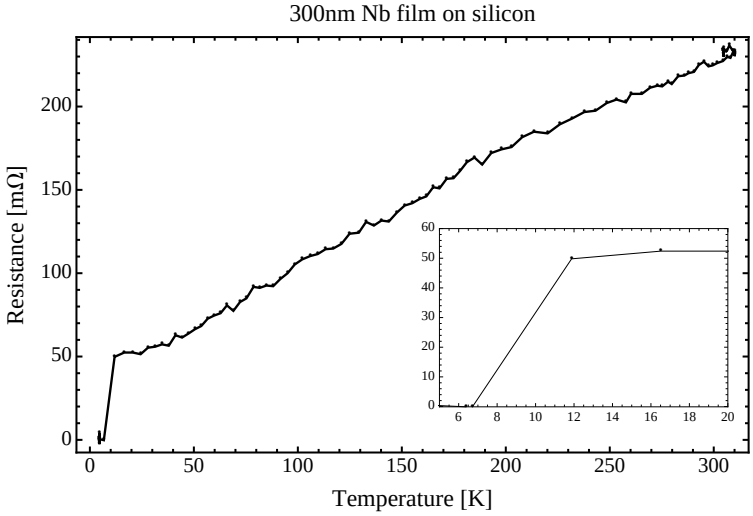

Figure 3.8: A 300 nm Nb film deposited on either bare Si or Si + low stress nitride (5000A thick) Si wafer, 675um thick and boron doped p-type 10ohm-cm resistivity seems to have a SC transition somewhere between 6-9K. The inset is a magnification of the transition region

The second measurement was on a 200nm Nb film deposited on Kapton. The in-line wiring configuration was also used. No sign of superconductivity was observed, data is displayed in figure 3.9.

The third measurement was of a Norcada SiNi window coated with a 200nm Nb film. Due to the delicate 200 nm SiNi window we could not do a four-lead in-line measurement as preformed for the other two samples. The results for this trial are shown in figure 3.10, due to the erratic behavior it is suspected that there was a problem with the four-lead measurement scheme during the cooldown period which made this test inconclusive.

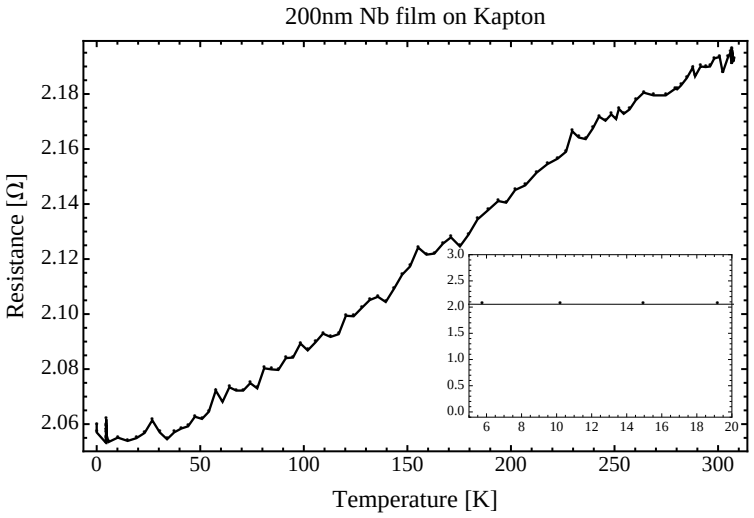

Figure 3.9: 200 nm Nb film deposited on Kapton does not exhibit any sudden changes in resistivity which suggest that no SC transition occurred above 4.5K on this sample. Inset is a magnification of the area of interest.

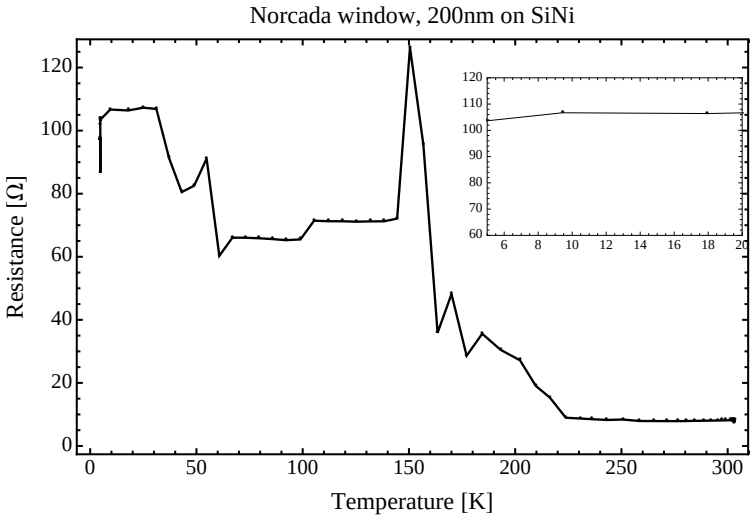

Figure 3.10: Data for Norcada 200nm Nb film deposited on a SiNi window is ruled inconclusive due to the erratic behavior which suggest a problem with the electrical contacts occurred during the cooldown. Inset is a magnification of area of interest.

4

RF Cylindrical Cavity, the Pill Box

The cylindrical (pill box) cavity is a well known problem primarily because of the existence of an analytic solution in terms of the Bessel functions in cylindrical coordinates [46]. The pill box is not often used in practice because it can be impractical to tune over a wide band for particular modes. For example, its first transverse magnetic (TM) resonant mode is independent of the length of the cavity, and only depends on the radius. However, higher order TM and transverse electric (TE) modes do have resonant frequencies that are dependent on the length in which one can use a piston at one end to tune it. Our interest is in exciting TM and TE modes with frequency resonances in the range of our equipment ranging from 1-20 GHz. This chapter begins with a detailed analytic solution to the pill box problem by solving the Maxwell equations in a cylindrical geometry.

4.1 Solution of Maxwell's equations in cylindrical geometry

4.1.1 The Wave Equation

Consider the pill box cavity as shown in figure 4.1, it is evident that the fields within the cylindrical cavity will have cylindrical symmetry along the x and y directions. Assuming that the electromagnetic waves travel along the positive z-direction, the z-dependance

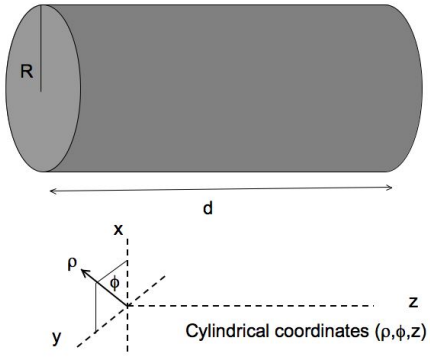

Figure 4.1: The pill box cavity is a hollow metallic cylinder of radius R and length d. Cylindrical coordinates are used as shown, waves are assumed to propagate along the z-direction.

can written explicitly

$$\vec{E}(\vec{x},t) = \vec{E}(\rho,\phi)e^{ikz-i\omega t}, \quad \vec{H}(\vec{x},t) = \vec{H}(\rho,\phi)e^{ikz-i\omega t}. \tag{4.1}$$

Applying the curl to Maxwell's equations

$$\vec{\nabla} \times \vec{E} = -\frac{\partial \vec{B}}{\partial t}, \text{ and } \vec{\nabla} \times \vec{H} = \frac{\partial D}{\partial t}, \tag{4.2}$$

the wave equations follow in the usual manner. In vacuum taking the approximation of a perfect conductor so that $\vec{\nabla} \cdot \vec{E} = 0$and $\vec{\nabla} \cdot \vec{B} = 0$, the fields in (4.1) obey the wave equations

$$\left(\nabla^2 - \frac{1}{c^2}\frac{\partial^2}{\partial t^2}\right)\left\{\begin{array}{c}\vec{E}\\ \vec{H}\end{array}\right\} = 0, \tag{4.3}$$

where it is assumed that the relative permeability and permittivity are both unity[1] (i.e. $\epsilon \equiv \epsilon_0,$ and $\mu \equiv \mu_0$.). Substituting the expressions for the fields in (4.1) into (4.3) and evaluating the exponential gives

$$\nabla_\perp^2 + \left(\frac{\omega^2}{c^2} - k^2\right)\left\{\begin{array}{c}\vec{E}\\ \vec{H}\end{array}\right\} = 0, \tag{4.4}$$

[1]Recall that in linear-homogeneous media (LHM) the $\vec{D}$ and $\vec{H}$ fields obey $\vec{D} = \epsilon\vec{E}$ and $\vec{B} = \mu\vec{H}$.

where

$$\nabla_\perp^2 = \nabla^2 - \frac{\partial^2}{\partial z^2}. \tag{4.5}$$

We now seek to find expressions for the transverse fields ($E_\perp$ and $H_\perp$) as a function of the longitudinal fields (E_z and H_z). Substituting

$$\vec{E}_z = (\hat{z}\cdot\vec{E})\hat{z}, \text{ and } \vec{E}_\perp = (\hat{z}\times\vec{E})\times\hat{z}, \tag{4.6}$$

$$\vec{E} = \vec{E}_\perp + \vec{E}_z, \text{ and } \vec{H} = \vec{H}_\perp + \vec{H}_z, \tag{4.7}$$

into the following Maxwell's equations which have been evaluated with the fields in (4.1)

$$\vec{\nabla}\times\vec{E} = i\omega\mu_0\vec{H} \text{ and } \vec{\nabla}\times\vec{H} = -i\omega\epsilon_0\vec{E}. \tag{4.8}$$

gives a general expression for the transverse fields

$$\begin{aligned}\vec{E}_\perp &= \frac{i}{\epsilon_0\omega}\left[(-\partial_z H_\phi + \partial_\phi H_z)\hat{\rho} + (\partial_z H_\rho - \partial_\rho H_z)\hat{\phi}\right],\\ \vec{H}_\perp &= -\frac{i}{\mu_0\omega}\left[(-\partial_z E_\phi + \partial_\phi E_z)\hat{\rho} + (\partial_z E_\rho - \partial_\rho E_z)\hat{\phi}\right].\end{aligned} \tag{4.9}$$

Equation (4.9) is a system of four equations and four unknowns which can be solved in terms of the z components

$$\begin{aligned}E_\rho &= \frac{1}{\gamma^2}(ik\partial_\rho E_z + \frac{i\omega}{\epsilon_0 c^2}\partial_\phi H_z),\ E_\phi = \frac{1}{\gamma^2}(ik\partial_\phi E_z - \frac{i\omega}{\epsilon_0 c^2}\partial_\rho H_z)\\ H_\rho &= \frac{1}{\gamma^2}(ik\partial_\rho H_z - \frac{i\omega}{\mu_0 c^2}\partial_\phi E_z),\ H_\phi = \frac{1}{\gamma^2}(ik\partial_\phi H_z + \frac{i\omega}{\mu_0 c^2}\partial_\rho E_z).\end{aligned} \tag{4.10}$$

Combining these results with (4.1) and (4.7) gives the expressions for the transverse fields in terms of the z-components

$$\vec{H}_\perp = \frac{1}{\gamma^2}\left[\nabla_\perp\left(\frac{\partial H_z}{\partial z}\right) + \frac{i\omega}{\mu_0 c^2}\hat{z}\times\nabla_\perp E_z\right] \tag{4.11}$$

$$\vec{E}_\perp = \frac{1}{\gamma^2}\left[\nabla_\perp\left(\frac{\partial E_z}{\partial z}\right) - \frac{i\omega}{\epsilon_0 c^2}\hat{z}\times\nabla_\perp H_z\right], \tag{4.12}$$

where

$$\gamma^2 \equiv \frac{\omega^2}{c^2} - k^2. \tag{4.13}$$

4.1.2 The Boundary Conditions

In a perfect the conductor the parallel component of the electric field must vanish within the conductor, $E_{in}^{||} = 0$, and the normal component of the magnetic field must also vanish, $B_{in}^{\perp} = 0$. The boundary conditions are summarized as

$$\begin{aligned} \hat{n} \times \vec{E} &= 0, \\ \hat{n} \cdot \vec{H} &= 0, \end{aligned} \tag{4.14}$$

where $\hat{n}$ is the normal vector perpendicular to the surface. Applying the boundary conditions to the cylindrical cavity gives

$$\begin{aligned} E_z|_s &= 0, \\ (\hat{n} \cdot \nabla_{\perp}) H_z|_s = \partial_n H_z|_s &= 0, \end{aligned} \tag{4.15}$$

where ∂_n is the *normal* derivative. Observe that H_z and E_z are independent quantities, and since the boundary conditions may not (generally) be satisfied simultaneously we can divide the fields into two categories (modes), one for each boundary condition in (4.15). These modes are denoted as transverse magnetic (TM) and transverse electric (TE) modes. A TM mode is one in which the magnetic field is perpendicular to the direction of propagation and similarly a TE mode is one in which the electric field is perpendicular to the direction of propagation. Note that no transverse electromagnetic (TEM) mode is supported in a single cylindrical cavity or waveguide. The two independent modes are extracted by imposing the appropriate boundary conditions

$$\text{TM Modes} \qquad \begin{aligned} B_z &= 0 \text{ everywhere} \\ E_z|_s &= 0, \end{aligned} \tag{4.16}$$

$$\text{TE Modes} \qquad \begin{aligned} E_z &= 0 \text{ everywhere} \\ \partial_n H_z|_s &= 0. \end{aligned} \tag{4.17}$$

A general relation for the transverse fields follows from equations (4.11), (4.12), and the boundary conditions in equations (4.16) and (4.17) for the TM and TE modes, respectively,

$$\vec{H}_{\perp} = \pm \frac{\hat{z} \times \vec{E}_{\perp}}{Z} \quad \text{with;} \qquad \begin{aligned} Z_{TM} &= \frac{k}{\epsilon_0 \omega} \\ Z_{TE} &= \frac{\mu_0 \omega}{k}, \end{aligned} \tag{4.18}$$

where Z is the impedance for the corresponding mode, the positive value is taken for forward traveling waves, and the negative for backward traveling waves. Combining the boundary conditions in (4.16), (4.17) along with (4.11), (4.12) and using (4.18), the transverse fields for the the TM modes become

$$\vec{E}_\perp = \pm\frac{ik}{\gamma^2}\nabla_\perp E_z \tag{4.19}$$

$$\vec{H}_\perp = \pm\frac{i\omega}{\mu_0 c^2}\hat{z}\times\nabla_\perp E_z, \tag{4.20}$$

and similarly the transverse fields for the TE modes

$$\vec{E}_\perp = \mp\frac{i\omega}{\epsilon_0 c^2}\hat{z}\times\nabla_\perp H_z \tag{4.21}$$

$$\vec{H}_\perp = \pm\frac{ik}{\gamma^2}\nabla_\perp H_z. \tag{4.22}$$

4.1.3 The Resonant Cylindrical Cavity

Up to this point equations (4.19)-(4.22) are general expressions in terms of the z-components and summarize the results for the transverse electromagnetic fields in a cylindrical waveguide. Hence, to arrive at full solution for the fields we now seek explicit expressions for E_z and B_z. Furthermore, in order to find appropriate expressions for the cylindrical cavity we must generalize the fields to include forward and backward traveling waves. This is accomplished by noting that the cavity, shown in figure 4.1, will create standing waves from the superposition of backward and forward traveling waves. Hence, E_z is expected to have the form of

$$E_z \propto \psi'(\rho,\phi)\sin(kz) + \psi(\rho,\phi)\cos(kz). \tag{4.23}$$

Applying the boundary conditions in equation (4.16) it is required that $E_\perp(0) = E_\perp(d) = 0$, and from (4.19) we find for TM modes

$$\vec{E}_z(\vec{x},t) = \psi(\rho,\phi)\cos(kz)e^{-i\omega t},\ k = \frac{p\pi}{d},\ p = 0,1,2\cdots \tag{4.24}$$

and similarly applying the boundary conditions for the TE modes in equation (4.17) it is required that $H_z(0) = H_z(d) = 0$, and from (4.22) we find for TE modes

$$H_z(\vec{x}, t) = \psi(\rho, \phi) \sin(kz) e^{-i\omega t},\ k = \frac{p\pi}{d},\ p = 1, 2, 3 \cdots, \tag{4.25}$$

where an analogous linear superposition as in equation (4.23) has been used but for the magnetic field.

Applying these results for the z-components, the transverse fields in equations (4.19)-(4.22) are now expressed[2] in terms of the function $\psi(\rho, \phi)$

$$\text{TM Modes:} \qquad E_\perp = -\frac{p\pi}{d\gamma_j^2} \sin(\frac{p\pi z}{d}) \nabla_\perp \psi(\rho, \phi), \tag{4.26}$$

$$H_\perp = \frac{i\omega_j}{\eta c \gamma_j^2} \cos(\frac{p\pi z}{d}) \hat{z} \times \nabla_\perp \psi(\rho, \phi), \tag{4.27}$$

$$\text{TE Modes:} \qquad E_\perp = -\frac{i\eta\omega_j}{c\gamma_j^2} \sin(\frac{p\pi z}{d}) \hat{z} \times \nabla_\perp \psi(\rho, \phi), \tag{4.28}$$

$$H_\perp = \frac{p\pi}{d\gamma_j^2} \cos(\frac{p\pi z}{d}) \nabla_\perp \psi(\rho, \phi), \tag{4.29}$$

where $\eta \equiv \sqrt{\mu_0/\epsilon_0}$ is the impedance of free space. In addition, since E_z and H_z also satisfy the wave equation in (4.4), it follows that ψ satisfies the following eigenvalue equation

$$\left[\nabla_\perp^2 + \gamma_j^2\right] \psi(\rho, \phi) = 0, \quad \gamma_j^2 \equiv \left(\frac{\omega_j}{c}\right)^2 + \left(\frac{p\pi}{d}\right)^2, \tag{4.30}$$

where γ_j^2 is the j^{th} eigenvalue of the eigenvalue equation. For each value of p the eigenvalue γ_j^2 determines an eigenfrequency of resonance frequency ω_j. The solution to the wave equation for the electromagnetic fields in the cylindrical cavity has now been reduced to solving the eigenvalue equation in (4.30).

[2]Note that upon using trigonometric functions instead of the plane wave exponential (e^{ikz}) a derivative must be taken into account as indicated by the factor ik, hence the replacement $\cos(kx) \to \sin(kx)$ and vice versa.

4.1.4 The PDE

We have successfully reduced the solution to Maxwell's equations for the electromagnetic fields in the cavity into solving a single, well known, partial differential equation for ψ. The neat thing about this approach is that a solution for ψ will immediately give us the fields for both TE and TM modes via equations (4.26)-(4.29). In cylindrical coordinates

$$\nabla_\perp = \frac{1}{\rho}\partial_\rho(\rho\partial_\rho) + \frac{1}{\rho^2}\partial_\phi^2, \tag{4.31}$$

and using separation of variables with $\psi = R(\rho)\Phi(\phi)$ equation (4.30) becomes

$$\rho^2\left[\frac{1}{\rho R}\partial_\rho(\rho\partial_\rho R) + \gamma_j^2\right] + \left[\frac{1}{\Phi}\partial_\phi^2\Phi\right] = 0. \tag{4.32}$$

Because each term is a function of a different independent variable, the only way they can add up to zero is if each term is equal to a constant such that their sum is equal to zero. To wit, if

$$f(\rho) + g(\phi) = 0, \tag{4.33}$$

then it is required that $f(\rho) = c_1$ and $g(\phi) = c_2$ such that

$$c_1 + c_2 = 0. \tag{4.34}$$

Hence, the PDE reduces into two ODE's

$$\rho^2\left[\frac{1}{\rho R}\frac{d}{d\rho}(\rho\frac{dR}{d\rho}) + \gamma_j^2\right] = c_1, \tag{4.35}$$

$$\left[\frac{1}{\Phi}\frac{d^2\Phi}{d\phi^2}\right] = c2. \tag{4.36}$$

To obtain sinusoidal solutions fo rΦ lets choose $c_1 = m^2$, and after some simplification on the ODE for R we find

$$\frac{d^2R}{dx^2} + \frac{1}{x}\frac{dR}{dx} + \left(1 - \left(\frac{m}{x}\right)^2\right)R = 0, \quad x_m \equiv \rho\gamma_m, \tag{4.37}$$

$$\frac{d^2\Phi}{d\Phi^2} = -m^2\Phi, . \tag{4.38}$$

Notice that the index in γ_j has been redefined to match the the index m of Bessel's differential equation in equation (4.37). The well known solution to (4.37) is given by the Bessel functions of the first kind of order m which are denoted by $J_m(x_m)$. The solution to equation (4.38) is $\Phi = e^{\pm im\phi}$. Therefore, the complete solution to the eigenvalue equation in (4.30) is

$$\psi(\rho, \phi) = J_m(x_m)e^{\pm im\phi}, \quad x_m \equiv \gamma_m \rho. \tag{4.39}$$

4.1.5 The TM and TE Fields

With the general solution in (4.39) and the application of the appropriate boundary conditions explicit expressions for the TM and TE fields are now obtained. We begin with the TM modes. From equations (4.39), (4.26), and the boundary conditions in (4.16) it is required that

$$J_m(x_m)|_s = 0, \quad x_m|_s = R\gamma_m. \tag{4.40}$$

A new index(n) is introduced to account for the many zeroes of the Bessel funtions, Hence, x_{mn} is defined such that it satifies

$$J_m(x_{mn}) = 0, \quad x_{mn} \equiv R\gamma_{mn}, \tag{4.41}$$

where x_{mn} is the n^{th} root to $J_m(x_{mn}) = 0$. Notice that this also necessitates adding a new index to the eigenvalue, $\gamma_m \rightarrow \gamma_{mn}$. The TM fields are computed from (4.24),

(4.26), and (4.27) directly. We find

TM Modes:

$$
\begin{aligned}
E_z &= E_0 J_m(\frac{x_{mn}}{R}\rho)\cos(m\phi)\cos(\frac{p\pi}{d}z)e^{-i\omega t} \\
E_\rho &= -E_0 \frac{p\pi R}{dx_{mn}} J'_m(\frac{x_{mn}}{R}\rho)\cos(m\phi)\sin(\frac{p\pi}{d}z)e^{-i\omega t} \\
E_\phi &= E_0 \frac{mp\pi R^2}{dx_{mn}^2}\frac{1}{\rho} J_m(\frac{x_{mn}}{R}\rho)\sin m\phi \sin(\frac{p\pi}{d}z)e^{-i\omega t} \\
H_\rho &= iE_0 \frac{m\omega_{mnp}R^2}{\eta c x_{mn}^2}\frac{1}{\rho} J_m(\frac{x_{mn}}{R}\rho)\sin(m\phi)\cos(\frac{p\pi}{d}z)e^{-i\omega t} \\
H_\phi &= iE_0 \frac{\omega_{mnp}R}{\eta c x_{mn}} J'_m(\frac{x_{mn}}{R}\rho)\cos(m\phi)\cos(\frac{p\pi}{d}z)e^{-i\omega t} \\
H_z &\equiv 0 \\
\gamma_{mn} &= \frac{x_{mn}}{R}, \quad \omega_{mnp} = c\sqrt{\gamma_{mn}^2 + \left(\frac{p\pi}{d}\right)^2}, \quad p = 0, 1, 2\cdots \\
J_m(x_{mn}) &= 0, \quad J'_m(x) = \frac{d}{dx}J_m,
\end{aligned}
\tag{4.42}
$$

where it is of extreme importance to note that the chain rule has already been applied to the derivatives of the Bessel functions. To wit,

$$
J'_m(\frac{x_{mn}}{R}\rho) = \frac{d}{dx}J_m(x);\ x \equiv \frac{x_{mn}\rho}{R}, \tag{4.43}
$$

and not

$$
J'_m(\frac{x_{mn}\rho}{R}) = \frac{d}{d\rho}J_m(\frac{x_{mn}}{R}\rho). \tag{4.44}
$$

Expressions for the TE fields follow in an analogous manner, with the distinction that the boundary conditions for TE modes in equation (4.17) give

$$
J'_m(x'_m)\big|_s = 0, \quad x'_m\big|_s = R\gamma_m, \tag{4.45}
$$

where here x'_{mn} is defined to be the n$^{\text{nt}}$ root of $J'_m(x'_{mn})$ and satisfies

$$
J'_m(x'_{mn}) = 0. \tag{4.46}
$$

From (4.25), (4.28), and (4.29) the TE fields are

TE Modes:

$$
\begin{aligned}
H_z &= H_0 J_m(\frac{x'_{mn}}{R}\rho)\cos(m\phi)\sin(\frac{p\pi}{d}z)e^{-i\omega t} \\
H_\rho &= H_0 \frac{p\pi R}{dx'_{mn}} J'_m(\frac{x'_{mn}}{R}\rho)\cos(m\phi)\cos(\frac{p\pi}{d}z)e^{-i\omega t} \\
H_\phi &= -H_0 \frac{mp\pi R^2}{dx'^2_{mn}}\frac{1}{\rho} J_m(\frac{x'_{mn}}{R}\rho)\sin(m\phi)\cos(\frac{p\pi}{d}z)e^{-i\omega t} \\
E_\rho &= -iH_0 \frac{m\eta\omega_{mnp}R^2}{cx'^2_{mn}}\frac{1}{\rho} J_m(\frac{x'_{mn}}{R}\rho)\sin(m\phi)\sin(\frac{p\pi}{d}z)e^{-i\omega t} \\
E_\phi &= -iH_0 \frac{\eta\omega_{mnp}R}{cx'_{mn}} J'_m(\frac{x'_{mn}}{R}\rho)\cos(m\phi)\sin(\frac{p\pi}{d}z)e^{-i\omega t} \\
E_z &\equiv 0 \\
\gamma'_{mn} &= \frac{x'_{mn}}{R}, \quad \omega'_{mnp} = c\sqrt{\gamma'^2 + \left(\frac{p\pi}{d}\right)^2}, \quad p = 1, 2, 3\cdots \\
J'_m(x'_{mn}) &= 0, \quad J'_m(x') = \frac{d}{dx'}J_m(x'),
\end{aligned}
\tag{4.47}
$$

where once again care must be taken in noting that no chain rule is necessary in differentiating the Bessel functions. The use of the eigenvalue γ' is chosen for the TE modes so that it is not confused with the eigenvalue γ, which is used for the TM modes. Each set of modes has different set of resonance frequencies, ω_{mnp} for TM modes, and ω'_{mnp} for TE modes. Finally, the modes are classified by the nomenclature TM_{mnp} for TM modes , and TE_{mnp} for TE modes. Here m, n, and p corresponds to the number of half wavelengths (or sign changes) along the azimuthal direction (ϕ), radial direction (ρ), and the axial direction (z), respectively.

4.2 Quality Factors of the Cylindrical Cavity: The "Q"

The quality factor (Q) is roughly 2π times the number of rf cycles it takes to dissipate the energy stored in the cavity. That is, it measures how "good" the efficiency of the cavity is. A high Q means that the "ring down" time of an excitation takes a long time to decay. The Q is defined as

$$
Q \equiv \omega_0 \frac{U}{P_c}, \tag{4.48}
$$

where U is the energy stored in the cavity, P_c is the power loss in the cavity walls, and ω_0 is the frequency of interest. In a cavity with no external losses the power dissipated is equal to the rate of change of the stored energy in the cavity

$$P_c = -\frac{dU}{dt}. \tag{4.49}$$

From equations (4.48) and (4.49) we can write a differential equation whose solution shows that any initial energy stored in the cavity will decay exponentially with a time scale on the order of $\tau \sim Q_0/\omega_0$, that is

$$\frac{dU}{dt} = -\frac{\omega_0}{Q}U \;\Rightarrow\; U = U_0 e^{-\frac{\omega_0 t}{Q}}. \tag{4.50}$$

Since the energy U is proportional to E^2, the magnitude of the electric field must also decay with time

$$E = E_0 e^{-\frac{1}{2}\frac{\omega_0 t}{Q}} e^{-i\omega_0 t}. \tag{4.51}$$

Furthermore, because voltage is proportional to electric field and voltages are easily measured in practice, we define the time constant $\tau \equiv \frac{2Q}{\omega_0}$. With this definition the above expression can now be written as

$$E = (E_0 e^{-i\omega_0 t}) e^{-\frac{t}{\tau}}. \tag{4.52}$$

Calculation of the Q requires explicit calculations of the energy stored in the fields (U), and the power loss (P_c). Given the nature of the expression for the TM and TE fields this can be a tedious task. However, for our purposes we are only interested on the lowest TM and TE modes, and so, we restrict the calculations to the TM_{010}, TE_{111}, and the TE_{011} modes.

The total time-averaged electromagnetic energy in the cavity is

$$U = \frac{1}{2}\mu_0 \int_V |\vec{H}|^2 dV = \frac{1}{2}\epsilon_0 \int_V |\vec{E}|^2 dV. \tag{4.53}$$

The power loss associated with the cavity is [29]

$$P_c = \frac{1}{2}R_s \int_S |\vec{H}_{||}|^2 da, \tag{4.54}$$

where $\vec{H}_{||}$ is the parallel component at the surface[3] and R_s is defined to be the surface resistance which will be computed later.

We begin by calculating the total energy (U) for the TM_{010} mode. To keep track of quantities and avoid confusion within the TE and TM modes we will denote all quantities with the subscript corresponding to their type of mode. For example, U_{TM010} is the energy for the TM_{010} mode, and U_{TE111} is the energy for the TE_{111}mode, etc.. From section 4.1.5 the fields for the TM_{010} mode are

$$\text{TM}_{010}: \quad \begin{aligned} E_z &= E_0 J_0(\frac{x_{01}}{R}\rho)e^{-i\omega t} \\ H_\phi &= -i\frac{E_0}{\eta}J_1(\frac{x_{01}}{R}\rho)e^{-i\omega t}, \end{aligned} \tag{4.55}$$

all other fields vanish. For convenience lets use H to calculate the total energy, from equation (4.53)

$$\begin{aligned} U_{TM010} &= \frac{1}{2}\mu_0 \int_V (\frac{E_0}{\eta})^2 J_1^2(\frac{x_{01}}{R}\rho)dV \\ &= \frac{1}{2}\mu_0(\frac{E_0}{\eta})^2 \int_0^{2\pi} d\phi \int_0^d dz \int_0^R \rho J_1^2(\frac{x_{01}}{R}\rho)d\rho \\ &= \frac{E_0^2\mu_0\pi d}{\eta^2}\int_0^R \rho J_1^2(\frac{x_{01}}{R}\rho)d\rho \end{aligned} \tag{4.56}$$

The integral in (4.56) can be evaluated with the following relation

$$\int \rho J_m^2(\alpha\rho)d\rho = \frac{\rho^2}{2}[J_m^2(\alpha\rho) - J_{m-1}(\alpha\rho)J_{m+1}(\alpha\rho)]. \tag{4.57}$$

Therefore, the total time-average electromagnetic energy in a cylindrical cavity of length (d) and radius (R) excited with a TM_{010} mode is

$$U_{TM010} = E_0^2 \frac{\pi d\epsilon_0 R^2}{2} J_1^2(x_{01}), \tag{4.58}$$

where we have used the fact that $J_0(x_{01}) = 0$, since by definition x_{01} is the first root

[3]More generally we can summarize the boundary conditions by defining a surface current $K_{eff} = \vec{n} \times \vec{H}_{||}$, and the power is $dP_c = 1/2R_s|\vec{K}_{eff},|^2$da, where R_s is the surface resistance. However, this is just to keep track of the boundary condition. We are okay to use (4.54) so long we realize that the fields must be evaluated at the surface.

of J_0. The power loss (P_c) is calculated from equation (4.54),

$$P_c = \frac{1}{2}R_s \int_S |\vec{H}_{||}|^2 da = \frac{E_0^2 R_s}{2\eta^2} \int_S J_1^2(\frac{x_{01}}{R}\rho) da. \tag{4.59}$$

The integral must be evaluated over all the interior surfaces of the cavity, which include the two end-faces ($z = 0$, and $z = d$) and the cylindrical surface ($\rho = R$). Hence, the integral in (4.59) becomes

$$\begin{aligned} \int_S J_1^2(\frac{x_{01}}{R}\rho) da &= 2\int_0^R \rho J_1^2(\frac{x_{01}}{R}\rho) d\rho \int_0^{2\pi} d\phi + RJ_1^2(x_{01}) \int_0^d dz \int_0^{2\pi} d\phi \\ &= 2\pi J_1^2(x_{01})[R^2 + Rd] \end{aligned} \tag{4.60}$$

Plugging this result for the integral back into equation (4.59) gives the power loss,

$$P_c = \frac{E_0^2 R_s \pi}{\eta^2} J_1^2(x_{01}) R(R + d). \tag{4.61}$$

Substituting the results for U_{TM010} and P_c into equation (4.48) the Q for the TM_{010} mode is

$$Q = \frac{\omega_0 \mu_0 d}{2R_s(1 + \frac{d}{R})}. \tag{4.62}$$

We will return to this equation once we find an explicit expression for the surface resistance R_s.

Similarly, to calculate the Q for the TE_{111} mode, lets begin with the energy U_{TE111}. Using the expressions for the TE fields in (4.47)

$$\begin{aligned} U_{TE} &= \frac{1}{2}\epsilon_0 \int_V |\vec{E}|^2 dV \\ &= \frac{1}{2}\epsilon_0 H_0^2 \left(\frac{\eta\omega_{111}R^2}{cx_{11}'^2}\right)^2 \int_0^R \frac{1}{\rho^2} J_1^2(\frac{x_{11}'}{R}\rho)\rho d\rho \int_0^d \sin^2(\frac{\pi z}{d}) dz \int_0^{2\pi} \sin^2(\phi) d\phi \\ &\quad + \frac{1}{2}\epsilon_0 H_0^2 \left(\frac{\eta\omega_{111}R}{cx_{11}'}\right)^2 \int_0^R J_1'^2(\frac{x_{11}'}{R}\rho)\rho d\rho \int_0^d \sin^2(\frac{\pi z}{d}) dz \int_0^{2\pi} \cos^2(\phi) d\phi. \end{aligned} \tag{4.63}$$

Let us put the evaluation of the integrals above on hold for a bit so they can "sink in". Actually, one can imagine that the evaluation of P_c will have similar integrals, so being patient might save us from having to solve the same integrals twice. The power loss from the TE_{111} mode follows from equation (4.54) and the expression for the TE fields

in (4.47),

$$\begin{aligned} P_c &= \frac{1}{2}R_s \int_S |\vec{H}_{||}|^2 da \\ &= \frac{H_0^2}{2}\int_S \left[(\frac{\pi R}{dx'_{11}})^2 J_1'^2(\frac{x'_{11}}{R}\rho)\cos^2(\phi)\cos^2(\frac{\pi z}{d}) \right. \\ &\left. +(\frac{\pi R^2}{dx'^2_{11}})^2 \frac{1}{\rho^2} J_1^2(\frac{x'_{11}}{R}\rho)\sin^2(\phi)\cos^2(\frac{\pi z}{d}) + J_1^2(\frac{x'_{11}}{R}\rho)\cos^2(\phi)\sin^2(\frac{\pi z}{d}) \right] da. \end{aligned} \tag{4.64}$$

As before be must split this integral over all the interior surfaces of the cavity, the two end-faces and the cylindrical surface. For clarity lets separate the integrals involving the end-faces and the cylindrical surface. For the ends ($z = 0$)

$$\int_{ends}[\cdots]da = \tag{4.65}$$
$$2H_0^2\left[(\frac{\pi R}{dx'_{11}})^2 \int_0^R \rho J_1'^2(\frac{x'_{11}}{R}\rho)d\rho \int_0^{2\pi}\cos^2(\phi)d\phi + (\frac{\pi R^2}{dx'^2_{11}})^2 \int_0^R \frac{1}{\rho}J_1(\frac{x'_{11}}{R}\rho)d\rho \int_0^{2\pi}\sin^2(\phi)d\phi\right].,$$

and for the cylindrical surface ($\rho = R$)

$$\int_{cyln}[\cdots]da = \tag{4.66}$$
$$H_0^2 J_1^2(x'_{11})\left[(\frac{\pi R^2}{dx'^2_{11}})^2 \frac{1}{R}\int_0^d \cos^2(\frac{\pi z}{d})dz \int_0^{2\pi}\sin^2(\phi)d\phi + R\int_0^d \sin^2(\frac{\pi z}{d})dz\int_0^{2\pi}\cos^2(\phi)d\phi\right].$$

The trigonometric integrals are straightforward

$$\int_0^{2\pi}\cos^2(\phi)d\phi = \int_0^{2\pi}\sin^2(\phi)d\phi = \pi, \tag{4.67}$$
$$\int_0^d \cos^2(\frac{\pi z}{d})dz = \int_0^d \sin^2(\frac{\pi z}{d})dz = \frac{d}{2}. \tag{4.68}$$

Notice that our patience has paid off in that both P_c and U_{TE111} have the same type of integrals involving Bessel functions. For this reason let us define

$$\xi = \int_0^R \frac{1}{\rho}J_1^2(\frac{x'_{11}}{R}\rho)d\rho + (\frac{x'_{11}}{R})^2\int_0^R J_1'^2(\frac{x'_{11}}{R}\rho)d\rho, \tag{4.69}$$

and use the previous results to evaluate the trigonometric integrals to U_{TE111} in (4.63)

as

$$U_{TE} = \frac{H_0^2 \epsilon_0}{2} \left(\frac{\eta \omega_{111} R^2}{c x_{11}'^2} \right)^2 \frac{\pi d}{2} \xi. \tag{4.70}$$

Similarly, after adding the "ends" and "cyln" terms together and evaluating the trigonometric integrals, P_c becomes

$$P_c = H_0^2 R_s \pi \left(\frac{\pi R^2}{d x_{11}'} \right)^2 \left[1 + \frac{J_1^2(x_{11}') d}{4 R \xi} \left(1 + \left(\frac{x_{11}'^2 d}{\pi R} \right)^2 \right) \right] \xi. \tag{4.71}$$

The Q for the TE_{111} mode now follows from equation (4.48)

$$Q_{TE111} = \frac{1}{R_s} \frac{d^3 \epsilon_0 \eta^2 \omega_{111}^3}{4\pi^2 c^2} \frac{1}{\left[1 + \frac{J_1^2(x_{11}')}{4\xi} \frac{d}{R} + \frac{J_1^2(x_{11}') x_{11}'^4}{4\pi^2 \xi} (\frac{d}{R})^3 \right]}. \tag{4.72}$$

The hard work has been done, all that is left is to evaluate ξ and find and expression for R_s. In this manner the Q's can be calculated for any mode of the cylindrical cavity.

4.3 Surface Resistance

Applying Ohm's law ($J = \sigma E$) to the surface of a conductor yields the definition for surface impedance

$$Z_s = \frac{E_s}{I}, \tag{4.73}$$

where I is the total current, and E_s is the electric field at the surface. The surface resistance (R_s), which is defined as the *real* part of the surface impedance, can now be extracted by finding explicit expressions for E and I. Let us begin with the electric field at the surface. For sinusiodal fields ($E = E_0 e^{-i\omega t}$) and good conductors ($\sigma >> \epsilon_0 \omega$) the wave equation becomes

$$\nabla^2 E = \beta^2 E, \quad \beta^2 \equiv i\omega\sigma\mu_0. \tag{4.74}$$

For simplicity consider a planar conductor slab placed in the y-z plane, and assume a uniform electric field (E) points along the z-direction so that variations of E are restricted to the x-direction. Solving the differential equation for the electric field in

this geometry gives

$$E_z = E_0 e^{-\frac{x}{\delta}} e^{-i\frac{x}{\delta}}, \tag{4.75}$$

$$\delta \equiv \frac{\sqrt{2}}{\sqrt{\omega\mu_0\sigma}}, \tag{4.76}$$

where δ is the skin depth and is a measure of the distance the electric field penetrates the surface of the conductor. Likewise, from Ohm's law a similar expression follows for J,

$$J_z = J_0 e^{-\beta x}. \tag{4.77}$$

The total current is

$$I = \int_0^\infty J_0 e^{-\beta x} dx = \frac{J_0}{\beta}, \tag{4.78}$$

and the surface impedance follows from equation (4.73),

$$Z_s = \frac{E}{I} = \frac{\sqrt{2}}{2}\left(\frac{\sqrt{\omega\mu_0\sigma}}{\sigma} + i\frac{\sqrt{\omega\mu_0\sigma}}{\sigma}\right) = R_s + iX_s, \tag{4.79}$$

where we have used the identity $\sqrt{i} = \frac{\sqrt{2}}{2}(1+i)$, and Ohm's law. The surface resistance, defined as the *real* part of the surface impedance, can now be read off as

$$R_s = \frac{1}{\sigma\delta}, \tag{4.80}$$

with the definition of the skin depth as defined in (4.76).

4.4 Summary of Calculation and Main Results

We have calculated in detail the TE, TM modes, and Q for a cylindrical cavity of Radius R and length d. Since we are interested in the lowest modes, we focus our attention to the TM_{010} and TE_{111} modes. These modes yield the lowest resonance frequencies which are of interest. The zeroes of the Bessel functions can be looked up and we find

$$x_{01} = 2.405,\ x'_{11} = 1.841,\ \text{and}\ x'_{01} = x_{11} = 3.8317. \tag{4.81}$$

The relevant fields for the TM_{010} mode are

$$\mathrm{TM}_{010}: \quad \begin{aligned} E_z &= E_0 J_0(\frac{2.405}{R}\rho)e^{-i\omega t} \\ H_\phi &= -i\frac{E_0}{\eta}J_1(\frac{2.405}{R}\rho)e^{-i\omega t}, \end{aligned} \tag{4.82}$$

all other fields vanish, and the resonant frequency is

$$\omega_{010} = \frac{2.405c}{R}. \tag{4.83}$$

For the TE modes the relevant fields can be obtained from (4.47), and the resonant frequencies are

$$\omega'_{111} = 1.841\frac{c}{R}\sqrt{1 + 2.912\left(\frac{R}{d}\right)^2}, \tag{4.84}$$

$$\omega'_{011} = 3.832\frac{c}{R}\sqrt{1 + .672\left(\frac{R}{d}\right)^2}, \tag{4.85}$$

for the TE_{111} and the TE_{011} modes, respectively.

In section 4.3 we found an expression for the surface resistance (R_s), which is used to re-express the Q's in (4.62) and (4.72). For the TM010 mode

$$Q_{TM} = \frac{d}{\delta}\frac{1}{[1 + \frac{d}{R}]}, \tag{4.86}$$

and for the TE_{111}

$$Q_{TE} = \frac{1}{2}\frac{d}{\delta}\frac{\left(1 + .343(\frac{d}{R})^2\right)}{\left[1 + .209\frac{d}{R} + .243(\frac{d}{R})^3\right]}, \tag{4.87}$$

where $J_1^2(x'_{11}) = .3385$, and the evaluation for ξ is done in *Mathematica*,

$$\xi = .404547. \tag{4.88}$$

The Q factor for the TE_{011} mode is

$$Q_{TE011} = \frac{0.610\lambda}{\delta}\frac{\left(1 + 0.168\left(\frac{2R}{d}\right)^2\right)^{3/2}}{1 + 0.168\left(\frac{2R}{d}\right)^3}, \tag{4.89}$$

where R is the radius, d is the length of the cavity, $\delta = (1/2\pi)(\sqrt{(10^3\rho/f)})$ is the skin depth in cm, and λ is the wavelength.

Finally, for most RF applications obtaining a high quality factor (Q) is of utter importance. From the definition of the quality factor in an RF cavity it is apparent that minimizing losses is a practical goal when attempting to achieve high Q's. However, apart from the technical aspects it is also important to point out intrinsic limitations on the quality factor such as those caused by the mode shape (geometrical) factor. It is fruitful to point out that the Q can also be written in the form of

$$Q \propto \frac{\text{Cavity Volume}}{S\delta} \times \text{geometrical factor}, \tag{4.90}$$

where S is the total interior surface area of the cavity, and δ is the skin depth. The geometrical factor is an intrinsic property of the particular mode, and arises from the integration of the particular mode over the geometry of the cavity, hence, it varies for different modes. For example, the TE_{011} mode has a high geometrical factor and naturally leads to higher Q's in RF cylindrical cavities. Also, in this form the Q is the ratio of the volume occupied by the fields in the cavity to the volume that the fields penetrate into the conductor. In fact, since it is within the skin depth that conductors with finite conductivity exhibit ohmic loss, the amount of volume that the fields penetrate into the conductor is directly related to degradation of the quality factor.

4.5 RF Measurements and Cavity Construction

Now that a general formulation has been developed for the relevant quantities for RF cylindrical cavities, we turn to some practical implementation. In particular, the cylindrical cavities used in our preliminary experiments are made from copper and aluminum. The following sections play an important role, as these cavities are used in experimentation in the subsequent chapters.

4.5.1 Making of Copper Cavities

The first type of RF cylindrical cavities built at the Chiao lab were made from standard 1" plumbing-grade copper tubing available at the local hardware store. End-plates were attached by soldering copper end-plates to a small section of copper pipe. The soldering

was preform a with benzene gas torch, 60Sb40Pb solder, and a standard flux paste to ensure solder flow for proper bonding. SMA RF couplers were also attached by the same soldering technique. However, coupler placement and design play an important role, and great care must be taken when coupling to particular modes. For placement determination of the SMA couplers the following references are helpful [46, 47]. Figure 4.2 shows a copper cavity with no couplers attached. This type of cavity is extremely easy an economical to build, however at the sacrifice of high quality factors.

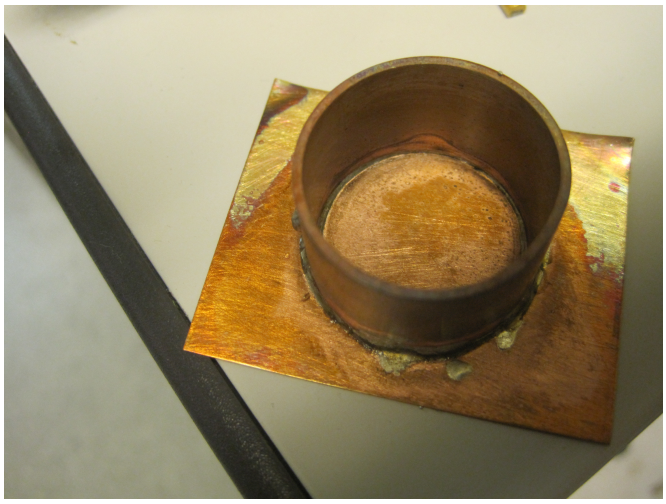

Figure 4.2: A typical copper cylindrical cavity made from 1" copper tubing. No couplers are attached yet, and missing one end-plate.

4.5.2 Making of Aluminum Cavities

Although the copper cavities are easy and economical to build, they become troublesome when higher Q values are desired. The reason for this is primarily in the limited flexibility in tuning the couplers. To achieve a more robust RF cylindrical cavity we designed and built an aluminum cavity. The new design, shown in figure 4.3a, allows for precise tuning of the input and output couplers which ultimately leads to higher Q values. Specifically, the cavity was made from of aluminum alloy 6061, which recently has been used to build high-Q superconducting RF (SRF) cavities [48]. Figure 4.3b shows the completed aluminum cavity, machined and assembled at UC Merced. Calculations using the formalism developed in the previous section predict a Q factor up to 3×10^4 at room temperature.

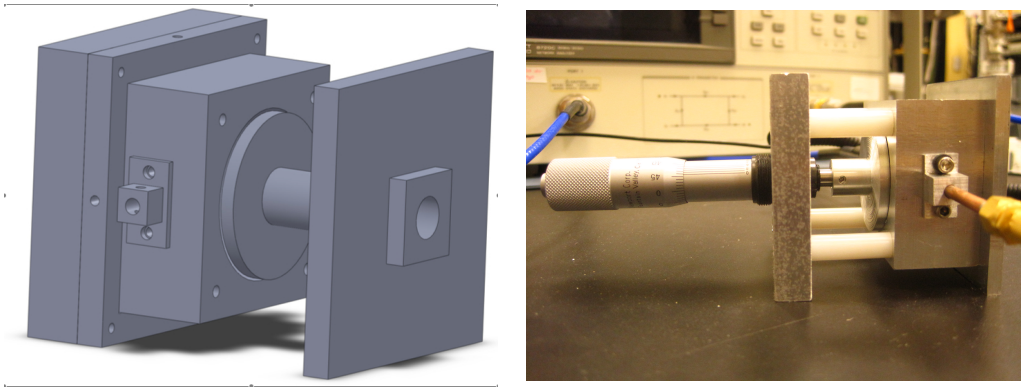

(a) Cavity design prototype.

(b) Aluminum 6061 tunable cavity.

Figure 4.3: Aluminum 6061 RF cylindrical cavity. This particular aluminum (alloy 6061) cavity has been designed and built for preliminary test of cavity Q values, coupling parameters, membrane coupling, mode splitting, and SRF experimentation.

4.6 Splitting the degeneracy of the TE_{011} and TM_{111} modes

It will be of practical interest to break the degeneracy that exist between the TE_{011} and TM_{111} modes, otherwise mode interference effects can drastically affect the Q of the cavity. Fortunately, although the frequencies of these two modes coincide, the field patterns are significantly different. These differences can be exploited to shift the resonant frequencies of the modes. The physical mechanism for this is due to the fact that the time-average electromagnetic energy stored in electric fields of the cavity must be equal to the energy stored in the magnetic fields. To illustrate, assume that we make a small perturbation to the volume of the cavity at a location where one of the fields, say electric field, is non-vashing but the other field (magnetic field) vanishes. Because the volume which the electric fields occupies changes, this perturbation will also change the energy stored by the electric fields. In order for the magnetic field energy to compensate for this change in electric field energy, a change in frequency must occur. In this sense the average energy stored by the electric fields remains equal to the average energy stored by the magnetic fields. The frequency shift when the cavity experiences a small volume perturbation can be approximated by [47]

$$\frac{\Delta\omega}{\omega} \approx \frac{\int_{\Delta V}(\mu H^2 - \epsilon E^2)dV}{\int_V(\mu H^2 + \epsilon E^2)dV} = \frac{\int_{\Delta V}(\mu H^2 - \epsilon E^2)dV}{4U_0}, \tag{4.91}$$

where U_0 is the total time-average energy stored in the cavity. Therefore, equation (4.91) can be used to calculate the shift in frequency for a given mode when the cavity undergoes a small volume perturbation. It is worthwhile noting the nature of the approximation taken in equation (4.91) so that a better understanding of when it is valid is obtained. The exact expression for the frequency shift in a cavity with a small volume perturbation is a function of the fields before the volume perturbation and the fields after the perturbation [49]. If the volume perturbation is made sufficiently small enough as to not significantly change the shape of the mode, then the approximation that the fields remain unperturbed can be made. In this way we can avoid having to calculate the perturbed fields, which can be cumbersome depending on the shape of the volume perturbation. Hence, the approximation in equation (4.91) holds in the limit that mode fields in the perturbed cavity remain relatively unchanged from the fields of the unperturbed cavity. Since the interaction of the fields depend on the geometry and location of the volume perturbation, a general limit cannot be defined. However, as a rule of thumb the approximation works good when the volume perturbations are made small.

4.6.1 Frequency shifts via Couplers

Let us apply equation (4.91) to our aluminum cylindrical cavity of radius (R) and length ($d \equiv L$) for the case of a small coupler located at r=.48R on the end-plate. The coupler is modeled by a very small cylindrical rod of radius a that is inserted an amount l at the point of maximum magnetic field for the TE_{011} mode ($r = 48\%R$) and at one end of the cavity, say ($z = 0$). Using the results for the TE fields of section 4.1.5 we can approximately evaluate equation (4.91) and estimate the shift in resonant frequency,

$$\frac{\Delta\omega}{\omega} \approx \frac{\mu_0 H_0^2 R^2 \Delta\phi}{4U_0} \left\{ \left[\int_{x_1}^{x_2} J_0^2(\lambda_{11}x)xdx - \left(\frac{\omega_{011}R}{cx_{11}}\right)^2 \int_{x_1}^{x_2} J_1^2(\lambda_{11}x)xdx \right] \left[\frac{l}{2} - \frac{L}{4\pi}\sin\left(\frac{2\pi}{L}l\right) \right] + \left[\left(\frac{\pi R}{Lx_{11}}\right)^2 \int_{x_1}^{x_2} J_1^2(\lambda_{11}x)xdx \right] \left[\frac{l}{2} + \frac{L}{4\pi}\sin\left(\frac{2\pi}{L}l\right) \right] \right\}, \tag{4.92}$$

where we define the Bessel zero $\lambda_{11} \equiv x_{11}$, $L \equiv d$, $x = r/R$, $x_1 = (.48R - a)/R$, $x_2 = (.48R + a)/R$,

$$\frac{H_0^2}{U_0} = \frac{2}{\mu_0 V_{\text{eff}}}, \text{ and } \Delta\phi \approx 2 \arctan\left(\frac{a}{0.48R}\right). \tag{4.93}$$

For our aluminum cavity $L = 2.695$ cm, $R = 1.905$ cm, $f = 11.1$ GHz, $\lambda_{11} = 3.8317$, and $a = 1.778$ mm, we find the frequency shift as a function of insertion length l for the TE_{011} is

$$\Delta f_{\text{TE011}} \approx 11.1\,[-0.199l + 1.78\sin(.233l)] \text{ [MHz]}. \tag{4.94}$$

where the insertion length (l) is in units of millimeters, and f_0 is the original resonant frequency of the cavity, 11.1 GHz in our case. A plot of the result is illustrated in figure 4.4. Using this method one can also design fine or coarse frequency tuners for RF cavities.

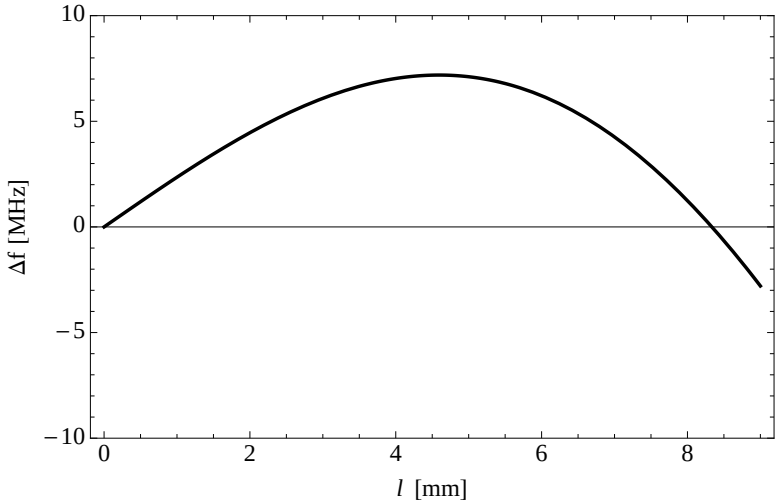

Figure 4.4: (Color)Approximation of the frequency shift in TE_{011} mode in a cylindrical cavity via an input coupler modeled as a 1.778 mm radius cylindrical rod placed at $r = 48\%R$, and $z = 0$ (i.e, at the point for maximum coupling to the TE_{011} mode). Frequency shift is plotted against the insertion length l of the coupler.

An experiment was preformed to test this idea, the results are illustrated in figure 4.5. The experiment consisted of a cylinder rod of radius $a = 1.778$ mm whose insertion length was varied with the used of a micrometer. Resonant frequencies were recorded with a network analyzer. For lengths less than 3 mm the approximation is fairly

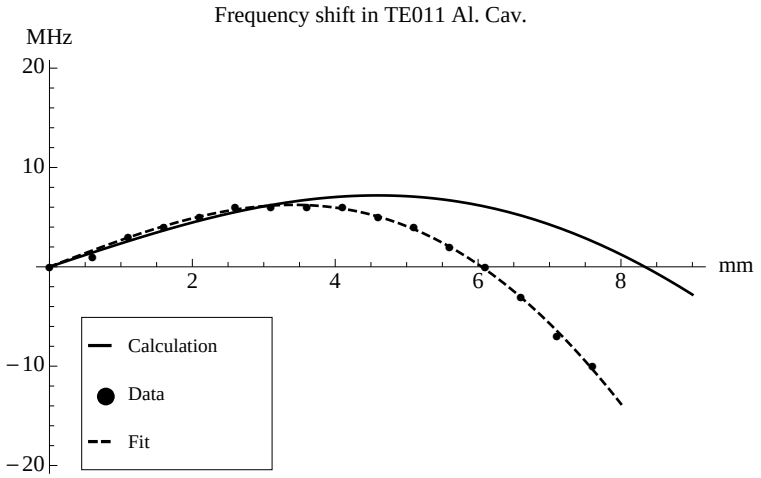

Figure 4.5: The solid curve is a plot of the approximation in equation (4.94), dashed curve is a fit to equation (4.95), and solid dots represent the data points obtained experimentally as the insertion length (l) of a 1.778 mm rod was varied in the cylindrical cavity.

good. The reason for the additional approximation during the evaluation of equation (4.91) was to avoid the difficulty in integrating the Bessel functions over an off-origin circular region in cylindrical coordinates. Instead, we approximated the circular region with a small wedge which is the natural area element in cylindrical coordinates. This approximation allows for easy solutions and it is illustrated in figure 4.6. To check the accuracy of functional dependance, we fit the data to

$$\Delta f = 11.1\,(\alpha l + \beta \sin(.233l))\ \ [\text{MHz}], \tag{4.95}$$

where α and β are left as fit parameters, and l is in mm. The fit shows that the functional dependance of the calculation is in excellent agreement with the experimental results. The correct values for the coefficients are found by the curve fit, $\alpha = -0.582979$ and $\beta = 3.57358$. These values provide the correct coefficients to the approximation in equation (4.94) which is shown in figure 4.5.

4.6.2 Frequency Shift due to a Protruded Ring

Although the coupler scheme appears to be a possible method to split the degeneracy that exist between the TE_{011} and TM_{111} modes, unwanted issues may arise. In particular, we have already observed that analytical calculations become cumbersome. More importantly the introduction of a coupler into the cavity adds additional losses which

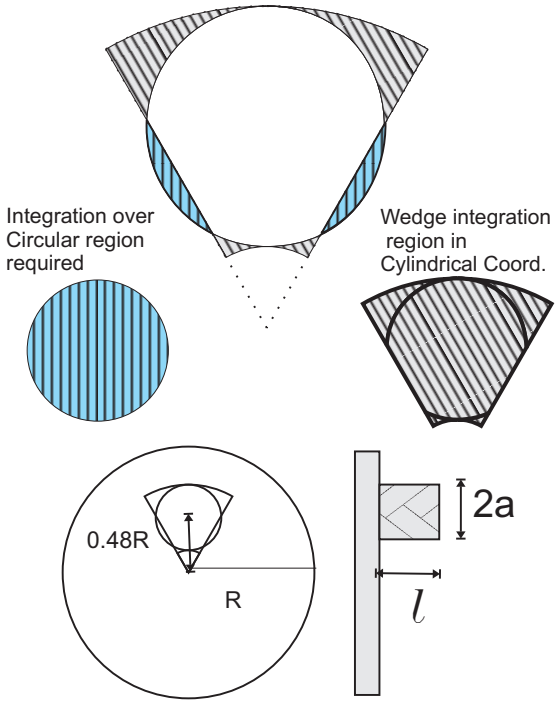

Figure 4.6: An illustration of the approximation taken to facilitate the evaluation of the Bessel integrals. In this form we avoid integrating the Bessel functions over an off-origin circular region in cylindrical coordinates. A schematic view of the small cylindrical rod is also shown, not to scale.

can have unwanted effects on the cavity's quality factor. Certainly, this is something thats needs to be avoided if high Q's are desired. For this reason we now analyze the case of a protruded ring located at one of the cavity's end-plates. A schematic view of the set up is shown in figure 4.7a, and a perspective view in figure 4.7b.

Using equation (4.91) from section 4.6 to estimate the frequency shift of the TE_{011} mode in our aluminum cylindrical cavity[4] for a ring with inner diameter (ID) of 0.75"=1.905 cm and outer diameter (OD) of 1.125"=2.858 cm we find the rather inaccurate result

$$\Delta f = 11.1(-6.31l + 46.76\sin[.233l])\ [\text{MHz}], \tag{4.96}$$

where l is the insertion length in units of millimeters. An experiment preformed to test this calculation showed that equation (4.96) is a very poor approximation of the actual

[4]R=1.905 cm, L=2.695 cm, and $f = 11.1$ GHz.

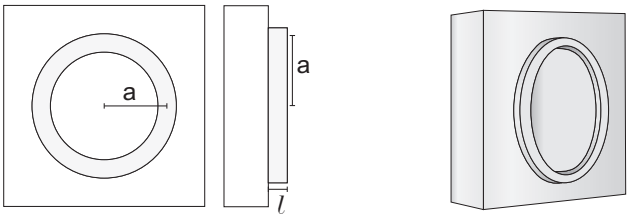

(a) Schematic view of protruded ring used as the volume perturbation.

(b) Perspective view of protruded ring on the cavity's end-plate.

Figure 4.7

frequency shift observed when a circular perturbation is introduced in the aluminum cavity. A plot of the inaccurate result in equation (4.96) is illustrated in figure **??**. A better approximation can be achieved by realizing that the inner diameter of the

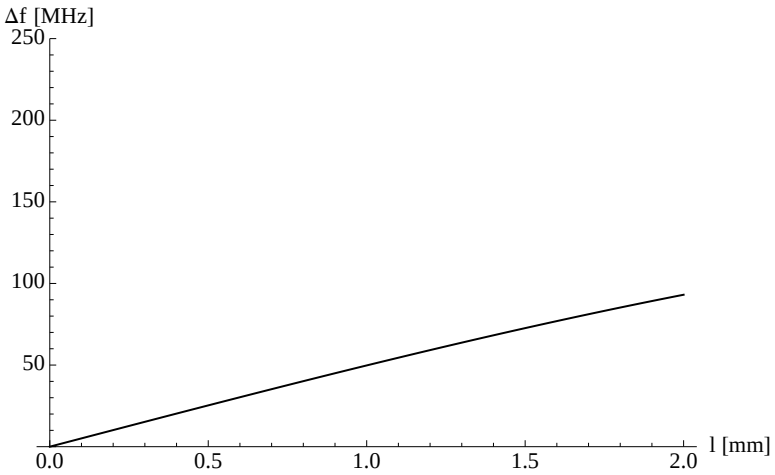

Figure 4.8: Plot of equation (4.96). The result is calculated with the actual dimensions of the ring perturbations (OD=1.905 cm, ID=2.585 cm) and is found to be a underestimate of the actual frequency shift observed experimentally.

ring perturbation acts like a circular waveguide that is below cutoff, hence, leading to evanescent waves inside the circular perturbation (see figure 4.7). In this approximation the circular perturbation in figure 4.7 is approximated as having an effective inner diameter of $ID_{eff} \equiv 0$, and the frequency shift is

$$\Delta f = 11.1(-2.79l + 46.81 \sin[.233l]) \text{ [MHz]}, \tag{4.97}$$

where l is the insertion length in millimeters. Figure 4.9 shows that the results in

equation (4.97) are in better agreement with the experimentally observed results. It is noted that measurement of the insertion length contributed to a portion of the error, and as can be observed from figure 4.9 the approximation breaks down after an insertion length of about 1.3 mm.

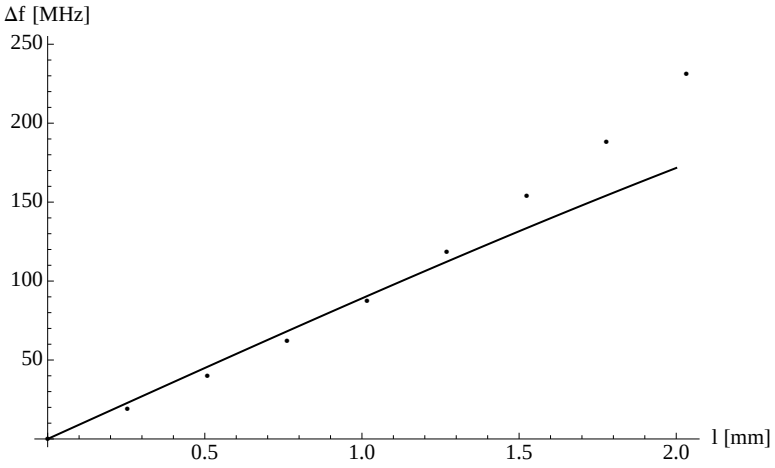

Figure 4.9: Assuming that evanescent waves within the circular perturbation leads to an effective ID=0, the calculation results in a much better estimate for the frequency shift in the TE_{011} mode of a cylindrical cavity with a ring perturbation. Solid curve is a plot of equation (4.97), dots represent experimental data points.

4.7 Q Measurements

The most important measurements for characterizing our cylindrical RF cavities are frequency, coupling parameters, and quality factor. It should be noted that in practice what is measured is the loaded quality factor (Q_L) which include extra losses introduced from the couplers. Nevertheless, the intrinsic quality factor can be extracted by a measurement of the coupling parameters.

Resonant frequency measurement is done with an HP electrical spectrum analyzer or with an HP network analyzer. Measurement of the cavity loaded Q value is achieved via the network analyzer which has 3 dB point measurements capabilities. Measurements are verified by fitting the data to the energy stored in the cavity [29]

$$U = \frac{\frac{2P_f}{\pi f}}{\left(\frac{1}{Q_L}\right)^2 + \left(\frac{x}{f} - \frac{f}{x}\right)^2}, \tag{4.98}$$

where U is the energy in the cavity, P_f is the forward traveling power, f is the resonant frequency determined by the fit, and Q_L is the loaded quality factor determined by the fit. Figure 4.10a shows equation (4.98) fitted to the measured data obtained from the aluminum cavity with the network analyzer. This analysis yields a loaded Q factor (Q_L) of approximately 14000 with a resonant frequency at 11.0692 GHz, consistent with network analyzer 3 dB point measurements. The cavity's intrinsic Q (Q_0) is calculated

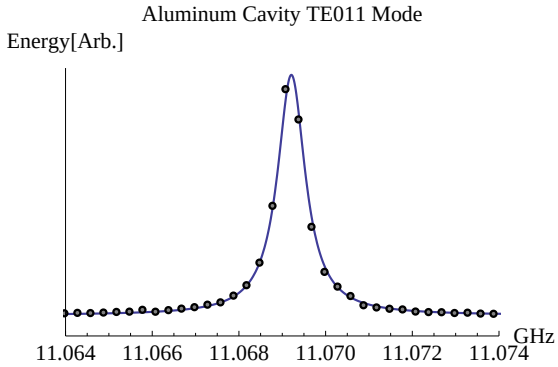

(a) Data obtained from network analyzer. Solid curve is a fit to equation (4.98), Q_L and f are determined by the fit.

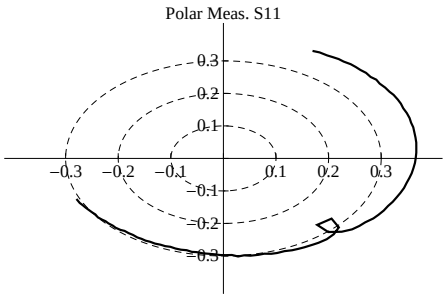

(b) Polar plot of the refection coefficient for a S11 measurement on the input coupler. It is determined that the cavity's input coupler is undercoupled.

Figure 4.10: Data

from

$$Q_0 = Q_L(1+\beta), \tag{4.99}$$

where β is the input coupling strength and can be determined by a reflection measurement via

$$\beta = \frac{1 \pm \sqrt{P_r/P_f}}{1 \mp \sqrt{P_r/P_f}}, \tag{4.100}$$

where the upper signs are used when the cavity input coupler is overcoupled, and the lower signs used when it is undercoupled. Determination of the state of coupling is done by a polar plot of the reflection coefficient as shown in figure 4.10b. The input coupling parameter is found to be $\beta = 0.55$. Combining this result with equation (4.99)

and the measured Q_L we find

$$Q_0 \sim 2.2 \times 10^4 \tag{4.101}$$

for our aluminum 6061 cylindrical cavity tuned to 11.0692 GHz. This is in good agreement with the predicted theoretical limit value of 3×10^4.

4.8 Copper RF Cylindrical Cavity Used for Membrane Excitation

Here we discuss the copper cavity used in an experiment in which a mechanical membrane was excited into motion via a TM_{010} RF mode in a cylindrical cavity. The details and results of this experiment are discussed in chapter 6. The resonant frequencies of the cylindrical copper cavity were determined from the following relation [46],

$$(fD)^2 = A + Bp^2 \left(\frac{D}{L}\right)^2, \tag{4.102}$$

where f is the frequency in MHz, D is the diameter of the cavity in centimeters, L is the length of the cavity in centimeters, p is the third index of the mode (i.e TM_{mnp} mode, where p corresponds to the number of half-wavelengths along the cylinder axis), A is constant depending on the mode, and B is a constant depending on the medium of the cavity; both constants are tabulated in [46]. For the TM_{010} mode ($p = 0$) it follows that the resonant frequency is independent of the length of the cavity, $(fD)^2 = A$. For the TM_{011} mode ($p = 1$) the resonant frequency becomes length dependent, $(fD)^2 = A + B(D/L)^2$. Measurement of the resonant frequencies were made with an HP 8720C Network Analyzer. Figure 4.11 shows a S21 transmission measurement of our copper cylindrical cavity with $D = 2.604$ cm and $L = 3.909$ cm. The two peaks represent the TM_{010} and TM_{011} modes.

Verification of the two modes of interest was achieved by varying the length of the cavity and recording the observed resonant frequencies. The measured resonant frequencies are plotted with the choice of $(D/L)^2$ and $(fD/10^4)^2$ as x and y coordinates, respectively. A linear fit to equation 4.102 is used to experimentally determined the constants A and B as a measure that the correct modes were excited. Figure 4.12 shows the fitted curves are in excellent agreement with the experimental results. The

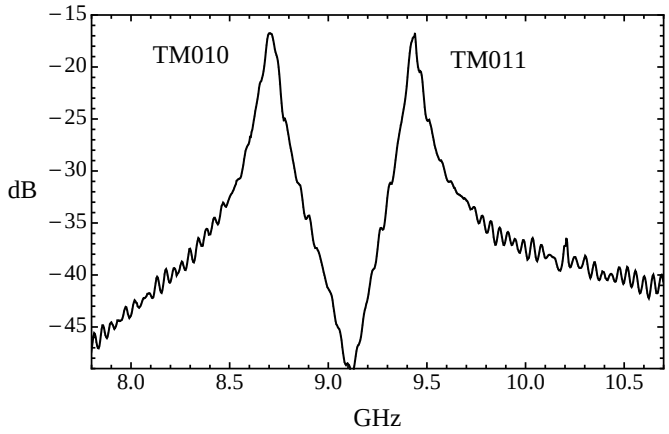

Figure 4.11: S21 measurement shows the resonant frequencies, 8.72 GHz and 9.41 GHz for the TM_{010} and TM_{011} modes, respectively, of the copper cylindrical cavity with $D = 2.604$ cm and $L = 3.909$ cm.

experimentally determined values ($A = 5.0830 \times 10^8$ and $B = 2.2109 \times 10^8$) were within 4% of the theoretical values reported in [46] ($A = 5.2621 \times 10^8$, and $B = 2.2451 \times 10^8$) this presents clear evidence that we successfully excited the TM_{010} and TM_{011} modes.

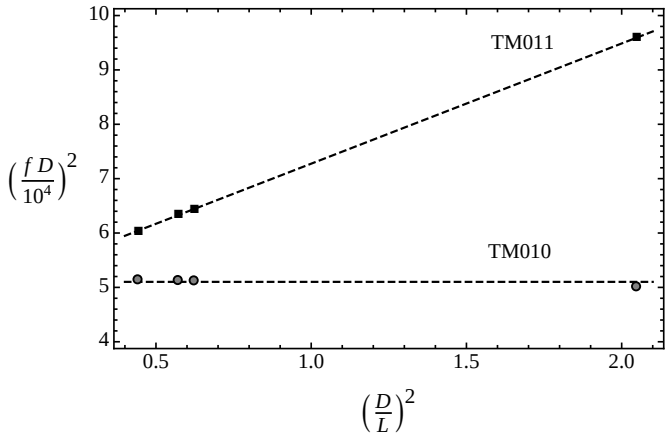

Figure 4.12: Measured resonant frequencies for various cavity lengths. A linear fit yields the experimentally determined values of A and B within 4% of the theoretical expected values. This is clear evidence the we excited the TM_{010} and TM_{011} modes.

The loaded quality factor ($Q_L = f_0/2\Delta f$) was determined experimentally by measuring the FWHM ($2\Delta f$) and resonant frequency. In addition, we verify the loaded Q

by fitting the measured power as a function of frequency [29]:

$$P_m = \frac{P_f}{(1/Q_{RF})^2 + (f/f_0 - f_0/f)^2}, \tag{4.103}$$

where P_f is used as a scaling fit parameter [5], Q_L is the loaded Q determined by the fit, and f_0 is the resonant frequency determined by the fit. Here Q_L serves as a lower limit on the RF cavity's intrinsic quality factor (Q_0). Figure 4.13 illustrates a fit of equation 4.103 to our experimental data for the copper cavity with a 50 nm gold coated membrane end-mirror. Data was obtained by sweeping an RF signal generator and measuring the output power with an RF spectrum analyzer. We found the loaded quality (Q_L) factor of the cavity to be on the order of 200.

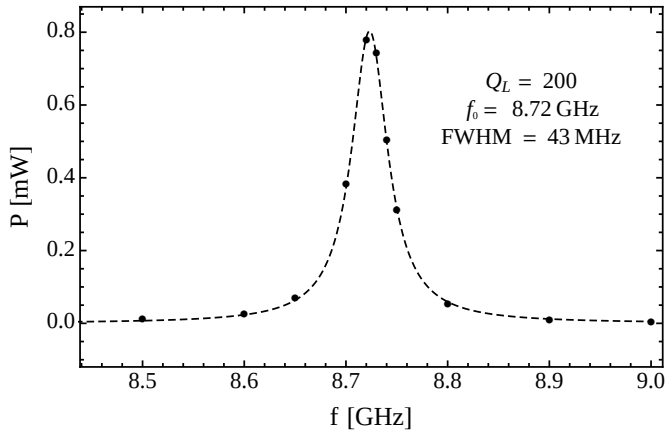

Figure 4.13: Fit of equation 4.103 to our experimentally measured power vs frequency for the TM_{010} mode. The fit accurately gives the resonant frequency (8.72 GHz) and loaded Q_L (200) of the copper cavity.

[5] Exact value of this depends on the input and output couplings, and forward power traveling towards the cavity

5

Vibration of Thin Elastic Circular Membranes

We begin with a concise description of elastic deformation in solids with the goal of introducing some of the concepts that will be important in the subsequent sections. Following we briefly examine the different types of waves (vibrations or modes of oscillation) that can exist within a circular isotropic elastic membrane and mention some of the different regimes in which these different modes can exist. Finally we solve the problem of a damped driven isotropic thin elastic circular membrane in detail.

5.1 Introduction to Elasticity in Solids

In general vibration in a solid must take into account all three spatial dimensions. Because a solid of finite thickness can undergo deformations in any spatial direction, modeling a true solid can be a complicated task. One must take into account all the possible combinations of deformations that the solid can undergo in three dimensions. The deformations of the solid when a stress is applied are referred to as normal and shear strains. Normal strains are elongations of the solid and typically denoted by $\epsilon_{xx},\ \epsilon_{yy},\ \epsilon_{zz}$. Shear strains refer to rotations of the solid's surfaces, or put differently, the total change of the solid's surface angle when a stress is applied with respect to the solid's original surface angle (usually 90 degrees). Shear strains are typically denoted by $\epsilon_{xy},\ \epsilon_{zx},\ \epsilon_{yz}$.

In the elastic limit (Hooke's law regime) a solid is assumed to return to its original

configuration after a deformation. In addition, the solid's deformations follow a Hooke's law behavior in which the strains are linearly proportional to the applied stress. The constants of proportionality are referred to as the elastic modulus (constants). Because of this Hooke's law behavior, we can write a given stress as a linear combination of all the strains the solid can undergo under a given load (stress), and where the constants of proportionality are defined by the elastic constants. In general for an anisotropic elastic material one can summarize all deformations via the stress tensor [50]

$$\sigma_{ij} = C_{ijkl}\epsilon_{kl}, \tag{5.1}$$

where C_{ijkl} is the elasticity tensor (note that it can also be expressed as a matrix $[C]$ whose components are the elasticity constants), and ϵ_{kl} denotes the shear and normal strain components. In matrix notation[1] this can be expressed as

$$[\sigma] = [C][\epsilon], \tag{5.2}$$

where $[\sigma]$ and $[\epsilon]$ are 6 component column matrices, and $[C]$ is a 6×6 matrix with 36 elastic constants. These relations are known as the *stress-strain relations* or the *constitutive relations*, and summarize the deformations of a 3-D elastic solid.

For an isotropic elastic material the elastic constants are independent of orientation and the elasticity matrix can be summarize by two independent elastic constants, λ and μ, known as *Lame's elastic constants*. The relation of Lame's constants with respect to the elasticity matrix are as follows [50]:

$$\begin{aligned} & C_{11} = C_{22} = C_{33} = \lambda + 2\mu \\ & C_{12} = C_{21} = C_{31} = C_{13} = C_{32} = C_{23} = \lambda \\ & C_{44} = C_{55} = C_{66} = \mu \\ \text{all other } & C_{ij} = 0. \end{aligned} \tag{5.3}$$

[1] We may also denote the components of the matrix $[C]$ as C_{ij}, the reader should be able to tell from the context.

Hence, for an isotropic elastic material equation (5.1) reduces to

$$\begin{aligned}
\sigma_{xx} &= \lambda\Delta + 2\mu\epsilon_{xx} \\
\sigma_{yy} &= \lambda\Delta + 2\mu\epsilon_{yy} \\
\sigma_{zz} &= \lambda\Delta + 2\mu\epsilon_{zz} \\
\sigma_{yz} &= \mu\epsilon_{yz} \\
\sigma_{zx} &= \mu\epsilon_{zx} \\
\sigma_{xy} &= \mu\epsilon_{xy},
\end{aligned} \tag{5.4}$$

where

$$\Delta \equiv \epsilon_{xx} + \epsilon_{yy} + \epsilon_{zz}, \tag{5.5}$$

and corresponds to the dilatation (compression or expansion) of the solid. Lame's constants (λ and μ) can be expressed in terms of Young's modulus E, shear modulus G, bulk modulus K, and Poisson's ratio ν as follows [50]

$$E = \frac{\mu(3\lambda + 2\mu)}{\lambda + \mu} \tag{5.6}$$

$$G = \mu \tag{5.7}$$

$$K = \lambda + \frac{2}{3}\mu \tag{5.8}$$

$$\nu = \frac{\lambda}{2(\lambda + \mu)} \tag{5.9}$$

or

$$\lambda = \frac{\nu E}{(1+\nu)(1-2\nu)} \tag{5.10}$$

$$\mu = \frac{E}{2(1+\nu)} = G \tag{5.11}$$

5.2 Modes of Vibration

The general equations of motion for a homogeneous, isotropic, elastic medium are compactly summarized by [50]

$$(\lambda + \mu)\nabla(\nabla \cdot \vec{u}) + \mu\nabla^2\vec{u} = \rho\vec{u}_{tt}, \tag{5.12}$$

where λ and μ are Lame's constants, and ρ is the mass density. These equations give rise to two main modes of vibrations. The first type of vibrations are those in which the dilatation vanishes ($\Delta = 0$). These particular modes may be identified by any of the following names: equivoluminal, flexural, drumhead, diaphragm, distortional, shear, transverse, rotational, or S-waves. The main mechanism behind these types of vibrations is the restriction that the dilatation, which represents the change in volume per unit volume of the material, vanishes. That is, the elastic solid cannot under go any volume changes. These types of modes are easily observed in thin flexible elastic membranes, as those present in a drumheads or diaphragms. For a thin membrane of radius R and volume mass density ρ stretched over an opening with tension T, the natural resonant frequencies are given by [50]

$$\omega_{mn} = \lambda_{mn}\frac{v}{R}, \tag{5.13}$$

where $v = \sqrt{T/\rho A}$ is the distortional speed of sound in the material, m represents the number of nodal diameters, n represents the number of nodal circles, and λ_{mn} is the n^{th} zero of the m^{th} order Bessel function. Because of the limiting mechanical properties of elastic solids, typically, the resonances of these modes are in the acoustic frequency range. These drumhead type modes are summarized in figure 5.1.

The second type of mode arises from compressional waves within the elastic medium. In this case, the dilatation does not vanish and changes in volume are allowed to occur. These types of waves lead to modes in which the solid's shape (volume) may change, unlike the drumhead modes where no change in volume was allowed. These waves or resulting modes may be referred to as: dilatational, irrotational, dilational, longitudinal, compression, or P-waves. The resonances for dilatational modes are dependent on the thickness of the elastic membrane. The fundamental dilatational resonance is given by [3]

$$\omega = v_s\frac{\pi}{t_0}, \tag{5.14}$$

where, $v_s = \sqrt{(\lambda + 2\mu)/\rho}$ is the speed of sound for compressional waves, and t_0 is the membrane's thickness. This result is rather intuitive and corresponds to the amount of time it takes a distortion to propagate back and forth through the elastic solid. Resonance occurs when the time between applied distortions coincide with the returning

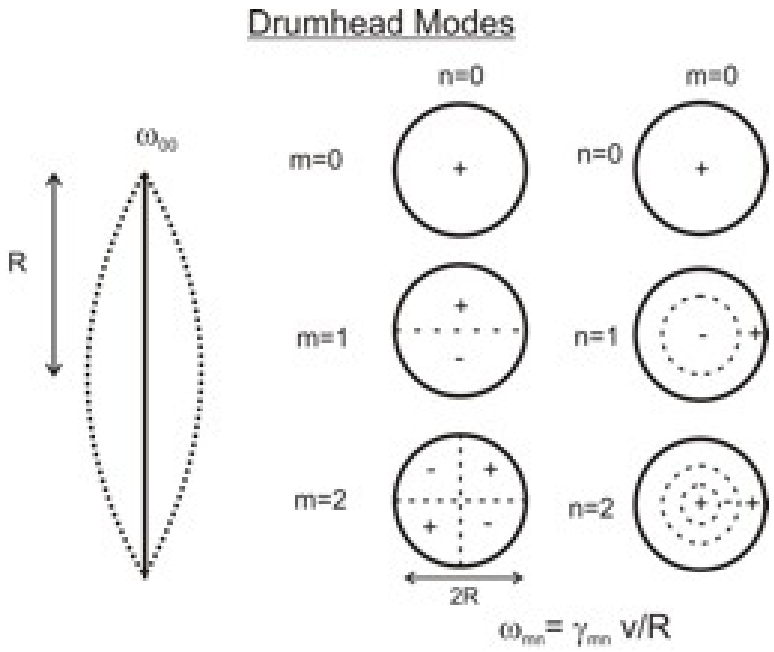

Figure 5.1: Front view of modal patterns and side view of the fundamental vibrational mode of a drumhead for a thin circular elastic membrane, where m represents the number of nodal diameters, n the number of nodal circles, and λ_{mn} in the n^{th} zero of the m^{th} order Bessel function.

signal. Typically, dilatational modes tend to have higher natural frequencies due to the higher speed of sounds associated within elastic solids and control over the thickness of the membrane. In modern day application extremely thin silicon nitride membranes down to a few tens of nanometers thick can be achieved. The fundamental dilatational mode is illustrated in figure 5.2

In general, both types of modes can be excited simultaneously. However, in practice when only drumhead modes are desired, it is important to restrict the elastic solid to a sufficiently thin flexible elastic membrane. In this limit the dilatational mode resonances are much higher in frequency, and can be ignored. A general relationship can be established between the speed of dilatational waves, and distortional waves. For a given isotropic linear elastic solid, the compressional wave speed v_s is greater than the distortional wave speed v, as can be seen from

$$\frac{v_s}{v} = \sqrt{2\frac{1-\nu}{1-2\nu}} > 1, \tag{5.15}$$

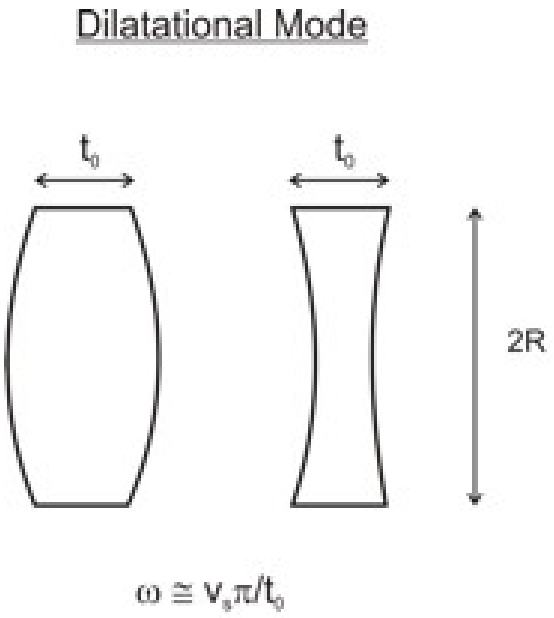

Figure 5.2: Excitation of the fundamental dilatational mode leads to longitudinal expansion and contraction of the elastic solid. Typically these modes tend to be higher in frequency.

where ν is Poisson's ratio for the elastic material and assumed to be less than 0.5.

5.3 Intermission: Bessel Series Expansion

We take a small digression to briefly discuss the Bessel-Fourier series expansion. For any function whose norm satisfies [51, 52]

$$||f(x)||^2 \equiv \int_0^1 f(x)^2 x dx < +\infty \tag{5.16}$$

where here x is a dimensionless variable, the function can be expanded in a Bessel-Fourier series as

$$f(x) = \sum_{n=1}^{\infty} c_n J_\nu(\lambda_n x) \tag{5.17}$$

where λ_n is the n^{th} Bessel zero[2] of J_ν. The coefficients c_n follow from the following orthogonality condition

$$\int_0^1 J_\nu(\lambda_m x) J_\nu(\lambda_n x) x dx \equiv < J_\nu(\lambda_m x), J_\nu(\lambda_n x) >= 0 \text{ if } m \neq n \tag{5.18}$$

Hence, the coefficients of the Bessel series are given by

$$c_n = \frac{< f(x), J_\nu(\lambda_n x) >}{||J_\nu(\lambda_n x)||^2}, \tag{5.19}$$

where

$$||J_\nu(\lambda_n x)||^2 = \frac{J_{\nu-1}^2(\lambda_n)}{2}. \tag{5.20}$$

5.4 Damped Driven Thin Elastic Circular Membrane

The displacement (u) for the damped-driven elastic membrane is given by the following equation of motion [53]

$$\rho \ddot{u} + \gamma \dot{u} - \mathcal{T} \nabla^2 u = e^{i\Omega t} F(r), \tag{5.21}$$

where ρ is the mass per unit area, r is the radial coordinate, $\gamma \equiv 2\rho\beta$ is the damping coefficient, $\mathcal{T}$ is the tension per unit length, Ω is the modulation frequency, and $F(r)$ is a radially symmetric driving pressure that can be expanded as a zeroth-order Bessel series. The particular solution to equation 5.21 is obtained via a Bessel-Series solution method with the following Anzatz [3]

$$u(r,t) = e^{i\Omega t} \sum_{n=1}^{\infty} A_n J_0 \left(\lambda_n \frac{r}{R} \right), \tag{5.22}$$

where J_0 is the zeroth-order Bessel function, λ_n is the n^{th} zero of the zeroth-order Bessel function, and R is the radius of the membrane

Upon substitution of equation (5.22) in equation (5.21), and writing $f(r) = F(r)/\rho$ as a zeroth-order Bessel series, we find

$$\sum_n A_n [-\Omega^2 J_0(\lambda_n \frac{r}{R}) + 2\beta i \Omega J_0(\lambda_n \frac{r}{R}) - v^2 \nabla^2 J_0(\lambda_n \frac{r}{R})] = \sum_{n'} c_{n'} J_0(\lambda_{n'} \frac{r}{R}), \tag{5.23}$$

[2] Note that we will omit double referencing in the form of $\lambda_{\nu n}$, the index ν is unnecessary.
[3] Clamped boundary conditions, $u(r = R, \theta) = 0$

where $v^2 \equiv \mathcal{T}/\rho$, $2\beta \equiv \gamma/\rho$, and $f(r) \equiv F(r)/\rho$. Multiplying by $rJ_0(\lambda_n \frac{r}{R})$ on both sides then integrating over the radius of the membrane we find,

$$A_n \left[(2\beta i\Omega - \Omega^2) \int_0^R rJ_0(\lambda_n \frac{r}{R})^2 dr - v^2 \int_0^R rJ_0(\lambda_n \frac{r}{R}) \nabla^2 J_0(\lambda_n \frac{r}{R}) dr \right] = c_{n'} \int_0^R rJ_0(\lambda_{n'} \frac{r}{R}) J_0(\lambda_n \frac{r}{R}) dr. \tag{5.24}$$

To obtain non-vanishing coefficients (i.e $A_n \neq 0$) it is required that

$$\lambda_n = \lambda_{n'}, \tag{5.25}$$

and after the expansion of the second derivative term, equation (5.24) becomes

$$A_n \left\{ (2\beta i\Omega - \Omega^2) \int_0^R rJ_0(\lambda_n \frac{r}{R})^2 dr - v^2 \int_0^R \left[-\frac{\lambda_n^2}{2R^2} \left(rJ_0^2(\lambda_n \frac{r}{R}) - rJ_0(\lambda_n \frac{r}{R}) J_2(\lambda_n \frac{r}{R}) \right) - \frac{\lambda_n}{R} J_0(\lambda_n \frac{r}{R}) J_1(\lambda_n \frac{r}{R}) \right] dr \right\} = c_n \int_0^R rJ_0^2(\lambda_n \frac{r}{R}) dr. \tag{5.26}$$

To calculate the first coefficient A_1, set $r = xR$ in order to use the orthonormal properties of the Bessel functions,

$$A_1 \left\{ (2\beta i\Omega - \Omega^2) R^2 \int_0^1 xJ_0(\lambda_1 x)^2 dx + v^2 \left[\frac{\lambda_1^2}{2} \int_0^1 J_0^2(\lambda_1 x) x dx - \frac{\lambda_1^2}{2} \int_0^1 J_0(\lambda_1 x) J_2(\lambda_1 x) x dx + \lambda_1 \int_0^1 J_0(\lambda_1 x) J_1(\lambda_1 x) x dx \right] \right\} = c_1 R^2 \int_0^1 J_0^2(\lambda_1 x) x dx. \tag{5.27}$$

With

$$\int_0^1 J_0^2(\lambda_1 x) x dx = ||J_0(\lambda_1 x)||^2 = \frac{1}{2} J_1^2(\lambda_1) \tag{5.28}$$

equation (5.27) becomes

$$A_1\left\{(2\beta i\Omega-\Omega^2)R^2\left(\frac{1}{2}J_1^2(\lambda_1)\right)+\right.$$
$$\left.v^2\left[\frac{\lambda_1^2}{2}\left(\frac{1}{2}J_1^2(\lambda_1)\right)-\frac{\lambda_1^2}{2}\int_0^1 J_0(\lambda_1 x)J_2(\lambda_1 x)xdx+\lambda_1\int_0^1 J_0(\lambda_1 x)J_1(\lambda_1 x)xdx\right]\right\}$$
$$=c_1R^2\left(\frac{1}{2}J_1^2(\lambda_1)\right). \tag{5.29}$$

The last integral on the second line is

$$\int_0^1 J_0(\lambda_1 x)J_1(\lambda_1 x)xdx=\frac{1}{2\lambda_1}, \tag{5.30}$$

and with some algebraic simplification

$$A_1\left\{(2i\beta\Omega-\Omega^2)+\frac{v^2\lambda_1^2}{R^2}\left[\frac{1}{2}+\frac{1}{\lambda_1^2J_1^2(\lambda_1)}-\frac{\xi_1}{J_1^2(\lambda_1)}\right]\right\}=c_1, \tag{5.31}$$

where

$$\xi_1\equiv\int_0^1 xJ_0(\lambda_1 x)J_2(\lambda_1 x)dx. \tag{5.32}$$

The last term in brackets in equation (5.31) is computed numerically and is identically 1;

$$\left[\frac{1}{2}+\frac{1}{\lambda_1^2J_1^2(\lambda_1)}-\frac{\xi_1}{J_1^2(\lambda_1)}\right]=1. \tag{5.33}$$

Noting that the *free*[4] membrane's resonant frequency is given by

$$\omega_1=\frac{\lambda_1 v}{R} \tag{5.34}$$

we set

$$\frac{v^2\lambda_1^2}{R^2}=\omega_1^2, \tag{5.35}$$

where ω_1 is introduced and denotes the natural resonant frequency of a *free* membrane

[4]Undriven-undamped membrane.

(pellicle). Finally, the expression for A_1 is

$$A_1 = \frac{c_1}{\left[(\omega_1^2 - \Omega^2) + 2i\beta\Omega\right]}. \tag{5.36}$$

In a similar fashion we can solve for the n^{th} coefficient,

$$A_n = \frac{c_n}{[(\mu_n\omega_n^2 - \Omega^2) + 2i\beta\Omega]}, \tag{5.37}$$

where

$$\mu_n \equiv \left[\frac{1}{2} + \frac{2\Lambda_n}{\lambda_n J_1^2(\lambda_n)} - \frac{\xi_n}{J_1^2(\lambda_n)}\right]. \tag{5.38}$$

The full particular steady state solution (ignoring transients) can now be summarized as

$$u(r,t) = e^{i\Omega t + i\delta}\sum_{n=1}^{\infty} A_n J_0(\lambda_n \frac{r}{R}), \text{ where} \tag{5.39}$$

$$A_n = \frac{c_n}{\sqrt{(\mu_n\omega_n^2 - \Omega^2)^2 + 4\beta^2\Omega^2}}, \tag{5.40}$$

$$\mu_n \equiv \left[\frac{1}{2} + \frac{2\Lambda_n}{\lambda_n J_1^2(\lambda_n)} - \frac{\xi_n}{J_1^2(\lambda_n)}\right], \tag{5.41}$$

$$\Lambda_n \equiv \int_0^1 J_0(\lambda_n x) J_1(\lambda_n x) dx, \tag{5.42}$$

$$\xi_n \equiv \int_0^1 x J_0(\lambda_n x) J_2(\lambda_n x) dx, \text{ and} \tag{5.43}$$

$$c_n = \frac{< f(r), J_\nu(\lambda_n x) >}{||J_\nu(\lambda_n x)||^2}, \tag{5.44}$$

where the added phase accounts for the complex amplitude A_n, $x = r/R$ is a dimensionless variable, and $f(r)$ is a radially symmetric function that is expanded as a Bessel series and corresponds to the driving pressure divided by the density ρ. It's important to note that the term μ_n appears to be unity at least to order $n = 20$ as checked with a numerical calculation. The recipe for the above solution is to first take a radially symmetric function $f(r)$, expand it as a Bessel series that results in the fastest conversion, calculate the coefficients c_n along with the other given quantities, and keeping in mind that $\mu_n = 1$ for $n \leq 20$, then calculate the amplitude of oscillation A_n.

The result in equations (5.39)-(5.44) will be used in the following chapter in appli-

cation with RF cylindrical cavities where the Maxwell stress tensor creates a driving pressure on a elastic circular membrane attached to one end of the RF cylindrical cavity.

6

Excitation of Thin Circular Membranes with RF Cylindrical Cavities

This chapter begins with with the use of the general results from chapter 5 to obtain an order of magnitude estimate for the amplitude of vibration of a thin circular membrane excited at its acoustic resonances by a TM_{010} and a TE_{011} electromagnetic mode in a RF cylindrical cavity. Following, we estimate the vibrational mode amplitude in the high frequency regime, in which the mechanical membrane's oscillation frequency approaches the free mass limit. Finally, present experimental results are presented, and are in excellent agreement with the calculations for the coupling of the mechanical mode to the electromagnetic TM_{010} mode.

6.1 Calculations

6.1.1 Excitation of a circular membrane via a TM_{010} mode

Consider a RF cylindrical cavity of radius R with an elastic membrane placed at one end. Due to the electromagnetic fields contained within the cavity there will be a pressure exerted on the walls of the cavity. The pressure at a particular boundary is generally given by the Maxwell stress tensor [54]

$$T_{ij} = \epsilon_0 \left(\mathcal{E}_i \mathcal{E}_j - \frac{1}{2} \delta_{ij} \mathcal{E}^2 \right) + \frac{1}{\mu_0} \left(\mathcal{B}_i \mathcal{B}_j - \frac{1}{2} \delta_{ij} \mathcal{B}^2 \right), \tag{6.1}$$

where $\mathcal{E}$ and $\mathcal{B}$ are the radially symmetric electromagnetic (EM) fields of the TM_{010} mode[1] in the RF cylindrical cavity. The TM_{010} fields are calculated from equation (4.42) in section 4.1.5,

$$\mathcal{E}_z = \mathcal{E}_0 J_0(k_1 r) e^{-i\omega t} \tag{6.2}$$

$$\mathcal{H}_\phi = -\frac{i\mathcal{E}_0}{\eta} J_1(k_1 r) e^{-i\omega t}, \tag{6.3}$$

where $k_n \equiv \lambda_n / R$, $\eta = \sqrt{\mu_0/\epsilon_0}$ is the impedance of free space, and $\mathcal{E}_0$ is the peak electric field inside the cavity. The force per unit area along the normal direction on the membrane is computed from the Maxwell stress tensor and the EM fields,

$$T_{zz} = \frac{\epsilon_0 \mathcal{E}_0^2}{2} \left[J_0^2(k_1 r) + J_1^2(k_1 r) \right] e^{-i\omega t}. \tag{6.4}$$

Keep in mind that we have only calculated the z-component at the membrane because we are interested in the force pushing the elastic membrane in a direction normal to its surface. In this manner the T_{zz} component excites transverse drumhead modes due the applied stress of the EM fields. Observe that equation (6.4) is a radially symmetric pressure compose of a linear combination of two Bessel functions. Hence, we can use the results from chapter 5 to calculate the coefficients c_n. We begin by defining equation (6.4) as the radially symmetric function $f(r)$ so that it can be expanded as a Bessel series

$$F(r) \equiv \frac{\epsilon_0 \mathcal{E}_0^2}{2} \left[J_0^2 \left(\lambda_1 \frac{r}{R} \right) + J_1^2 \left(\lambda_1 \frac{r}{R} \right) \right] e^{-i\omega t}. \tag{6.5}$$

The natural resonance of the mechanical membrane will have a relatively low resonant frequency as compared to the resonant frequency of the RF cavity ($f_{\text{EM}} >> f_{\text{mech}}$). Thus, we preform a time average of the fast oscillating RF fields, and define a low acoustic-range modulation frequency Ω which drives the membrane at resonance. Experimentally this is achieved by the amplitude modulation of the RF power in cavity. The time average adds a factor of 1/2 and removes the time dependance so that

$$f(r) \equiv \frac{< F(r) >}{\rho} = \frac{1}{2} \frac{\epsilon_0 \mathcal{E}_0^2}{2\rho} \left[J_0^2 \left(\lambda_1 \frac{r}{R} \right) + J_1^2 \left(\lambda_1 \frac{r}{R} \right) \right], \tag{6.6}$$

[1] We have slightly switched notation of the fields from $E \rightarrow \mathcal{E}$ etc. However, we may use them interchangeably.

where we also divided by the area mass density of the membrane. The radial symmetric function $f(r)$ is now expanded as a Bessel series of zeroth order Bessel functions. Ignoring the constants momentarily, lets begin with the expansion of the $J_0^2(\lambda_1 \frac{r}{R})$ term. Let

$$J_0^2(\lambda_1 \frac{r}{R}) = \sum_{n=1}^{\infty} a_n J_0(\lambda_1 \frac{r}{R}) \tag{6.7}$$

multiplying by $rJ_0(\lambda_1 \frac{r}{R})$ the first coefficient a_1 is

$$a_1 = \frac{\int_0^R r J_0^3(\lambda_1 \frac{r}{R}) dr}{||J_0(\lambda_1 \frac{r}{R})||^2}. \tag{6.8}$$

Similarly the nth coefficient a_n is

$$a_n = \frac{2\int_0^1 x J_0^2(\lambda_1 x) J_0(\lambda_n x) dx}{J_1^2(\lambda_n)}, \tag{6.9}$$

where $r \equiv Rx$, and the orthonormality condition for the Bessel functions was used. The expansion for the $J_1^2(\lambda_1 \frac{r}{R})$ term is analogous, we find

$$J_1^2(\lambda_1 \frac{r}{R}) = \sum_{n=1}^{\infty} b_n J_0(\lambda_n \frac{r}{R}), \text{ where,} \tag{6.10}$$

$$b_n = \frac{2\int_0^1 x J_1^2(\lambda_1 x) J_0(\lambda_n x) dx}{J_1^2(\lambda_n)}. \tag{6.11}$$

The first 10 values of the coefficients of a_n, and b_n are listed in figure 6.1. Therefore, c_n can be expressed in terms of the above results for a_n and b_n,

$$c_n = \frac{\epsilon_0 \mathcal{A} \mathcal{E}_0^2}{4m}(a_n + b_n), \tag{6.12}$$

where we have assumed a uniform area mass density of the membrane $\rho = m/\mathcal{A}$.It now follows that the particular solution for the membrane's displacement when driven with

a_n	$\frac{<J_0(\lambda_n r), J_0{}^2(\lambda_1 r)>}{\|J_0(\lambda_n r)\|^2}$
a_1	0.7230
a_2	0.3120
a_3	−0.0477
a_4	0.0190
a_5	−0.0099
a_6	0.0060
a_7	−0.0039
a_8	0.0028
a_9	−0.0020
a_{10}	0.0015

(a)

b_n	$\frac{<J_0(\lambda_n r), J_1{}^2(\lambda_1 r)>}{\|J_0(\lambda_n r)\|^2}$
b_1	0.3620
b_2	−0.5100
b_3	0.2610
b_4	−0.2090
b_5	0.1810
b_6	−0.1630
b_7	0.1490
b_8	−0.1390
b_9	0.1300
b_{10}	−0.1230

(b)

Figure 6.1: First 10 tabulated values for the coefficients a_n, and b_n.

a TM_{010} mode is

$$u(r,t) = e^{i\Omega t + i\delta} \sum_{n=1}^{\infty} A_n J_0(\lambda_n \frac{r}{R}), \text{ with} \tag{6.13}$$

$$A_n = \frac{c_n}{\sqrt{(\mu_n \omega_{0n}^2 - \Omega^2)^2 + 4\beta^2\Omega^2}}, \tag{6.14}$$

$$\mu_n \equiv \left[\frac{1}{2} + \frac{2\Lambda_n}{\lambda_n J_1^2(\lambda_n)} - \frac{\xi_n}{J_1^2(\lambda_n)}\right], \tag{6.15}$$

$$\Lambda_n \equiv \int_0^1 J_0(\lambda_n x) J_1(\lambda_n x) dx, \tag{6.16}$$

$$\xi_n \equiv \int_0^1 x J_0(\lambda_n x) J_2(\lambda_n x) dx, \text{ and} \tag{6.17}$$

$$c_n = \frac{\epsilon_0 \mathcal{A} \mathcal{E}_0^2}{4m}(a_n + b_n), \tag{6.18}$$

$$a_n = \frac{2\int_0^1 x J_0^2(\lambda_1 x) J_0(\lambda_n x) dx}{J_1^2(\lambda_n)}, \tag{6.19}$$

$$b_n = \frac{2\int_0^1 x J_1^2(\lambda_1 x) J_0(\lambda_n x) dx}{J_1^2(\lambda_n)}, : \tag{6.20}$$

where $\mathcal{A}$ is the area of the membrane, m is the mass, ω_{0n} are the natural radially symmetric acoustic resonances of the elastic membrane, δ is a phase, ϵ_0 is the permittivity

of free space, 2β is the FWHM, $\mathcal{E}_0$ is the peak electric field inside the cavity, and it is noted that $\mu_n = 1$ for the first 20 terms; higher order terms were not checked.

6.1.2 Excitation of a circular membrane via a TE_{011} mode

Excitation of a thin mechanical membrane via a TE_{011} in a cylindrical RF cavity is calculated in the same manner. However, the electromagnetic fields for this particular mode differ. At the boundary where the membrane is located only the magnetic field along the radial direction in non-zero. This radial component of the magnetic field is given by (see section 4.1.5)

$$H_\rho = -\mathcal{H}_0 J_0'(\lambda_{01}' \frac{r}{R}) e^{-i\omega t}, \quad \mathcal{H}_0 \equiv H_0 \frac{\pi R}{d\lambda_{01}'} \tag{6.21}$$

where H_0 is the peak magnetic field inside the cavity, R is the radius, λ_{01}' is the first zero of J_0' (i.e. $J_0'(\lambda_{01}') = -J_1(\lambda_{01}') = 0$), and d is the length of the cavity. A plot of the relevant fields for the TE_{011} are shown in figure 6.2.

As for the TM_{010} mode, the z-component of the Maxwell stress tensor creates a pressure along the z-direction which excites into motion a mechanical membrane placed at one end. The $\hat{x}$ and $\hat{y}$ field components lead to strains along the radial direction, however, these can be neglected. Thus, from equation (6.1) the pressure exerted on the membrane along the z-direction is

$$T_{zz} = -\frac{\mu_0 \mathcal{H}_0^2}{2} J_1^2(\lambda_{01}' \frac{r}{R}) e^{-2i\omega t} \tag{6.22}$$

where μ_0 is the permeability of free space, and $\mathcal{H}_0$ is defined in equation (6.21). Observe that the Maxwell stress tensor pressure in equation (6.22) is a radially symmetric function. Hence, the solution of the damped-driven membrane is identical as in the previous section, with the exception that we have a different Bessel series $f(r)$ for the driving term,

$$f(r) \equiv \frac{T_{zz}}{\rho} = -\frac{\mu_0 \mathcal{H}_0^2}{2\rho} J_1^2(\lambda_{01}' \frac{r}{R}) e^{-2i\omega t}. \tag{6.23}$$

The expansion of the term (ignoring the constants momentarily) $J_1^2(\lambda_{01}' \frac{r}{R})$ in terms of

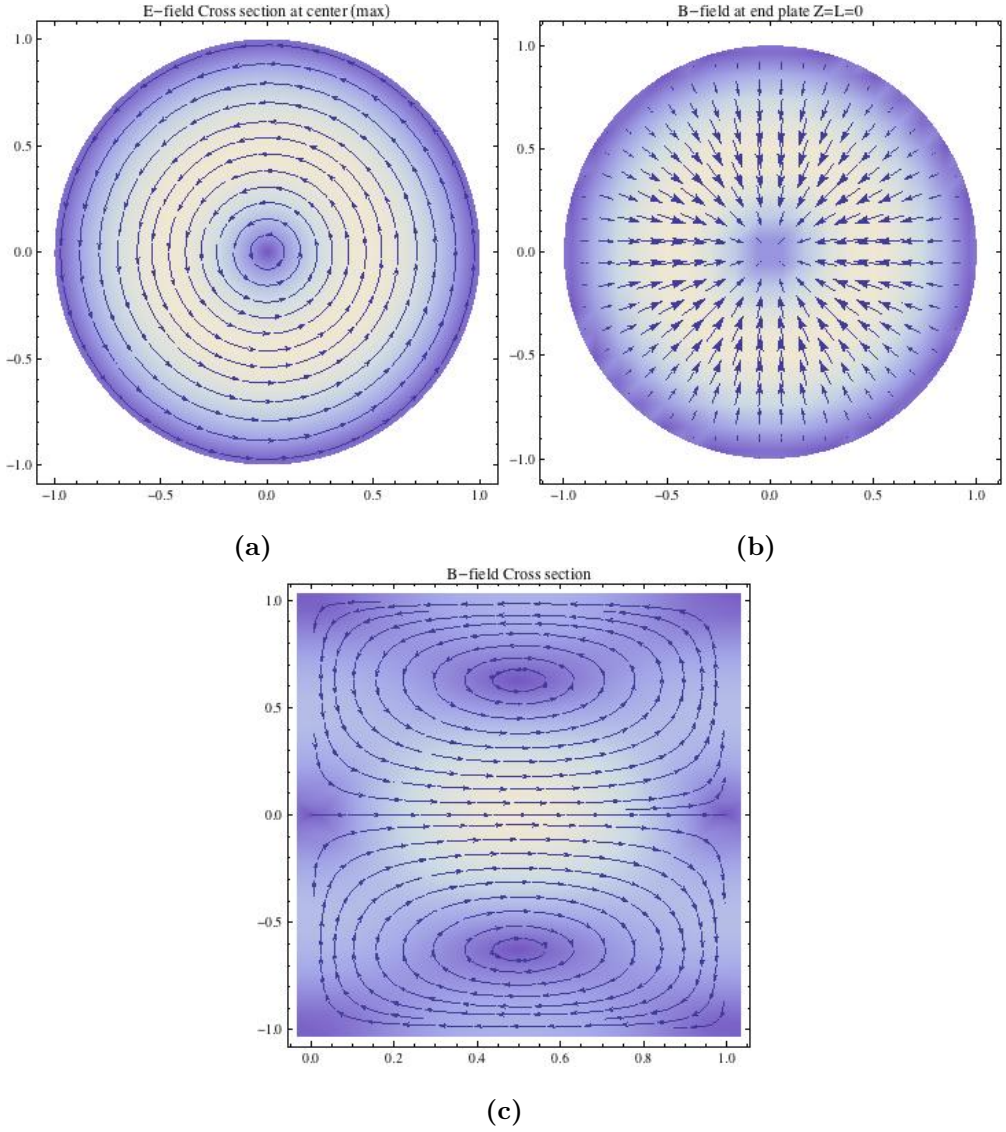

Figure 6.2: Plot of the TE_{011} electric and magnetic fields. Light regions represent high field amplitude. Dark shading represent regions of zero field. The electric field is maximum at the center of the cavity and zero at the ends.

the zeroth-order Bessel functions gives

$$J_1^2(\lambda_{11}x) \propto \sum_{n=1}^{\infty} c_n J_0(\lambda_{0n}\frac{r}{R}), \tag{6.24}$$

where $x \equiv r/R$, and $\lambda_{11} \equiv \lambda'_{01}$ is the first Bessel zero of the first order Bessel function

J_1. Solving for the coefficient c_n we find

$$c_n \propto \frac{2\int_0^1 J_1^2(\lambda_{11}x)xJ_0(\lambda_{0n}x)}{J_1^2(\lambda_{0n})}dx. \tag{6.25}$$

Note that besides the numerical constant this result for c_n is identical to b_n in the previous result for the TM_{010} mode, hence, the first 10 coefficients can be read off from figure 6.1b. The particular solution for the damped-driven circular membrane's displacement when driven with a TE_{011} mode is

$$u(r,t) = e^{2i\omega t+i\delta}\sum_{n=1}^{\infty} A_n J_0(\lambda_n \frac{r}{R}), \text{ with} \tag{6.26}$$

$$A_n = \frac{c_n}{\sqrt{(\omega_{0n}^2-\Omega^2)^2+4\beta^2\Omega^2}}, \tag{6.27}$$

$$c_n = \frac{\mu_0\mathcal{H}_0^2}{2\rho}\frac{2\int_0^1 J_1^2(\lambda_{11}x)xJ_0(\lambda_{0n}x)}{J_1^2(\lambda_{0n})}dx. \tag{6.28}$$

where ρ is the area mass density of the membrane which has been assumed to be uniform, ω_{0n} are the natural resonances of the membrane, δ a phase factor associated with the complex amplitude, μ_0 is the permeability of free space, 2β is the FWHM, $\mathcal{H}_0$ is defined in equation (6.21), and have $\mu_n = 1$ for the first 20 terms, hence, not listed here (see equations (6.13)-(6.20)).

6.1.3 Calculation of peak field H_0 for the TE_{011} mode

The peak magnetic field H_0 is calculated in terms of forward traveling power P_f, intrinsic quality factor Q_0, coupling parameter β, and resonant frequency ω_0. The energy stored in steady state within a RF cavity driven at resonance, and with a single input coupler, is given by [29]

$$U_0 = \frac{4\beta P_f}{(1+\beta)^2}\frac{Q_0}{\omega_0}. \tag{6.29}$$

In practice an output coupler may be used to sample a small amount of energy from the cavity. Typically this coupling is very small, and to a good approximation we can use the above result so long the output coupler does not allow for large energy loss.

The total electromagnetic energy in the cavity is

$$U_0 = \frac{1}{2}\mu_0 \int_V |\vec{H}|^2 dV = \frac{1}{2}\epsilon \int_V |\vec{E}|^2 dV, \tag{6.30}$$

where the integral is over the volume of the cavity. From equations (6.30) and (6.29), we can express H_0 in terms of parameters that are easily measurable in practice. It is convenient to use the magnetic fields in equation (6.30) so that

$$\int_V |\vec{H}|^2 dV = \int_V (H_\rho^2 + H_z^2) dV. \tag{6.31}$$

The solution to the first integral involving H_ρ is

$$\begin{aligned}\int_V H_\rho^2 dV &= R^2 \mathcal{H}_0^2 \int_0^d \cos^2(\frac{\pi z}{d}) dz \int_0^{2\pi} d\phi \int_0^1 x J_1^2(\lambda_{11} x) dx \\ &= \mathcal{H}_0^2 \frac{\pi R^2 d}{2} J_0^2(\lambda_{11}),\end{aligned} \tag{6.32}$$

where $x \equiv r/R$, and $\lambda_{11} = \lambda'_{01}$.With $H_z = H_0 \sin(\pi z/d) J_0(\lambda'_{01} r/R)$, the second integral involving H_z is

$$\begin{aligned}\int_V H_z^2 dV &= H_0^2 \int_0^d \sin^2(\frac{\pi z}{d}) dz \int_0^{2\pi} d\phi \int_0^1 x J_0^2(\lambda_{11} x) dx \\ &= H_0 \frac{\pi R^2 d}{2} J_0^2(\lambda_{11}),\end{aligned} \tag{6.33}$$

Combining both results, the stored energy in the cavity is

$$\frac{2U_0}{\mu_0} = \frac{\pi R^2 d}{2} J_0^2(\lambda_{11})[\mathcal{H}_0^2 + H_0^2]. \tag{6.34}$$

Plugging in the definition for $\mathcal{H}_0 \equiv H_0 \pi R/d\lambda_{11}$

$$\frac{2U_0}{\mu_0} = H_0^2 \times \frac{\pi R^2 d}{2} J_0^2(\lambda_{11}) \left(\left(\frac{\pi R}{\lambda_{11} d} \right)^2 + 1 \right) \equiv H_0^2 \times V_{\text{eff}}. \tag{6.35}$$

Observe that the main effect of the integration is to account for the volume where the fields are non zero. It is instructive to calculate the ratio of the exact energy (U_0) due to the mode versus the approximated energy (U_{approx}) if one did not integrate and

instead used the approximation $V_{\text{eff}} \approx \pi R^2 d$, the actual volume of the cavity,

$$\frac{U_0}{U_{\text{approx}}} = \frac{V_{\text{eff}}}{V_{\text{cav}}} = \frac{1}{2} J_0^2(\lambda_{11}) \left(\left(\frac{\pi R}{\lambda_{11} d} \right)^2 + 1 \right), \tag{6.36}$$

where $U_{\text{approx}} \propto H_0^2 V_{\text{cav}}$ denotes the approximated energy when one uses the actual volume of the cavity instead of the effective volume. For our aluminum cavity of $R = 1.5" = 3.81$ cm and $d = 1.061" = 2.695$ cm we find

$$\frac{U_0}{U_{\text{approx}}} = \frac{V_{\text{eff}}}{V_{\text{cav}}} = 0.2. \tag{6.37}$$

This shows that the actual energy in the cavity is about 5 times smaller than it would be if one ignored the integration and approximated the effective volume by the actual volume of the cavity for the TE_{011} mode.

The value of peak magnetic field now follows from equations (6.29) and (6.35)

$$H_0 = \sqrt{\frac{16\beta P_f Q_0}{\mu_0 \pi R^2 d J_0^2(\lambda_{11}) \left(\left(\frac{\pi R}{\lambda_{11} d} \right)^2 + 1 \right) (1_\beta)^2 \omega_0}} = \sqrt{\frac{16\beta P_f Q_0}{\mu_0 V_{\text{eff}} (1+\beta)^2 \omega_0}}. \tag{6.38}$$

For our aluminum cavity we can reduce this result in terms of the forward traveling power, intrinsic quality factor and resonant frequency

$$H_0 = 2.61 \times 10^5 \sqrt{\frac{P_f Q_0}{\omega_0}}, \tag{6.39}$$

in SI units, and with a value of $\beta = 1$ which corresponds to perfect input coupling (i.e. maximum energy transfer into cavity).

6.2 Numerical estimates of Membrane displacement

In section **??** we found the solution to the equation of motion for the damped-driven membrane when excited by a TM_{010} and TE_{011} EM mode in a RF cylindrical cavity. We now estimate the maximum displacement amplitude of the membrane for the case when the electromagnetic modes are coupled to the fundamental vibrational mode of the membrane.

6.2.1 Coupling of the TM_{010} Mode to the Fundamental Acoustic Mode

The maximum displacement at the center of the membrane ($r = 0$) follows from equation 6.13

$$u_{\max}(r=0) = \frac{P_f Q_{0RF}}{\pi m f_{010} d} \sum_n \frac{a_n + b_n}{\sqrt{(\omega_{0n}^2 - \Omega^2)^2 + 4\beta^2\Omega^2}}, \tag{6.40}$$

where, we have assumed perfect coupling of the cavity and RF forward traveling power, $\mathcal{E}_0^2 = 8P_f Q_{0RF}/\omega_{010} V \epsilon_0$ with the approximation that the effective volume (V) is given by the volume of the cavity for the TM_{010} mode, d is the length of the cavity, f_{010} is the resonant frequency of the cavity [2], Q_{0RF} is the cavity's intrinsic Q, P_f is the RF forward traveling power, and m is the mass of the membrane. All quantities are in SI units. The parameters for our RF copper cavity and PVC membrane are $m = 22$ mg, $d = 4$ cm, $P_f = 10$ mW, $Q_{0RF} = 200$, $\beta = 6$ rad/s, $\Omega = 2\pi \times 1118$ Hz, and $f_{010} = 8.72$ GHz, and we find $u_{\max} \sim 1.0$ nm. A plot of the solution for the first 20 terms in the series of the membrane driven at the first resonance with the given parameters is plotted in figure 6.3.

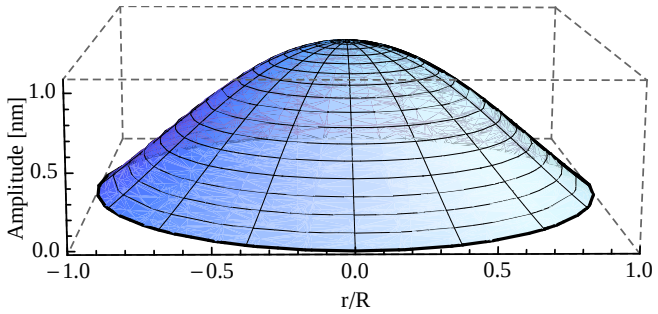

Figure 6.3: (Color) The Bessel series solution, equation 6.13, plotted for the first 20 terms in the series when driven at the fundamental resonance. Parameters are in the text.

6.2.2 Coupling of the the TE_{011} Mode to the Fundamental Acoustic Mode

Similarly, the maximum displacement of the membrane when driven by a TE_{011} mode follows from equation (6.26) and (6.39),

$$u_{\max}(r=0) = .003\mu_0 \frac{P_f Q_{0RF}}{m} \sum_{n=1}^{\infty} \frac{c_n}{\sqrt{(\omega_{0n}^2 - \Omega^2)^2 + 4(\beta\Omega)^2}}, \tag{6.41}$$

[2] Its assume that the RF signal is tuned to this resonant frequency of the cavity.

where Q_{0RF} is the cavity's intrinsic Q factor, m the mass of the membrane, P_f is the forward traveling power into the cavity, c_n are Bessel coefficients, β is the damping constant, and we have used the frequency of 11.1 GHz which corresponds to our aluminum cavity with $R = 3.81$cm and $d = 2.695$cm. All quantities are in SI units. A maximum displacement on the order of 0.2 micro-meter can be achieved with the following parameters: $m = 22$mg, $Q_{0RF} = 2 \times 10^4$, $P_f = 10$mW, $\beta = 6$. The membrane's mode of oscillation is shown in figure 6.4 for the first 20 terms.

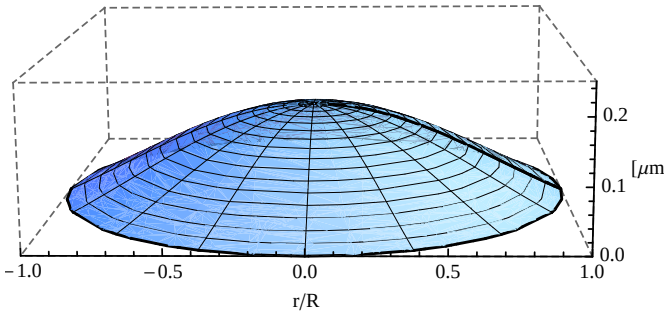

Figure 6.4: Elastic membrane excited at its fundamental resonance by a TE_{011} RF mode modulated at the membrane's resonant frequency. Maximum displacement on the order of 0.2 micro-meter.

6.2.2.1 High Frequency Limit in SRF cavity with TE_{011} mode

In the high frequency regime, in which the membrane is driven at a frequency much higher than its natural frequencies ($\omega >> \omega_{0n}$), the amplitude is approximately

$$A_n \approx .003\mu_0 \frac{P_f Q_0}{m} \sum_n \frac{c_n}{(2\omega)^2} \tag{6.42}$$

For the purpose of illustration, let us assume that we drive the membrane at the second harmonic of the resonant frequency of the RF cavity, $2 \times \omega = 2\pi \times 11.1$ GHz, with $Q_{0RF} = 1 \times 10^9$, $P_f = 10$mW, and $m = 22$mg. With these parameters, the maximum displacement amplitude of the membrane in the free mass limit, is estimated on the order of 2 atto-meters. Figure 6.5 shows the mode of oscillation in the free mass limit regime. Figure 6.6 shows a cross-sectional view of the elastic mode of oscillation.

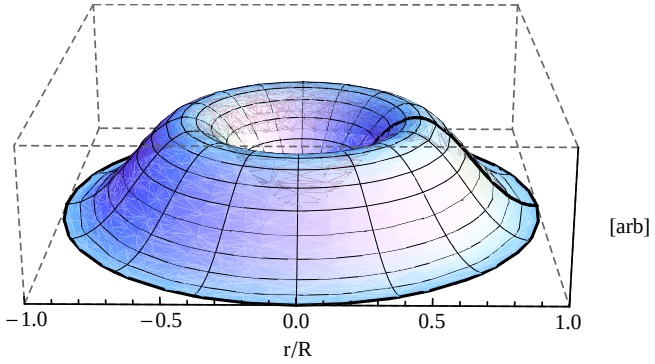

Figure 6.5: Elastic membrane driven at the second harmonic of the RF drive way above any of its natural resonances, the free mass limit.

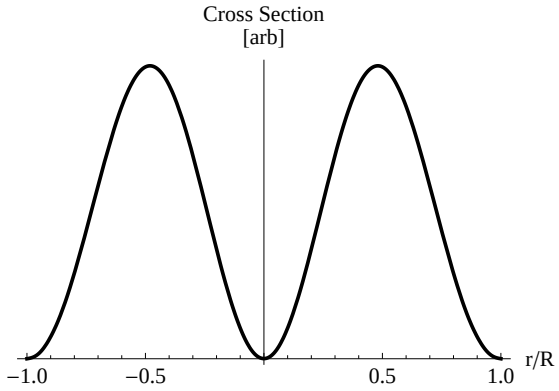

Figure 6.6: Cross section view of elastic mode when driven at the second harmonic of the cavity's resonant frequency 11.1GHz.

6.3 Detection of Membrane Vibration Excitation

We use a TM_{010} mode at 8.74 GHz in a copper RF cylindrical cavity to excite the fundamental vibrational mode of a thin PVC elastic membrane with a thin 50nm gold film coating on one side. For more details on this cavity see sections **??** and 4.8. The purpose of the gold film is to provide good electrical contact with the cavity and to act as a mirror for laser reflection. The cavity's dimensions are shown in figure 6.7. For detection of the membrane's vibration two techniques were used. First as a preliminary set up, we used a laser deflection technique to detect the motion of the membrane. However, this scheme cannot measure the displacement amplitude of the membrane, and served as a proof of concept. The second scheme used interferometry to detect and measure the displacement amplitude of the membrane.

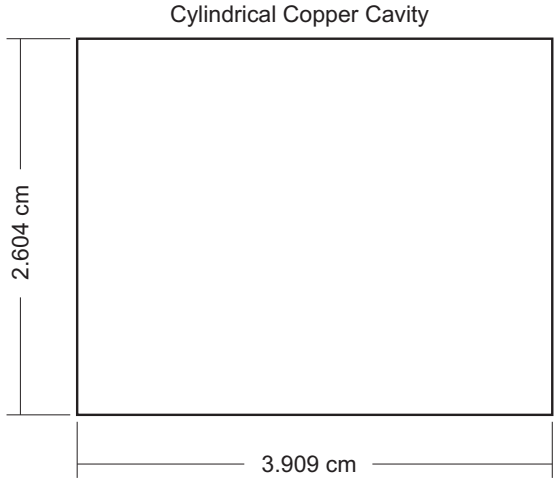

Figure 6.7: The dimensions of the copper cylindrical cavity used to excite the vibrational modes of a thin elastic membrane placed at one end of the cavity.

6.3.1 Deflection Scheme

This scheme consisted of a laser aimed at the center of the membrane at a large angle of incidence, the beam was then directed through a small aperture (iris) and finally incident on a photodiode detector. As the membrane vibrates the laser beam is slightly deflected and the intensity reaching the photodiode detector is modulated via the small aperture. The entire set up is placed in a small home-built plexiglass vacuum chamber. Signal detection was done via a SRS 830 Lock-in amplifier and a Labview VI. This scheme is illustrated in figure 6.8.

The use of a speaker for excitation of the membrane in order to tune the scheme was extremely helpful. The speaker provided large vibration amplitudes, which in turn generated detection signals that were easier to detect. Data obtained using a speaker as the source of excitation is shown in figure 6.9. Once proper alignment was achieved, and the fundamental resonant frequency located, we used an automated sweep Labview VI with the Lock-In amplifier to detect the vibration of the membrane caused by the modulation of the RF power in the cavity. Data obtained using this technique is diplayed in figures 6.10a and 6.10b. It was observed that the resonant frequency decreased over a period of a day by about 20 Hz. This is associated with degradation, loss of tension over time, and mostly due to the PVC material used for membrane construction. This preliminary scheme was useful in establishing the proof of

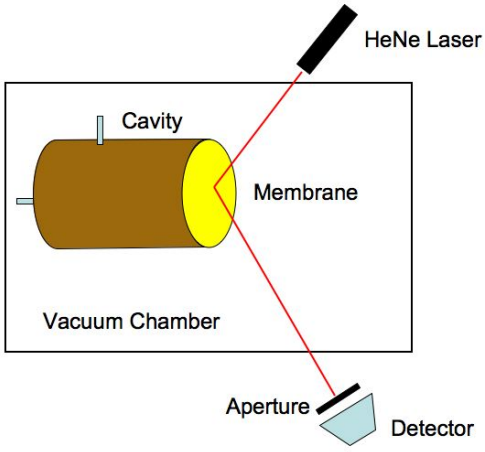

Figure 6.8: The deflection scheme uses a 632 HeNe laser reflected from the back of the gold coated membrane through a small aperture and into a photodiode detector. As the membrane vibrates it changes the deflection angle which results in an intensity modulation via the small aperture. Signal detection was done via a SRS 830 Lock-In amplifier.

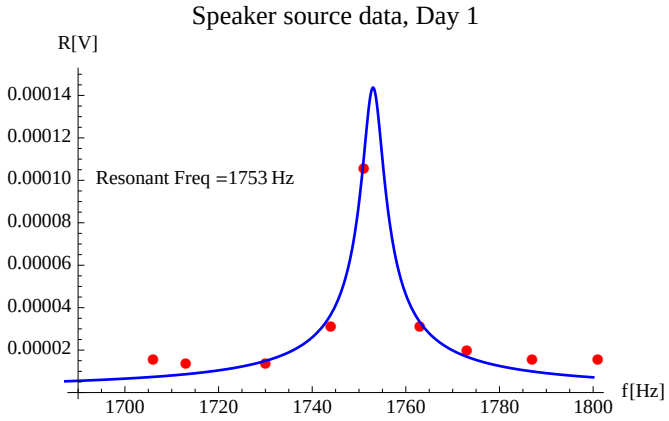

Figure 6.9: (Color) Voltage signal recorded from photodiode detector with Lock-In amplifier while driving the membrane with a speaker. The solid curve is a Lorentzian fit. Dots represent data points.

concept, namely that the RF fields in a cylindrical cavity can drive into motion a large mechanical membrane placed at one end. To measure the membrane displacement, we implement an interferometric scheme.

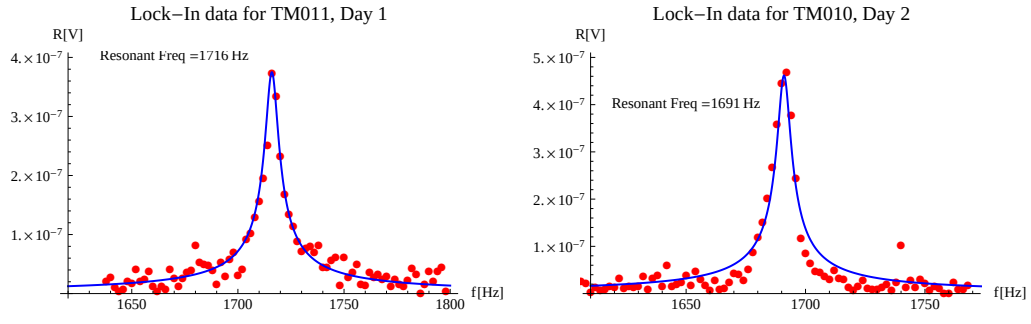

(a) **(b)**

Figure 6.10: (Color) Voltage signal from Lock-In when membrane is driven by a TM_{010} mode at 8.74 GHz. On day one the membrane's resonance is at 1716 Hz. On day two it has shifted to 1691 Hz. Blue curves are Lorentzian fits, data points are represented by red dots.

6.3.2 Interferometric Scheme

Here we examine the Michelson interferometer measurement scheme in detail for the case of an unbalanced interferometer with non-zero optical path difference. In addition, we implement the use of an optical filter via a single mode fiber optic to avoid distortion problems of the interference pattern caused by poor reflection quality from the gold coated membrane, and to compensate for the non-zero optical path difference. Noise reduction was achieved by placing the interferometer inside a ~ 50 mbar vacuum chamber pumped down with a roughing pump. This scheme provides high sensitivity and easy set up, but the major limitations are ambient vibrational and acoustical noise.

The intensity of the interference pattern of a Michelson interferometer is

$$I = I_1 + I_2 + 2\sqrt{I_1 I_2}\cos(\delta), \tag{6.43}$$

where I_1 and I_2 are the intensities of each arm, and $\delta = k\Delta_r + k\Delta_p$ is the total optical path difference gained between the two beams from reflection and path difference[3].

The gold coated membrane is used as one of the mirrors of the Michelson interferometer. Since the membrane undergoes sinusoidal motion, the modulation of the

[3] $k = 2\pi/\lambda$ is the wavenumber, Δ_p is the optical path difference, and $\Delta_r = \lambda/2$ is the net phase gained by the beam splitter reflection coefficient (i.e. $-1 = e^{i\pi}$, or $k\Delta_r = \pi$)

optical path is given by

$$\Delta_p \rightarrow \Delta_p(t) = 2l + 2x_0 \sin(\omega_s t). \tag{6.44}$$

Note that l is a net optical path difference, ω_s is the oscillation frequency of the membrane, and x_0 is the amplitude of oscillation of the gold coated membrane ($u_{\max}$).

Let us focus our attention on the interference term involving the $\cos(\delta)$ in equation (6.43). With $\delta = k\Delta_r + k\Delta_p$ along with the cosine sum formula we find

$$\cos\delta = \cos(k\Delta_r)\cos(k\Delta_p(t)) - \sin(k\Delta_r)\sin(k\Delta_p(t)) = -\cos(k\Delta_p(t)), \tag{6.45}$$

where we used the fact that $k\Delta_r = \pi$. From equation (6.44) we find

$$-\cos(k\Delta_p(t)) = -[\cos(2kd)\cos(2kx(t)) - \sin(2kd)\sin(2kx(t))], \tag{6.46}$$

where we define $x(t) \equiv x_0 \sin(\omega_s t)$. We now assume that the amplitude of oscillation of the membrane is very small ($kx_0 << 1$) and use the small angle approximation,

$$-\cos(k\Delta_p(t)) \approx -\cos(2kd) + 2kx_0 \sin(2kd)\sin(\omega_s t). \tag{6.47}$$

Hence, when the amplitude of oscillation of the membrane is small as compared to the wavelength, the intensity is given by

$$\begin{aligned} I(t) = \quad & I_1 + I_2 - 2\sqrt{I_1 I_2}\cos(2kd) \\ & +4kx_0\sqrt{I_1 I_2}\sin(2kd)\sin(\omega_s t). \end{aligned} \tag{6.48}$$

The intensity in equation 6.48 is composed of DC and AC components. We eliminate the DC component by AC coupling the signal into our measurement device. AC coupling effectively differentiates the input signal so that it eliminates the DC component. For conversion of the light intensity to a voltage we use a Thorlabs FDS 100 Si photodiode detector in a photoconductive mode with a basic op amp circuit to insure the detector is not affected by the external loads of the measuring instruments. In this configuration the output voltage of the photodiode detector scales linearly with the

intensity,

$$V(I) = V_0 + \mathcal{R}I, \tag{6.49}$$

where V_0 is some DC offset and a constant [4]. Here $\mathcal{R}(\lambda)$ is constant for a given wavelength, usually denoted as the responsivity. Intensity linear response from the detector was verified with a calibrated OPHIR Orion-PD power meter. Frequency linear response from DC to 5 KHz was verified with the aid of a New Focus 3501 optical chopper.

Solving for the intensity in equation (6.49), we find $I = \Delta V/\mathcal{R}$, where $\Delta V \equiv V(I) - V_0$. Under the assumption of a linear photodetector the AC part in equation (6.48) becomes

$$\frac{V(I)}{\mathcal{R}} = 4kx_0\frac{\sqrt{\Delta V_1 \Delta V_2}}{\mathcal{R}}\sin(2kd)\sin(\omega_s t), \tag{6.50}$$

from which it follows that the voltage signal is independent of the responsivity ($\mathcal{R}$) and eliminates the need of a calibrated photodetector. The voltages ΔV_1 and ΔV_2 must be measured from the reference voltage V_0. The voltage signal from the photodiode becomes

$$V_s(t) = \alpha\sin(\omega_s t + \theta_s) \tag{6.51}$$

where $\alpha \equiv 4\sqrt{\Delta V_1 \Delta V_2}\sin(2kd)kx_0$, and θ_s is an arbitrary phase that may be acquired during the signal processing. The displacement amplitude is extracted from a measurement of $V_s[\text{rms}] = V_s/\sqrt{2}$ using a SR830 Lock-In amplifier. From equation (6.51) we find

$$x_0 = \frac{\sqrt{2}V_s[\text{rms}]\lambda}{4\pi\sqrt{\Delta V_1 \Delta V_2}\sin(2kd)}, \tag{6.52}$$

with $kx_0 << 1$.

The optical phase added by the net optical path difference is tuned so that $\sin(2kd) = 1$. This is achieved by tuning the interference intensity with a piezo electric actuator to the point of maximum sensitivity. This occurs when the total voltage is equal to the sum of the individual voltages from each arm of the interferometer; $\Delta V = \Delta V_1 + \Delta V_2$. This tuning is done prior to any modulation, i.e., the DC term is set so that $I = I_1 + I_2 - 2\sqrt{I_1 I_2}\cos(2kd) = I_1 + I_2$ which is satisfied when $d = (2n+1)\lambda/8$,

[4] This offset accounts for dark current and any initial DC voltage offset present in the photodiode detector and is measured when no light intensity is incident on the detector.

where n is an integer. With proper tuning we set $\sin(2kd) = 1$ and the displacement of the membrane is extracted from a measurement of the DC and *rms* voltages

$$x_0 = \frac{\sqrt{2}V_s[\text{rms}]\lambda}{4\pi\sqrt{\Delta V_1 \Delta V_2}}. \tag{6.53}$$

Measurements preformed used a 10mW helium-neon 633 nm laser as the light source. The DC voltages (ΔV_1 and ΔV_2) were measured with an oscilloscope. Solenoid-actuated blockers were used to block the beams as necessary to measure each arm intensity. A piezo-electric actuator was used to tune the interference pattern to its most sensitive setting as described above. The *rms* voltage was measured with an SRS 830 DSP lock-in amplifier, and the lock-in reference signal was used to amplitude modulate the HP 8684B RF signal generator at the reference frequency. A Labview VI program automatically swept the reference frequency and recorded the *rms* voltage measurement from the lock-in. Since, the measurements can be done relatively fast no feedback loop was implemented. The measurement scheme is illustrated in figure 6.11.

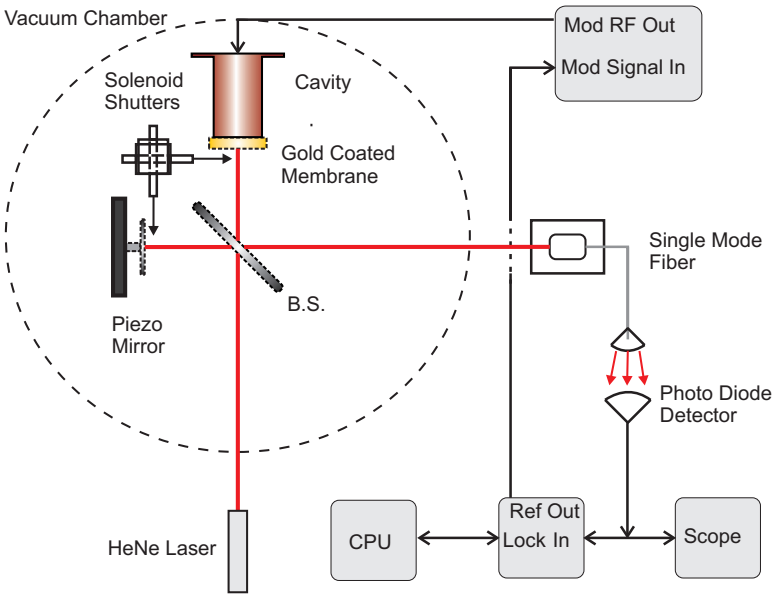

Figure 6.11: (Color) Experimental Scheme for membrane displacement measurement using inteferometry.

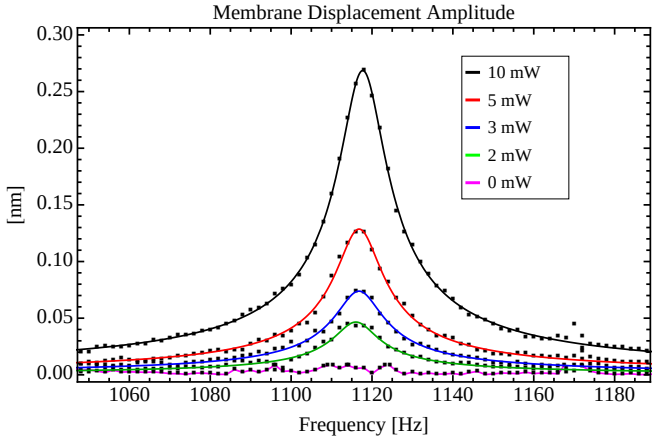

Figure 6.12: (Color) Experimental data and fits to equation (6.13) (solid curves) for different RF powers of the TM_{010} mode. For 10 mW of forward traveling power the displacement amplitude is approximately 0.3 nm at a resonance frequency of approximately 1118 Hz.

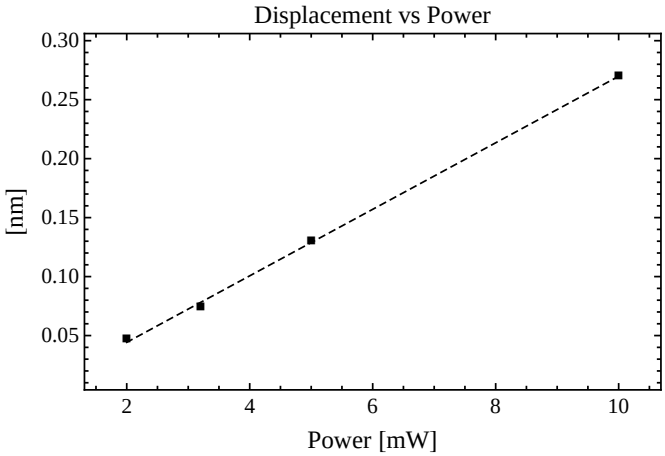

Figure 6.13: Membrane displacement amplitude plotted against RF forward traveling power. The dash line is a linear fit to the experimentally measured values.

6.3.3 Measurement of Membrane Displacement Using IFO Scheme

The membrane's fundamental resonance was observed at 1118 Hz. Figure 6.12 shows the experimental data for different RF forward traveling powers, the solid curves are fits to equation (6.13) from which we can extract the amplitude and resonance frequency of the membrane's vibration with the use of equation (6.53). To confirm excitation of the main resonance we varied the RF forward traveling power. From equation (6.40) we see that the power scales linearly with the amplitude of oscillation of the membrane. This

linear relationship is clearly displayed in figure 6.13. The mechanical Q of the membrane is calculated from the experimental results and is on the order of 100. Furthermore, the excitation of the membrane resonance was confirmed using an acoustical measurement with a speaker tuned to the main fundamental resonant frequency.

Higher order acoustical modes where also observed with lower oscillation amplitude as can be seen in figures 6.14 and 6.15a. For comparison a control run was preform with the power modulation turned off and the RF power level set to -120 dBm. Leaving the equipment on plays an important role in assuring that the observed modes are not artifacts of equipment noise. The full scan of the noise is displayed in figure 6.15b.

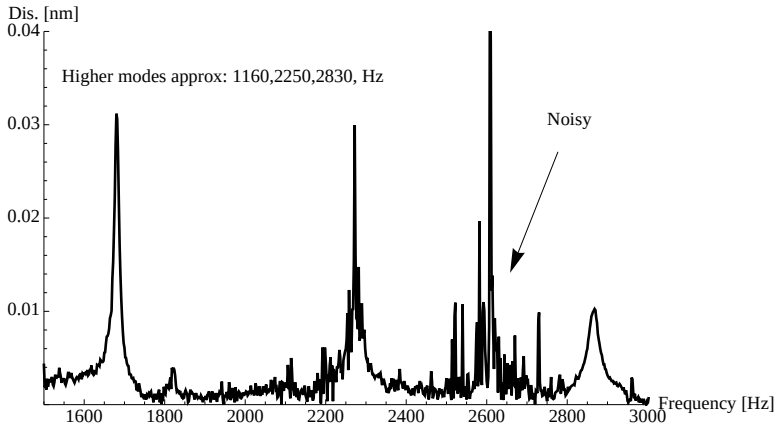

Figure 6.14: Higher order acoustic modes excited via a TM_{010} RF mode.

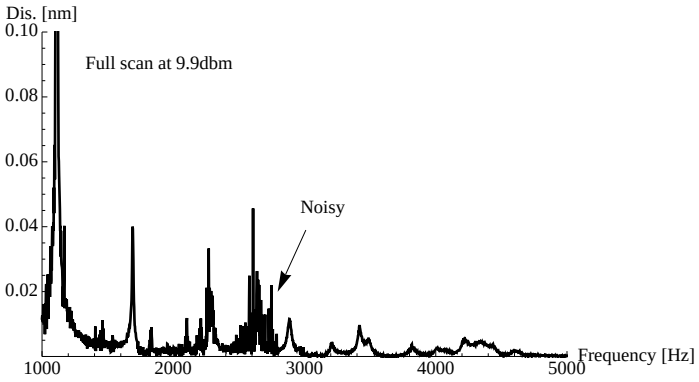

(a) Full scan shows all observable modes and noise regions.

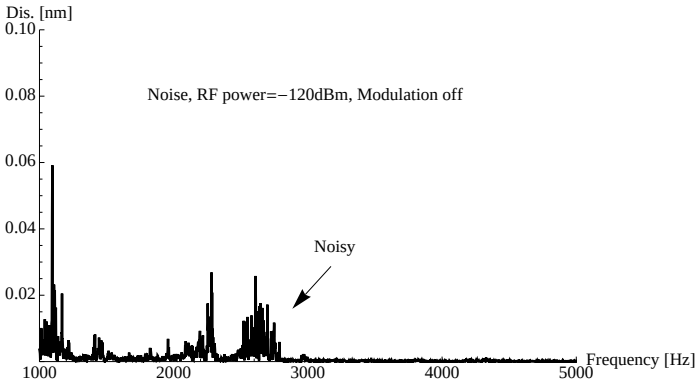

(b) Full scan with modulation turned off but leaving equipment on and power input set to -120 dBm shows the acoustic noise present.

Figure 6.15: Comparison of figures (a) and (b) shows the acoustic modes excited via the TM_{010} mode in the RF cylindrical cavity.

7

Pondermotive Effects and Practical Considerations

7.1 Ponderomotive effects: Damping in a Fabry Perot

We begin with a review of Braginsky's 1967 paper [30] where he first pointed out the existence of a electromagnetic damping associated with moving mirrors. Although this is typically a small effect, Braginsky noted that the effect could be greatly enhanced with the existence of high-Q resonators [31]. Indeed, his work pave the way for cavity optomechanics where this effect is exploited with the use of high-Q resonators.

Consider a mirror moving to the right with constant velocity v for some fixed period of time $T/2$, subsequently suppose this mirror moves in the opposite direction with velocity $-v$ for a time $T/2$. Ignoring acceleration periods, the mirror undergoes a full cycle in a total time T. If a right traveling electromagnetic wave (light) is incident on the moving mirror it will experience a Doppler shift. While the mirror is moving to the right the light of frequency ω would be red-shifted to a frequency ω_- upon reflection. Similarly, while the mirror is moving to the left light would be blue-shifted to a frequency ω_+ upon reflection. The shift in frequency is calculated by the Doppler formulas

$$f_- = f\left(\frac{1-v/c}{1+v/c}\right) \quad \text{for red-shifted light, and} \tag{7.1}$$

$$f_+ = f\left(\frac{1+v/c}{1-v/c}\right) \quad \text{for blue-shifted light,} \tag{7.2}$$

where c is the speed of light, and $\omega = 2\pi f$. At the single photon level one can imagine that if the mirror is at rest then the energy spectrum consist of a single energy level hf. However, when the mirror undergoes a full cycle of motion the energy spectrum consist of two different photons, one with energy hf_- and the other with energy hf_+. If we consider N photons reflecting from the moving mirror during one full cycle we may write the total averaged energy as

$$U = \frac{1}{2}\left[Nhf_+ + Nhf_-\right] = \frac{1}{2}Nhf\left[\left(\frac{1+v/c}{1-v/c}\right) + \left(\frac{1-v/c}{1+v/c}\right)\right]. \tag{7.3}$$

In the limit where $v << c$ we can expand this expression up to order $(v/c)^2$,

$$\approx \frac{1}{2}Nhf\left[(1+v/c)(1+v/c+(v/c)^2) + (1-v/c)(1-v/c+(v/c)^2)\right], \tag{7.4}$$

and after some algebraic simplification we find

$$< U >= Nhf\left[1 + 2\left(\frac{v}{c}\right)^2\right]. \tag{7.5}$$

Because the average energy is directly related to the average intensity as given by the Poynting vector $< S > \propto < U > \propto Nhf$, we can write equation (7.5) as

$$< S > + \frac{2 < S > v^2}{c^2}. \tag{7.6}$$

Observe that the second term involving $(v/c)^2$ is an extra energy that must be supplied by the external mechanical source moving the mirror. That is, this energy is associated with the friction of light acting on the mirror. This important result can be stated more clearly by identifying the radiation pressure $P_{\text{rad}} \equiv < S > /c$, so that equation (7.6) becomes

$$P_{\text{rad}}c + 2P_{\text{rad}}\frac{v^2}{c} = P_{\text{rad}}c + 2P_{\text{rad}}\frac{v}{c}\cdot v \tag{7.7}$$

$$\equiv P_{\text{rad}}c + F_{\text{fr}}\cdot v, \tag{7.8}$$

where we define the drag friction coefficient $b \equiv 2P_{\text{rad}}/c = 2 < S > /c^2$. With this definition, the drag force (per unit area) associated by the reflection of light from a

moving boundary with constant velocity is

$$F_{\text{fr}} \equiv b \cdot v. \tag{7.9}$$

As it stands this effect is miniscule due to the factor of $(v/c)^2$, however as Braginsky pointed out, this effect can be enhanced with the use of high-Q resonators.

The electric field inside a Fabry-Perot cavity of length d (see section 2.2) is

$$E_{01}^{+} = \frac{t}{1 - r^2 e^{-i\delta}} E_{0P}, \tag{7.10}$$

where we revert to using t to denote for the amplitude transmission coefficient, r the reflection coefficient which is assumed to be identical for both mirrors of the FP, and E_{0P} is the electric field of the external pump beam. Since the radiation pressure is proportional to E^2, at resonance ($\delta = 2\pi m$) we find

$$(E_{01}^{+})^2 = \frac{E_{0P}^2}{1 - r^2} = \frac{E_{0P}^2}{t^2} = \frac{\mathcal{F} E_{0P}^2}{\pi r}, \tag{7.11}$$

where $\mathcal{F} \equiv \pi r/(1-r^2)$ is the finesse. From the definition of the Poyting vector $< S >= c\epsilon_0 E^2/2$, the radiation pressure on a mirror inside a Fabry-Perot at resonance is

$$P_{\text{rad}}^{\text{mirror}} = 2\frac{< S_{0P} >}{ct^2}. \tag{7.12}$$

For very good Fabry-Perot interferometers values under 10^{-2} can easily be achieved for t^2. Therefore, the radiation force is significantly enhanced when a high-Q resonator is used.

When one mirror of the FP is displaced by a small amount ϵ, it will shift the resonance curve, thus, the resonance frequency (or length) will no longer coincide with the frequency of the pump beam. That is, the frequency f will no longer be in resonance with the resonant frequency of the FP f_0. From equation (7.10) the radiation pressure on the mirror when the FP is off resonance is

$$P_{\text{rad}}^{\text{mirror}}(\delta) = \frac{2t^2}{(1 + r^4 - 2r^2\cos(\delta))} \frac{< S_{0P} >^2}{c}, \quad \text{where} \quad \delta = 2kd, \tag{7.13}$$

and d is the length of the FP cavity. If there is a small displacement ϵ from the

equilibrium (resonance), i.e. $2kd \rightarrow 2k(d+\epsilon)$ we find

$$P_{\text{rad}}^{\text{mirror}}(\epsilon) = \frac{2t^2}{(1+r^4-2r^2\cos(2k\epsilon))}\frac{< S_{0P} >^2}{c}, \tag{7.14}$$

where we used the small angle approximation. Because the resonance has a length dependance, there is a force that arises when the mirror is displaced. This force gives rise to an effective spring constant

$$K_{\text{op}} \equiv \frac{\partial P_{\text{rad}}^{\text{mirror}}}{\partial x}. \tag{7.15}$$

In addition, there exist a value of $x = \epsilon_{\max}$ for which this effect is a maximum

$$K_{\text{op}}^{\max} = \frac{\partial P_{\text{rad}}^{\text{mirror}}}{\partial x}|_{\epsilon_{\max}} \tag{7.16}$$

Before we find an explicit expression for the optical spring constant in equation (7.16), we note a few results for the FP that will be helpful in the process and find an expression for the quality factor in a low-loss FP cavity. For very high reflective mirrors ($t^2 << 1$), the Finesse of a FP is approximately

$$\mathcal{F} = \frac{\pi r}{1-r^2} \approx \frac{\pi}{1-r^2} = \frac{\pi}{t^2}. \tag{7.17}$$

The number of round trips that a photon makes inside the Fabry-Perot is

$$N_{\text{rt}} = \frac{\tau_p}{\tau} = \frac{1}{2(1-r^2)}, \tag{7.18}$$

where τ_p is the photon life time and $\tau = 2d/c$ is the round trip time. Since the decay rate Γ is inversely proportional to the photon life time $\tau_p = \tau N_{\text{rt}}$, it follows that

$$\Gamma = \frac{2}{\tau}(1-r^2) = \frac{t^2 f\lambda}{d} \approx 2\pi(2\Delta f_{1/2}), \tag{7.19}$$

where $2\Delta f_{1/2} = f_{fsr}/\mathcal{F}$ is the FWHM, and $f_{fsr} = c/2d$ is the free spectral range of the FP. From equation (7.19) it follows that the quality factor of the FP (Q_{FP}) for low loss mirrors is given by

$$Q_{FP} \approx \frac{2\pi f}{\Gamma} = \frac{2\pi d}{t^2\lambda}, \tag{7.20}$$

where $f\lambda = c$, and c is the speed of light. Equation (7.28) shows that the quality factor in a high-finesse FP is directly proportional to the length of the optical cavity, hinting at the fact that a gradient arises when the length of the FP cavity is perturbed.

A simple derivation of the optical spring constant as discussed by Branginsky [30] is now presented. It is shown that the length dependance of the resonance in the FP gives rise to an optical spring constant when one of the mirrors in the Fabry-Perot is allowed to move in such a way that it modulates the length of the cavity. The optical spring constant arises from the gradient of the radiation pressure along the motion of the mirror. Taking the approximation that the gradient is on the order of the maximum slope along the Lorentzian as depicted in figure 7.1, the optical spring constant is

$$\frac{\partial P_{\text{rad}}^{\text{mirror}}}{\partial x} \approx \frac{\Delta P_{\text{rad}}^{\text{mirror}}}{\epsilon_{\max}} \tag{7.21}$$

From figure 7.1 observe that

$$\Delta P_{\text{rad}}^{\text{mirror}} = \frac{P_{\text{rad}}^{\text{mirror}}}{2}, \tag{7.22}$$

$\epsilon = 2\Delta d_{1/2}/2$, where the HWHM (in units of length) for a FP is given by

$$\Delta d_{1/2} = \frac{d_{fsr}}{2\mathcal{F}} = \frac{\lambda t^2}{4\pi} \approx \epsilon_{\max}, \tag{7.23}$$

and $t^2 + r^2 = 1$. From equations (7.22) and (7.23) the maximum optical spring constant is

$$\frac{\partial P_{\text{rad}}^{\text{mirror}}}{\partial x}|_{\max} \approx \frac{\Delta P_{\text{rad}}^{\text{mirror}}}{\epsilon_{\max}} = \frac{P_{\text{rad}}^{\text{mirror}}}{2\epsilon_{\max}} = \frac{4\pi < S_{0P} >}{\lambda c t^4} \equiv K_{0P}^{\max}. \tag{7.24}$$

In general this spring constant can be positive or negative depending which side of the Lorentzian curve is chosen, see figure 7.1. This freedom in the choice of the sign allows for optical "heating" or "cooling" of the motion of the mirror, and is a common technique used in optomechanics.

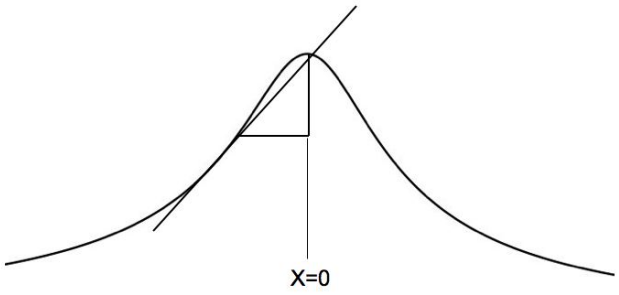

Figure 7.1: Approximation of the gradient by the slope leads to Braginsky's result for the optical spring constant in a high-Q Fabry-Perot Resonator.

7.2 Pondermotive effects: Damping in a RF Cylindrical Cavity

In the preceding section is was shown that a moving mirror in a Fabry-Perot cavity experiences a damping force due to the large gradient that exist as the mirror is slightly displaced from resonance. Similarly, the same effect in a RF cavity is expected. Indeed, in this section it is shown that a moving boundary in an RF cylindrical cavity can experience a damping force just like in the Fabry-Perot case.

The magnitude of the time averaged force per-unit area on the end-boundary of a cylindrical cavity excited in a TE_{011} mode is

$$< T_{zz} >= f(r)\frac{U_0}{L_0^2 V_{\text{eff}}}, \quad \text{where } f(r) \equiv \frac{1}{2}\left(\frac{\pi R}{\lambda_{11}}\right)^2 J_1^2(\lambda_{11}\frac{r}{R}), \tag{7.25}$$

U_0 is the total energy stored in the cavity, $\lambda_{11} = 3.8317$ is a Bessel zero, R is the radius of the cavity, and L is the variable used to denote the length of the cavity. Note that we will use L_0 to indicate constant length of the cavity for a particular resonance value, and that calculation of the total force over the boundary requires integration over r. For simplicity assume that the expressions for the cavity resonant fields are not perturb by the moving boundary, and that the effective volume of the cavity when the end-boundary is displaced by a very small amount remains constant.

In this approximation only the energy in the cavity is allowed to vary as a function of the displacement of the boundary from resonance. Furthermore, as it is required for our experimental application, the excitation source frequency (ω) is kept constant so that only the resonance length (L) is allowed to vary. This is contrary to the usual treatment where the resonance frequency (ω_0) is kept constant and the external source frequency is varied. Hence, the "optical" spring constant for a moving boundary in an RF cylindrical cavity follows from the gradient of the radiation pressure along the motion of the boundary,

$$\frac{\partial < T_{zz} >}{\partial L} = f(r)\frac{1}{L_0^2 V_{\text{eff}}}\frac{\partial U_0}{\partial L}. \tag{7.26}$$

The derivative is straight forward, but care must be taken in what is allowed to vary. In deriving an explicit expression for equation (7.26), we mention some important results that naturally arise along the way. Lets begin with the total stored energy in the cavity which is given by

$$U_0 = \frac{4P_f\omega^2\omega_0^2 Q_0}{4\omega^2\omega_0^2 + Q_0^2(\omega^2 - \omega_0^2)}, \tag{7.27}$$

where Q_0, and ω_0 are functions of the cavity length given by

$$Q_0(L) = .610\frac{\lambda}{\delta}\frac{[1 + .168(\frac{2R}{L})^2]^{3/2}}{1 + .168(\frac{2R}{L})^3} \quad \text{and} \tag{7.28}$$

$$\omega_0(L) = \frac{\pi}{R}\sqrt{A + B\left(\frac{2R}{L}\right)^2}, \tag{7.29}$$

where $A = (c\lambda_{11}/\pi)^2$, and $B = (c/2)^2$ with c being the speed of light in SI units, δ is the skin depth, and λ is the wavelength of the input frequency source. It is convenient to express the ratio λ/δ in equation (7.28) in terms of the relevant parameters of our 11.1 GHz aluminum cylindrical cavity

$$\frac{\lambda}{\delta} = \frac{56.6}{\sqrt{\rho[\Omega\text{-cm}]}}, \tag{7.30}$$

where $\rho[\Omega\text{-cm}]$ is the resistivity of the material (aluminum in our case) in units of Ohm-cm. From equation (7.28) it is evident that for our aluminum cavity with $R = 1.905$ cm, and $L = 2.695$ cm $Q_0 \sim 3 \times 10^4$. It is interesting to point out, as can be seen

from equation (7.28), that the only way of obtaining high Q values for a given mode is by lowering the resistivity. Although, the resistivity can be related to the surface resistance of the cavity (see section 4.3), it is worthwhile to calculating the effective resistivity required to achieve a Q on the order of 10^9. We find that $\rho_{\text{eff}} \sim 1.3\times10^{-15}$ Ω-cm. This is to be compared with the value for bulk aluminum at room temperature $\rho_{\text{Al}} = 2.65 \times 10^{-6}$ Ω-cm.

The derivatives of ω_0 and Q_0 are

$$\frac{\partial\omega_0}{\partial L} = -\frac{(2\pi)^2 B}{\omega_0 L^3}, \text{ and} \tag{7.31}$$

$$\frac{\partial Q_0}{\partial L} = -.307\frac{(2R)^2\lambda}{L^3\delta}[1 + .168\left(\frac{2R}{L}\right)^2]^{1/2}\frac{1-\left(\frac{2R}{L}\right)}{[1+.168\left(\frac{2R}{L}\right)^3]^2}, \tag{7.32}$$

respectively. Equation (7.31) gives an approximation of how the resonant frequency in the aluminum RF cavity changes as a function of the length of the cavity. When a small displacement (ΔL) is made from the original resonance length L_0, the resonant frequency changes by an amount

$$\Delta f \approx -\frac{B}{f_0 L_0^3}\Delta L. \tag{7.33}$$

Alternatively, rewriting this result in terms of the length displacement we find

$$\Delta L = -\frac{f_0 L^3}{B}\Delta f. \tag{7.34}$$

A plot of equation (7.33) is illustrated in figure 7.2. We add that an experiment in which the length of an aluminum cavity was varied confirmed this relation, the results are illustrated in figure 7.3. The experimental data was fitted to the linear function

$$\Delta f = a\Delta L, \tag{7.35}$$

where a is a fit parameter. The fit yielded $a = -110$ Hz/nm, which is within 6% of the theoretical predicted value, $-B/f_0L_0^3 = -104$ Hz/nm. In addition, note that the HWHM in terms of length and frequency, can be calculated from equations (7.33) and (7.34), respectively. In doing so we find the cavity's HWHM in units of length, i.e. the

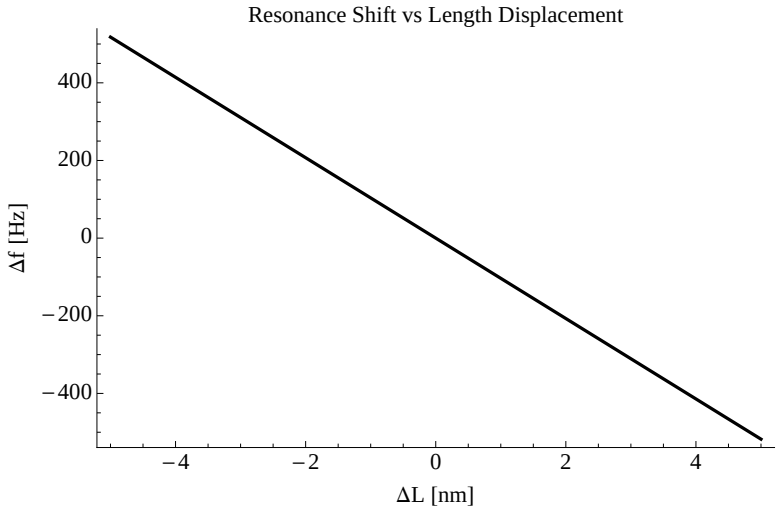

Figure 7.2: Plot of equation (7.33) predicts the shift in the resonance frequency of the cavity when its length is changed by a small amount. Note that this is completely independent of cavity's Q factor. The theoretical predicted value for the slope is -104 Hz/nm.

amount of displacement needed at the boundary to reduce the energy by half, to be

$$\Delta L_{1/2} = \frac{f_0^2 L_0^3}{2BQ_0}, \tag{7.36}$$

where $Q_0 = f_0/2\Delta f_{1/2}$ and $\Delta f_{1/2} \equiv$ HWHM. For a cavity with $L_0 = 2.695$ cm, $R = 1.905$ cm, a resonance at 11.1 GHz, and a $Q_0 \sim 10^9$ the HWHM ($\Delta L_{1/2}$) is on the order of 54 pm. In terms of frequency, this length corresponds to $\Delta f_{1/2} = 5.6$ Hz. A plot of equation (7.36) is shown in figure 7.4. Briefly returning to the derivative of the Q as function of length in equation (7.32), observe that the derivative vanishes when $2R/L = 1$. This corresponds with a maximum value of the Q factor for the TE_{011} mode. A plot of the Q as a function of the diameter-to-length ratio for our aluminum cavity is shown in figure 7.5.

Let us continue with the calculation of the derivative of $U_0(L)$ with respect to L,

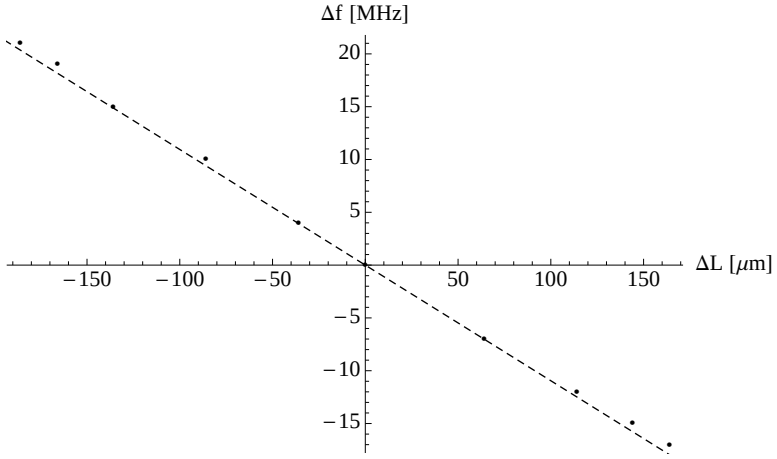

Figure 7.3: Experimental results for when the length of an aluminum RF cavity was varied via a end-piston attached to a micrometer. The dashed line is a linear fit to $\Delta f = a\Delta L$, with $a = -110$ Hz/nm which is within 6% of the theoretical expected value of -104 Hz/nm.

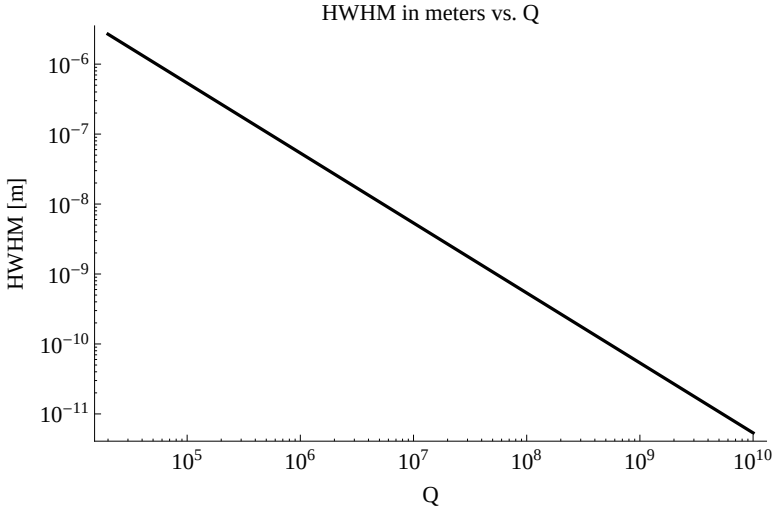

Figure 7.4: Log-Log plot of equation (7.36) plotted as a function of cavity Q factor. With Q's on the order of $Q_0 \sim 10^9$ the cavity's length need only to change by 54 pm to reduce the stored energy by half.

from equation (7.27)

$$\frac{\partial U_0}{\partial L} = \frac{4P_f\omega^2}{\left(4\omega^2\frac{\omega_0^2}{Q_0} + Q_0(\omega^2-\omega_0^2)^2\right)^2} \times \left\{\partial_L\omega_0\left(4\omega\frac{\omega_0^2}{Q_0} + Q_0(\omega^2-\omega_0^2)\right)\right.$$
$$\left. -\omega_0\left(4\omega^2(\frac{2\omega_0\partial_L\omega_0 Q_0 - \omega_0^2\partial_L Q_0}{Q_0^2}) + (\omega^2-\omega_0^2)^2\partial_L Q_0 + 4Q_0\omega_0(\omega^2-\omega_0^2)\partial_L\omega_0\right)\right\}, \tag{7.37}$$

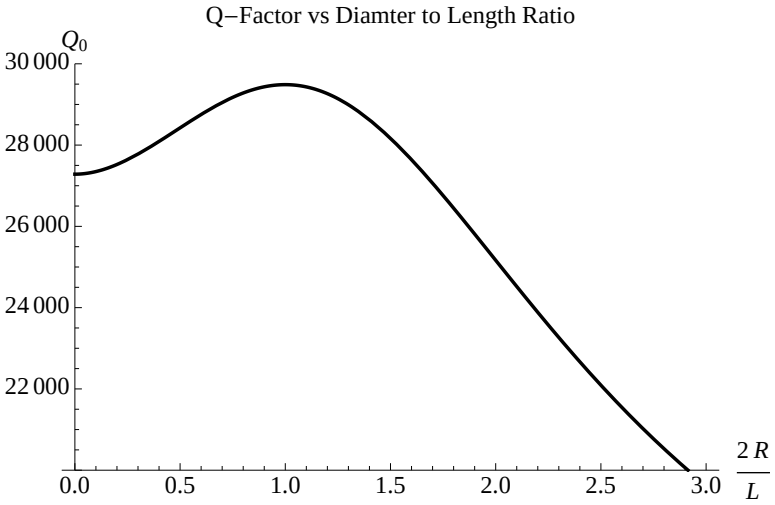

Figure 7.5: The Q factor of an aluminum cavity as a function of the diameter to length ratio. The maximum occurs at $2R = L$. For our aluminum cavity $2R/L = 1.41$.

where the short hand notation $\partial_L \equiv \partial/\partial L$ is introduced, and the derivatives of ω_0 and Q_0 are given by equations (7.31) and (7.32), respectively. Substituting the results from equations (7.27),(7.28), (7.29), (7.31), and (7.32) into equation (7.25) gives and explicit expression for the averaged force per unit area exerted at the boundary of a microwave cavity in terms of the variable cavity length L. This result for our aluminum cylindrical cavity excited in a TE_{011} mode at $\omega = 11.1$ GHz is plotted in figure 7.6a. The gradient of the radiation pressure which leads to an expression for the optical spring constant is calculated using the same results in equation (7.26). The result is plotted in figure 7.6b for our aluminum cavity.

From the figure 7.6a it is clear that the maximum force experienced by the end-boundary occurs when the cavity's length is tuned to resonance, this is expected since the energy stored in the cavity peaks at this point. Note that we have used a value of $Q_0 \sim 3 \times 10^4$, otherwise the FWHM would be to small to resolve in the plot. Observed that the gradient in figure 7.6b, which can be defined an effective non-linear spring constant

$$\frac{\partial < T_{zz} >}{\partial L} \equiv K_{\mathrm{eff}}(L), \tag{7.38}$$

has two maximum peaks of opposite sign. This result is analogous to that of the previous section where the effective optical spring constant in a Fabry-Perot with a

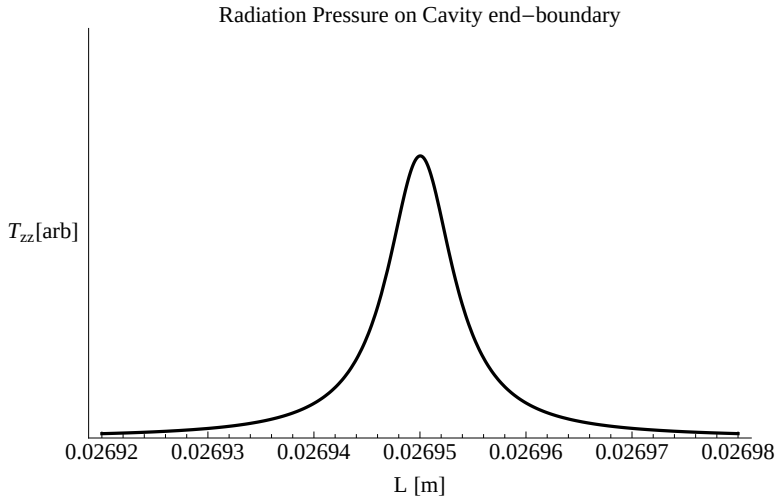

(a)

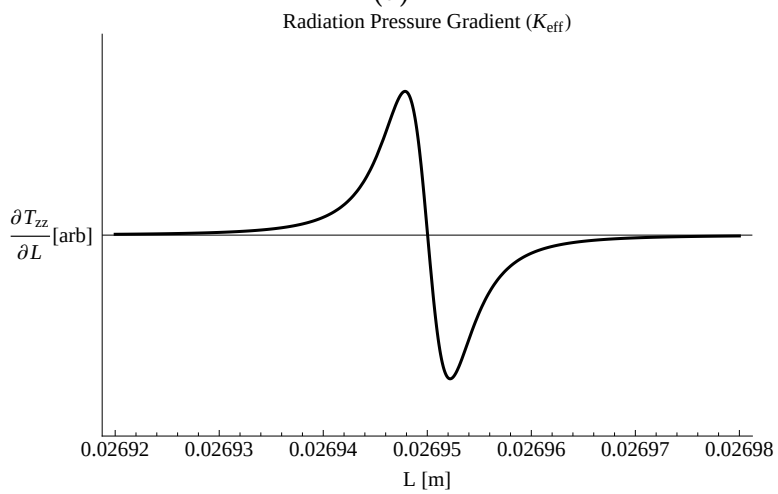

(b)

Figure 7.6: (a) The radiation pressure on the end-boundary of a cylindrical cavity as a function of the length while the excitation frequency is kept constant. (b) The gradient of the radiation pressure leads to an effective spring constant which creates damping as the end-boundary is displaced.

moving end-mirror was derived. The full explicit expression for $K_{\text{eff}}(L)$ can be expressed with the aid of the previous equations, however, the result is cumbersome. Since we have verified that the microwave system behaves like the Fabry-Perot system, let us use the same technique used in the FP for the the estimate of $K_{\text{eff}}^{\max}$. From equations

(7.36), and (7.25)

$$|K_{\text{eff}}^{\max}| \approx \frac{\Delta < T_{zz} >}{\Delta L_{1/2}} = \frac{\pi}{16\lambda_{11}^2} \frac{Q_0 P_f c^2 R^2}{f_0^3 L_0^5 V_{\text{eff}}} J_1^2(\lambda_{11} r/R), \tag{7.39}$$

where

$$V_{\text{eff}} = \frac{\pi R^2 L_0 J_0^2(\lambda_{11})}{2} \left((\frac{\pi R}{\lambda_{11} L_0})^2 + 1 \right) \text{ for the TE}_{011} \text{ mode,} \tag{7.40}$$

R is the radius, L_0 is the length of the cavity, f_0 is the resonant frequency, c is the speed of light, P_f is the forward traveling power, $\lambda_{11} = 3.8317$, and $\Delta < T_{zz} > \approx < T_{zz} > /2$. Note that this spring constant is defined per unit area, and one must integrate over the Bessel function along the surface of the end-boundary to obtain a total quantity.

Finally, it is important to point out the regime in which the effective spring constant in equation (7.39) holds. As in the Bragisnky calculation in which the optical fields are of much higher frequency than the motion of the end-boundary (mirror or membrane in our case), here we also require that the frequency of motion be significantly less than that of the electromagnetic fields. Indeed, this was an implicit assumption as the time average was taken at the start of the calculation. In the case where the mechanical resonance is close to the frequency of the electromagnetic fields a more careful analysis must be done as phase factors will become important.

7.3 Practical Considerations for Microwave Cavity Optomechanics

As discussed in chapter 2 the major components required for a cavity microwave parametric amplifier are; 1) A high-Q high-frequency mechanical oscillator, 2) high-Q cavity with a thin superconducting film at its end-boundary, 3) and high-Q cavity with a closely spaced dual-peak resonance spectrum. We have already discussed how one might accomplish requirements 1 and 2 above (see section 2, now we provide motivation on how one might accomplish requirement 3 in practice.

In the double Fabry-Perot (FP) cavity discussed in section 2.3 it was shown that placing a mirror at the center of a Fabry-Perot causes a splitting on the spectrum that is related to the reflection coefficient of the middle mirror. The frequency spacing of the splitting must be less than the free spectral range (FSR) of the long FP cavity for

a mirror with a reflection coefficient between zero and unity. In general, the higher the reflection coefficient the more closely spaced the dual spectrum becomes. Physically this must be the case because as the reflection coefficient approaches unity, the double Fabry-Perot approaches two independent single Fabry-Perot cavities with a single resonance peak. Alternative, as the reflection coefficient approaches zero, the frequency spacing becomes equal to the FSR of the long FP resulting in a single peak FP with a larger FSR. It is of interest to obtain a similar relation for a "double" microwave cavity scheme. Although the analysis preform by Stadt and Muller [22], which was verified by Hogeveen and Stadt [23], was done for an optical light Fabry-Perot, insight can be gained for the "double" microwave cavity scheme.

The physical mechanism that generates a splitting when a barrier is introduced at the center of a resonant electromagnetic wave cavity[1] is the sloshing of energy from one side of the cavity to the other. To picture this concept in a clear fashion imagine an hourglass[2] where the amount of time it takes for the sand to completely transfer from one chamber to another is related to the size of the hole coupling the two sides. In this sense, a larger hole corresponds to a smaller reflection coefficient or larger transmission coefficient[3]; that is, the bigger the hole the faster the transfer and vice versa. In a similar fashion the reflection coefficient in a barrier placed at the center of an electromagnetic cavity governs the transfer of energy from one half to the other. With this analogy it is somewhat easy to see that as the reflection coefficient becomes smaller (hole in hourglass becomes larger) the time it takes energy to slosh between cavities becomes smaller (time of transfer in hourglass) leading to a larger frequency splitting. Similarly, as the reflection coefficient grows larger the time for the transfer of energy between cavities becomes larger and the frequency splitting becomes smaller.

Although the frequency splitting calculations have been done specifically for the case of a double FP cavity [22], it is not completely unphysical to apply this (cautiously) to a "double" microwave cavity scheme. Formally, the motivation stems from the versatility of Maxwell's equations and the definition of the reflection coefficient related strictly to

[1]This also happens in Quantum Mechanics for a "particle in a box" when a finite potential barrier is introduced at the center of the box, and for that matter more generally in any dual cavity where resonant wave solutions exist and a reflection coefficient can be defined.

[2]The concept of wave reflection is being ignored, one should not take this analogy to literal, but instead just for the sake of clarity.

[3]This analogy works best with a transmission coefficient.

the field amplitudes. Differences might occur in the phase factors associated with the waves and mode factors associated with the shape of the electromagnetic modes.

7.3.1 Reflection Coefficient from Aperture in a Cylindrical Waveguide

In this section we calculate the reflection coefficient of a thin circular aperture placed in a cylindrical waveguide excited with a TE_{01} mode. We point out that the effects of apertures placed on waveguides have been studied in great detail for dominant propagating modes [55], TE_{11} in the case of a cylindrical waveguide. The analysis is based on the scattered amplitude calculation and aperture coupling theory [56, 57]. The theory is based on the approximation that the field in the region of a small aperture can be approximated by electric and magnetic dipole moments and was originally developed by Bethe [58]. This approximation holds in the regime where the aperture's resonant frequency is at least three times the operating waveguide frequency. However, in the regime where the aperture's resonant frequency becomes comparable with the operating frequency as occurs when the aperture becomes larger, Foster's reactance theorem can be applied to add an appropriate frequency correction factor [59].

In general the field amplitude of the n^{th} right and left traveling radiated mode is given by [56]

$$C_n^+ = \frac{i\omega I}{P_n}\int_S \vec{B}_n^- \cdot \vec{n} dS \quad \text{and} \tag{7.41}$$

$$C_n^- = \frac{i\omega I}{P_n}\int_S \vec{B}_n^+ \cdot \vec{n} dS, \tag{7.42}$$

respectively. Here P_n is a normalization factor given by

$$P_n = 2\int_S \vec{e}_n \times \vec{h}_n \cdot \hat{z} dS, \tag{7.43}$$

where e and h are defined as the transverse field amplitudes, and the integrals are over the area of the loop. For a cylindrical waveguide excited in a TE_{01} mode

$$e_\phi \equiv J_0'(k_c r), \quad \text{and} \tag{7.44}$$

$$h_r \equiv -Y_{TE} J_0'(k_c r), \tag{7.45}$$

where Y_{TE} is the waveguide's characteristic admittance, and $k_c = \lambda_{11}/R$. For our

normalization of the TE_{01} mode fields (defined below) we find

$$P_1 = -2\int\int e_\phi h_r r dr d\phi = 4\pi Y_{TE} R^2 \int_0^1 J_1^2(3.8317x)x dx. \tag{7.46}$$

In the approximation that the hole is sufficiently small so that the field in the region can be considered constant, equations (7.41) and (7.42) become

$$C_n^+ = \frac{i\omega}{P_n}\vec{B}_n^- \cdot \vec{M}, \quad \text{and} \tag{7.47}$$

$$C_n^- = \frac{i\omega}{P_n}\vec{B}_n^+ \cdot \vec{M}, \tag{7.48}$$

where M is magnetic dipole moment of the loop formed by the circular aperture. The aperture will effectively behave like two superposed magnetic moments, one which radiates back into the input waveguide and the other which radiates towards the output waveguide, the moments are [56]

$$\vec{M} = +\alpha_m[\vec{H}_{g1} + \vec{H}_{d1} - \vec{H}_{d2}]_t, \quad \text{and} \tag{7.49}$$

$$\vec{M} = -\alpha_m[\vec{H}_{g1} + \vec{H}_{d1} - \vec{H}_{d2}]_t, \tag{7.50}$$

respectively. Here $\alpha_m = 4r_0^3/3$ is the magnetic polarizability of a circular aperture of radius r_0, $\vec{H}_{g1}$ is the generator field, $\vec{H}_{d1}$ is the dominant mode field radiated by the dipole back to the input waveguide, and $\vec{H}_{d2}$ is the dominant mode field radiated by the dipole to the output waveguide. For a TE_{01} mode the relevant fields in the left half of a cylindrical waveguide with a circular aperture placed at $z = 0$ are

$$E_\phi = C(e^{i\beta z} - e^{i\beta z})J_0'(k_c r), \quad \text{and} \tag{7.51}$$

$$H_r = -C(e^{i\beta z} + e^{i\beta z})J_0'(k_c r). \tag{7.52}$$

Observe that these are the field modes of a cylindrical waveguide with no aperture, and we have choosen a normalization consistent with (7.44) and (7.45). It is also required that the tangent electric field vanish at the surface of the aperture ($z = 0$), but not the tangent component magnetic field. The radiated fields in the region $z > 0$ are assumed

to have the same mode shape but different amplitudes

$$E_\phi^+ \equiv Ae^{-i\beta z}J_0'(k_c r) = Ae_\phi e^{-i\beta z}, \quad \text{and} \tag{7.53}$$

$$H_r^+ = -AY_{TE}e^{-i\beta z}J_0'(k_c r) = Ah_r e^{-i\beta z}. \tag{7.54}$$

The amplitude A is found from equation (7.47) and $B_{01}^- = -\mu_0 h_r$

$$A = \frac{i\omega}{P_{01}}(-\mu_0 h_r)(2M), \tag{7.55}$$

where we have slightly modified the subscript notation to coincide with the notation for a TE_{01} mode, and the factor of two in the magnetic dipole moment is due to the superposition of the radiated fields into the input and output waveguide. The magnetic moment (M) follows from the field expression at the aperture boundary ($z = 0$),

$$H_{g1} = -2CY_{TE}J_0'(k_c r), \tag{7.56}$$

$$H_{d1} = AY_{TE}J_0'(k_c r), \quad \text{and} \tag{7.57}$$

$$H_{d_2} = -AY_{TE}J_0'(k_c r), \tag{7.58}$$

we find

$$M = -\alpha[-2CY_{TE}J_0' + 2AY_{TE}J_0']. \tag{7.59}$$

From equation (7.45), (7.46), (7.55) and M above, the amplitude A follows as

$$A = \frac{\frac{i\beta(J_0'(k_c r))^2\alpha_m}{\pi R^2 \int_0^1 J_1^2(3.8317x)xdx}}{1 + \frac{i\beta(J_0'(k_c r))^2\alpha_m}{\pi R^2 \int_0^1 J_1^2(3.8317x)xdx}}C. \tag{7.60}$$

To associate this with a reflection coefficient note that the back-radiated field in the region $z < 0$ is given by

$$E_\phi^- = AJ_0'(k_c r)e^{i\beta z}, \tag{7.61}$$

where by symmetry A is given by equation (7.60). It is then follows that the ratio A/C

can be identified with a amplitude transmission coefficient T,

$$\frac{A}{C} \equiv T = \Gamma + 1, \tag{7.62}$$

where Γ is the amplitude reflection coefficient. It is well known that an aperture in a waveguide leads to a shunt susceptance B [56, 57]. For a lossless waveguide with a shunt subsceptance the reflection coefficient is [57]

$$S_{11} = \Gamma = -\frac{i\bar{B}}{2 - i\bar{B}}, \tag{7.63}$$

where the bar in $\bar{B}$ is used to denote the normalized susceptance. Comparing equations (7.60), (7.62), and (7.63) we find

$$\frac{1}{\bar{B}} = -\frac{1}{2}\frac{\beta(J_0'(k_c r))^2 \alpha_m}{\pi R^2 \int_0^1 J_1^2(3.8317x)xdx}, \tag{7.64}$$

where β is the propagation constant. From equations (7.63) and (7.64) above, the magnitude of the reflection coefficient is

$$|\Gamma| = \frac{\bar{B}}{\sqrt{4 + \bar{B}^2}}. \tag{7.65}$$

For our cylindrical cavity dimensions ($R = 1.905$cm) at 11.1 GHz, noting that $\int_0^1 J_1^2(3.8317x)xdx = .08118$, and assuming the aperture is placed at $r = 48\%R$ so that $(J_0'(k_c r))^2 = J_1^2(k_c r) = .3386$ we find

$$|\Gamma| = \frac{1}{\sqrt{1 + 3.24 \times 10^{-7} r_0^6[\text{mm}]}} \tag{7.66}$$

where $\alpha_m = 4r_0^3/3$, and r_0 is in millimeters. A plot of equation (7.71) is illustrated in figure 7.7. It is important to keep in mind that this result is in the approximation that the aperture is small so that the field in the region of the aperture remains constant. In addition, the resonant frequency of the aperture has been assumed to be at least three times more than the operating frequency of 11.1 GHz. Furthermore, from this analysis it is clear that placing a small aperture at the center or the waveguide ($r = 0$) will result in a reflection coefficient of zero, hence, no coupling can be achieved. We conclude that the aperture must be placed at a point where the tangent magnetic field

does not vanish.

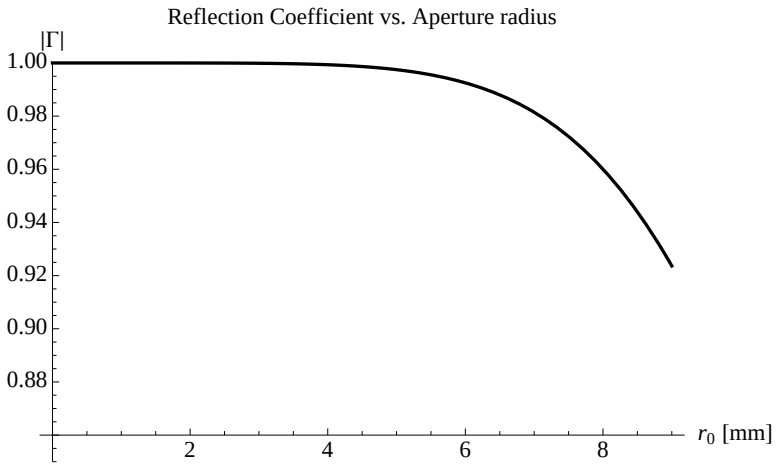

Figure 7.7: Reflection coefficient of a small thin circular aperture placed a $r = 48\%R$ in a circular waveguide

For the case of a bigger aperture Foster's reactance theorem adds a frequency correction factor to the normalized susceptance [59]

$$\bar{B} \to \bar{B}\left(1 - \left(\frac{f}{f_0}\right)^2\right), \tag{7.67}$$

where f_0 is the resonant frequency of the aperture, and f is the operating frequency. Although the resonant frequency of the aperture is best found by experimental measurement, we illustrate a sample calculation of this correction factor under the lose assumption that the resonant frequency of the aperture is on the order of the cutoff frequency of a waveguide with the same radial dimensions. It is important to point out that in general this is not the case, but in cases where a large aspect ratio exist this might be feasible [60]. Adding the correction factor in equation (7.71) we find

$$|\Gamma| = \left[\sqrt{1 + \frac{3.24 \times 10^{-7} r_0^6[\text{mm}]}{(1 - 3.69 \times 10^{-3} r_0^2[\text{mm}])^2}}\right]^{-1}, \tag{7.68}$$

where we have approximated $f_0 \approx f_c = .693c/r_0$ the cutoff frequency for the TE_{01} mode of a cylindrical waveguide with radius r_0. A plot of this modified reflection coefficient is illustrated in figure 7.8. The correction factor results in a much faster decay of the reflection coefficient as the aperture radius increases. Experimentally,

the behavior should be the same as that described here with the exception of some numerical corrections.

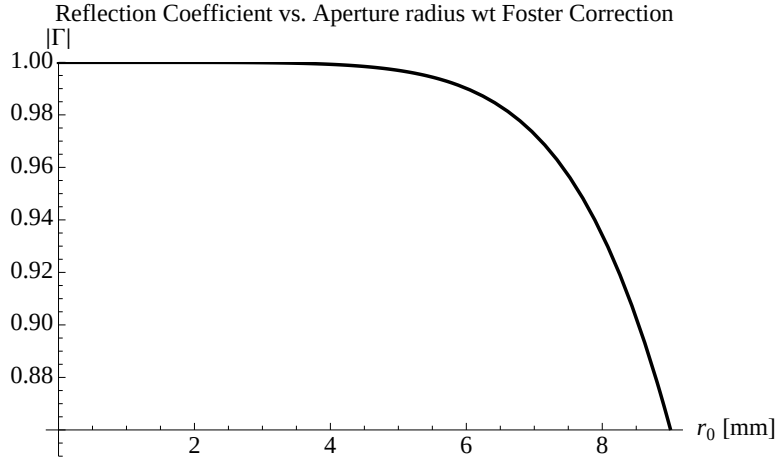

Figure 7.8: Reflection coefficient with Foster correction as a sample calculation with the approximation that the aperture resonant frequency is on the order of the cutoff frequency.

7.4 Frequency Splitting Measurements in a Dual RF Cavity with Aperture

Experiments were preformed to test results discussed in section 7.3.1, in which the reflection coefficient generated by a circular iris placed at the center of a dual RF cavity creates a frequency splitting. The circular apertures (irises) were placed between two aluminum cylindrical cavities at a radius equal to 48% the radius of the cavity (point of peak field for TE_{011} mode) as illustrated in figure 7.9. Several irises were constructed, S21 transmission measurements were preformed with an HP 8720C network analyzer. Figures 7.10a-7.10g summarized the measurements obtained when different sized apertures located at the bisection of the two cavities at a radius equal to 48% the radius of the cavity where used to generate frequency splittings ranging from 4-83 MHz. It is observed that the quality factors becomes asymmetric for the larger frequency splittings. This effect might be due to frequency tuning limitations associated with our aluminum cavity set up, and it is believed that this effect can be corrected. Further test with cavities that have the proper tuning mechanisms should confirm this speculation.

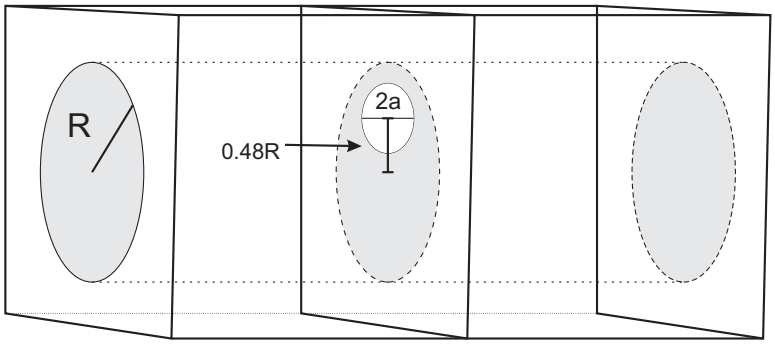

Figure 7.9: Dual RF cavity configuration with a circular aperture (iris) placed at a radius equal to 48% the radius of the cavity.

The double Fabry-Perot scheme is used as a model to generate an empirical relation for the frequency splitting as a function of aperture radius. The motivation for this model is due to the versatility of Maxwell equations along with the definition of the reflection coefficient involving only the field amplitudes. As discussed in section **??** for a double Fabry-Perot, the frequency splitting is given by

$$\Delta f = \frac{c}{2\pi L}(\pi - 2\phi), \tag{7.69}$$

where

$$\phi = \frac{1}{2}\arccos\left(-r_2\frac{(1+r^2)}{2r}\right), \tag{7.70}$$

L is the length from one mirror to the next (assumed to be the same for both cavities), r is the reflection coefficient of the end-mirrors, and r_2 is the reflection of the middle mirror. In this model the frequency splitting should be of the form given by equations (7.69), and (7.70), but with identification that r_2 is given by the reflection coefficient of the circular iris $|\Gamma|$. That is,

$$r_2 \equiv |\Gamma| = \left[\sqrt{1 + \frac{dx^6}{(1-bx^2)^2}}\right]^{-1}, \tag{7.71}$$

where d and b are treated as fit parameters to allow for correction factors, and x is the radius of the iris in units of millimeters. Hence, we speculate that the frequency splitting as a function of the reflection coefficient should fit an empirical relation of the

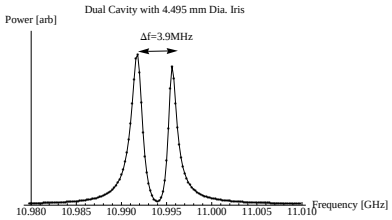

(a) 3.9 MHz splitting of the TE_{011} resonance with an iris of 4.495 mm in diameter.

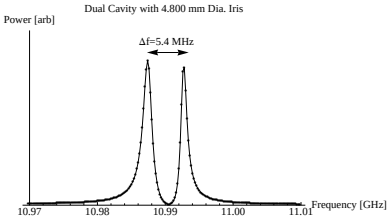

(b) 5.4 MHz splitting of the TE_{011} resonance with an iris of 4.8 mm in diameter.

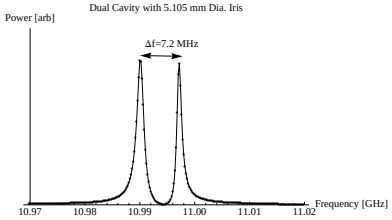

(c) 7.2 MHz splitting of the TE_{011} resonance with an iris of 5.105 mm in diameter.

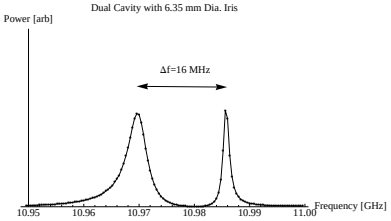

(d) 16 MHz splitting of the TE_{011} resonance with an iris of 6.35 mm in diameter.

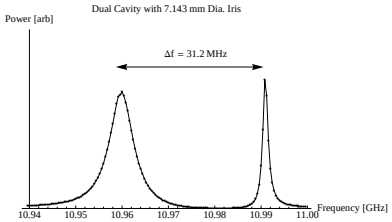

(e) 31.2 MHz splitting of the TE_{011} resonance with an iris of 7.143 mm in diameter.

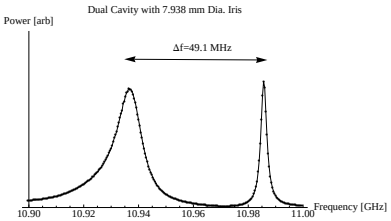

(f) 49.1 MHz splitting of the TE_{011} resonance with an iris of 7.938 mm in diameter.

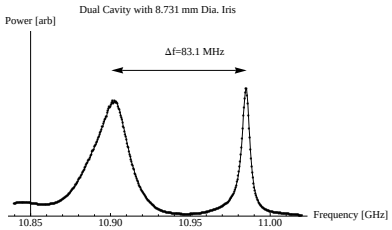

(g) 83.1 MHz splitting of the TE_{011} resonance with an iris of 8.731 mm in diameter.

Figure 7.10: Experimental results for the dual RF cavity frequency splitting

form

$$\Delta f = 1771g \left\{ \pi - \arccos \left[-\frac{1+r^2}{2r} \left(\sqrt{1 + \frac{dx^6}{(1-bx^2)^2}} \right)^{-1} \right] \right\}, \qquad (7.72)$$

where r is left as a fit parameter, and g is a fit parameter to compensate for the

correction factor associated with the phase length of the cavity. The experimental results fit the model extremely well as shown in figure 7.11, and suggest that the same physical mechanism that leads to a splitting in the Fabry-Perot also leads to splitting in RF cavities. The fit yields $r = .99999$, $b = .008175$, $g = 1.166$, and $d = 5.21 \times 10^{-10}$.

.

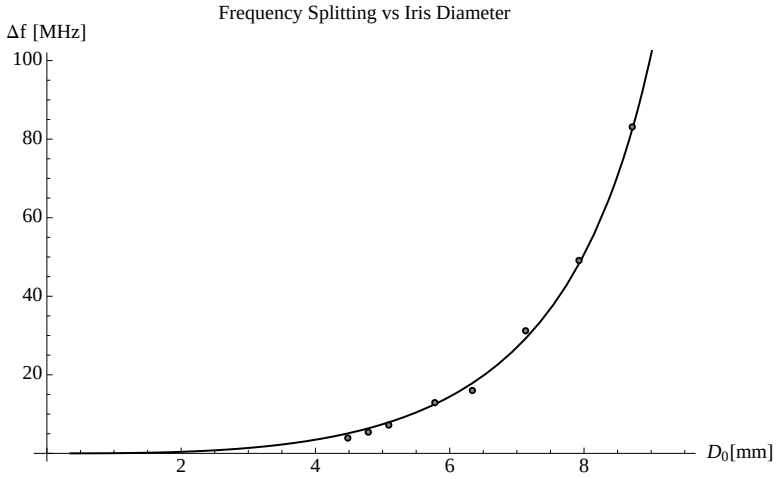

Figure 7.11: For an empirical relation we model the splitting as that of a double Fabry-Perot cavity. However, we take the reflection coefficient to be given by equation (7.71). Solid curve is a fit to equation (7.72), circles represent the data points obtained from above figures.

Finally, we add that similar test with a bisecting wire placed at the point of maximum electric field in a cylindrical cavity of length $L = 1.284$" and diameter $D = 1.02$" excited with a TE_{112} mode at 11.42 GHz displayed similar frequency splitting effects. A S21 transmission measurement, preformed with the HP 8720C network analyzer, shows the resonance of the TE_{112} mode at approximately 11.50 GHz, see figure 7.12a. A splitting is observed by placing a copper wire at the midpoint of the cavity, perpendicular to the axial direction and parallel to the input coupler. The splitting is approximately 400 MHz.

7.5 Optomechanics with cm-sized Microwave Cylindrical Cavities

We present a simple scheme in which cavity optomechanics may be achieved with cm-scale three-dimensional architectures. The major premise this thesis has been to

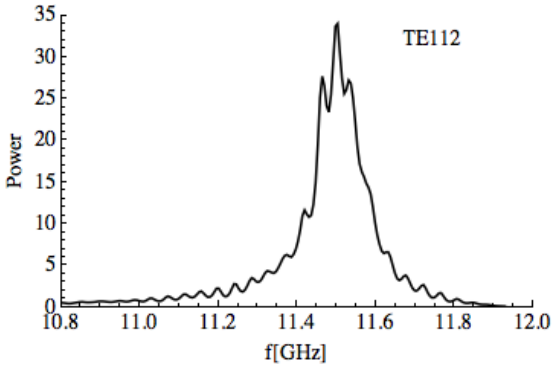

(a) Cylindrical cavity TE_{112} resonance at 11.50 GHz.

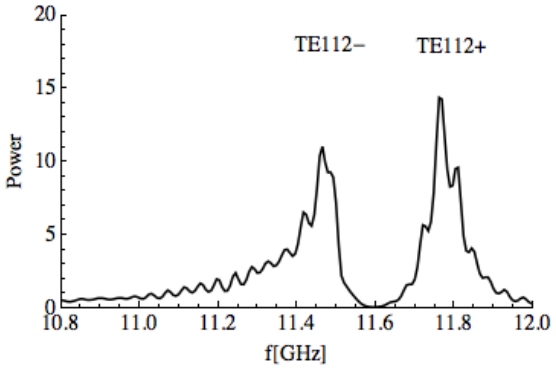

(b) Splitting of the TE_{112} mode in cylidrical cavity with a bisecting copper wire at its mid-point perpendicular to the axial direction and parallel to the input coupler. The Splitting in on the order of 400 MHz.

Figure 7.12: S21 transmission measurements (a) of a copper cavity with TE_{112} resonant frequency at 11.5 GHz and (b) splitting due to the placement of copper wire placed at the center. The vertical axes use the same arbitrary power reference in the conversion from logarithmic to linear scale.

show that the same effects and mechanism used in optical cavity optomechanics can be transferred to cm-size systems using high-Q SRF cavities with cm-sized mechanical oscillators. The key finding is that the small frequency splittings (section 7.4 in dual RF cavity systems on the order mega-Hertz frequencies may be used in combination with the ponderomotive effects experienced by a mechanical oscillator, whose surface is coated with thin SC film, to assemble a cm-sized RF cavity optomechanical system. Such a system can then be used for frequency up or down conversion of microwave frequency light and parametric oscillation of the mechanical oscillator. Furthermore,

we simply note that parametric oscillators/amplifier for microwave frequencies might also be feasible via this scheme.

7.5.1 Parametric mechanical oscillation and side band generation via microwave optomechanics

As example of how such a system may be realized, consider figure 7.13 in which a triple cavity scheme is employed. The right side consist of a dual RF cavity with a 1 MHz resonance splitting in which a pump beam may be injected at the upper resonance. The left cavity plays the role of an effective mechanical oscillator with a resonance frequency of 1MHz and $Q \sim 10^4$. The interaction of the pump beam with the mechanical oscillator will lead to a "Stokes"-like generated sideband (frequency down converted) which coincides with the lower resonance, 1 MHz away, of the dual RF cavity. The feedback do to the resonance at the "Stoke" mode frequency will in-turn amplify (parametrically) the motion of the mechanical oscillator, which in-turn generate more "Stokes" light, and so on. Hence, leading to parametric oscillation of the mechanical oscillators, and sideband generation. The threshold for oscillation of such a system is estimated analogously as for the "Brangisky" [26] case,

$$P_f > \frac{mL^2\Omega^2\omega_p}{2\Lambda^2 Q_1 Q_m Q_p}, \tag{7.73}$$

where P_f is the forward traveling power (perfect coupling assumed), $\Omega \sim 2\pi \times 1$ MHz is the effective frequency of the mechanical oscillator, $\omega_p \sim 2\pi \times 11$ GHz is the frequency of the pump, $m \sim 2$ μg is the mass of the oscillator, L 5 cm is the length of the dual cavity, $Q_p \sim 10^9$ is the Q factor of the pump resonance in the dual cavity, $Q_1 \sim Q_p$ is the Q factor of the sideband resonance in the dual cavity, $Q_m \sim 10^4$ is the effective Q of the mechanical oscillator, and $\Lambda \sim 1$ is a numerical factor to account for the shape of the interacting mechanical and electromagnetic modes. We find

$$P_f > 20\mu \text{ W}. \tag{7.74}$$

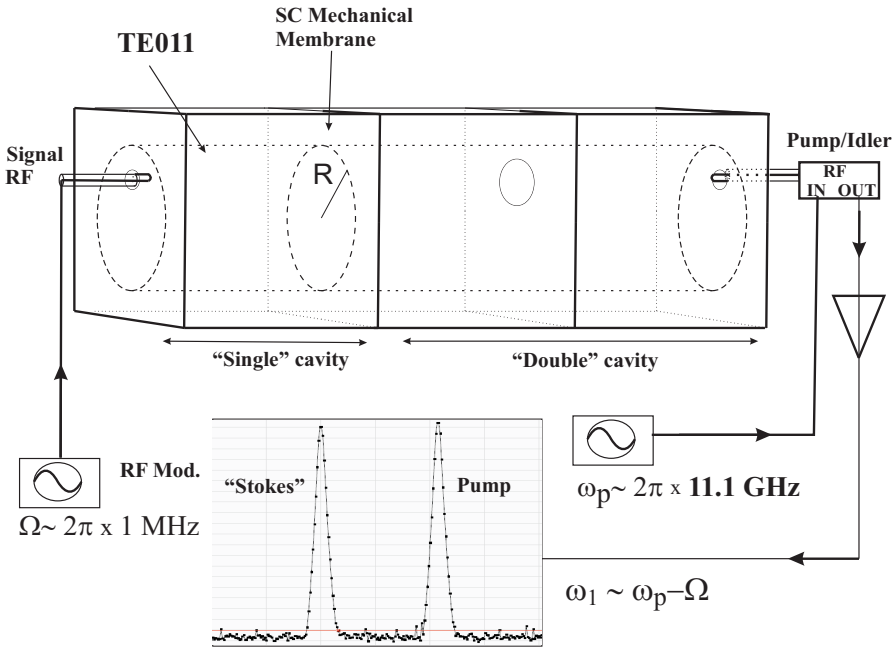

(a) Suggested scheme for a cm-sized microwave cavity optomechanical system. Description in text.

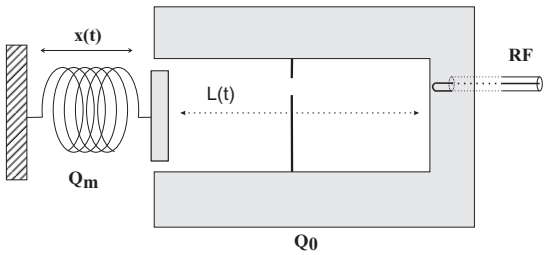

(b) Equivalent representation of the microwave optomechanical system that is to be compared with commonly used optical systems.

Figure 7.13: A cm-sized microwave optomechanical system.

References

[1] A.D. O'Connell and M. Hofheinz and m. Ansmann and R. C. Bialczak and M. Lenander and Erik Lucero and M. Neeley adn D. Sank and H. Wang and M. Weides and J. Wenner and J. M. Martinis and A. N. Cleland. *Nature*, **464**:697–703, 2010. iv, 2, 4

[2] Florian Marquardt and S. M. Girvin. *arXiv:0905.0566v1*, 2009. 2

[3] K. Børkje and S. M. Girvin. *New J. of Phys.*, **14**, 2012. 2, 76

[4] J. D. Thompson, B. M. Zwickl, A. M. Jayich, Florian Marquardt, S. M. Garvin, and J. G. E. Harris. *Nature*, **452**:72–75, 2008. 2

[5] A. Bruchhausen, R. Gebs, F. Hudert, D. Issenmann, G. Klatt, A. Bartels, O. Schecker, R. Waitz, A. Erbe, E. Scheer, J. R. Huntzinger, A. Mlayah, and T. Dekorsy. **Subharmonic resonant optical excitation of confined acoustic modes in a free standing semiconductor membrane at GHz frequencies with a high repetition rate femtosecond laser**. *Phy. Rev. Lett.*, **106**:077401, 2011. 2

[6] D. Hatanaka, I. Mahboob, K. Onomitsu, and H. Yamaguchi. **A phonon transistor in an electromechanical resonator array**. *App. Phy. Lett.*, **102**:213102, 2013. 2

[7] T.A. Palomaki, J.D. Teufel, R.W. Simmonds, and K.W. Lehnert. **Entangling mechanical motion with microwave fields**. *Science*, **342**(6159):710–713, 2013. 2

[8] T. Bagci, A. Simonsen, S. Schmid, L. G. Villanueva, E. Zeuthen, J. Appel, J. M. Taylor, A. Sørensen, K. Usami, A Schliesser, and E. S. Polzik. **Optical detection of radio waves through a nanomechanical transducer**. *Nature*, **507**:81–85, 2014. 2

[9] J.D. Teufel, T. Donner, Dale Li, J.W. Harlow, M. S. Allman, K. Cicak, A.J Sirois, J.D. Whittaker, K. W. Lehnert, and R. W. Simmonds. *Nature*, **475**:359–363, 2011. 2

[10] Jasper Chan, T. P. Mayer Alegre, Amir H. Safavi-Naeini, Jeff T. Hill, Alex Krause, Simon Gröblacher, Markus Aspelmeyer, and Oskar Painter. *Nature*, **478**:89–92, 2011. 2

[11] B. H. Eom, P. K. Day, H. G. LeDuc, and J. Zmuidzinas. *Nature*, **8**:623–627, 2012. 2

[12] William B. Case. **The pumping of a swing from the standing position**. *Am. J. Phys.*, **64**(3), 1996. 2

[13] B. Piccoli and J. Kullkarni. **Pumping a swing by standing and squatting: Do Children pump time optimally?** *Control Systems, IEEE*, **25**(4):48–56, 2005. 2

[14] Michel E Marhic. *Fiber Optical Parametric Amplifiers, Oscillators and Related Devices*. Cambridge University Press, 1st ed., 2007. 3

[15] Amnon Yariv. *Quantum Electronics*. John Wiley & Sons, Inc., 1st ed., 1989. 3

[16] Thomas Corbitt, David Ottaway, Edith Innerhofer, Jason Pelc, and Nergis Mavalvala. **Measurement of radiation-pressure-induced optomechanical dynamics in a suspended Fabry-Perot cavity**. *Phys. Rev. A*, **74**:021802, Aug 2006. 4, 6

[17] Raymond Y. Chiao, Luis A. Martinez, Stephen J. Minter, and Alex Trubarov. **Parametric Oscillation of a Moving Mirror driven by radiation pressure in a Superconducting Fabry-Perot Resonator System**. *Phys. Scr.*, **T147**, 2012. 4, 5, 6

[18] R. Y. Chiao, R. Haun, N. Inan, B.-S. Kang, S. J. Minter L. A. Martinez, G. Munoz, and D. Singleton. **A Gravitational Aharonov-Bohm effect and its connection to parametric oscillators and gravitational radiation**. *arXiv 1301.4270*, 2013. 4

[19] **Quantum Optomechanics—Throwing a Glance**. *J. Opt. Soc. Am. B*, **27**(A189), 2010. 5

[20] T. J. Kippenberg, H. Rokhsari, T. Carmon, A. Scherer, and K. J. Vahala. **Analysis of Radiation-Pressure Induced Mechanical Oscillation of an Optical Microcavity**. *Phys. Rev. Lett.*, **95**:033901, Jul 2005. 6

[21] S. Gigan, H.R Bohm, M. Paternostro, F. Blaser, G. Langer, J. B. Hertzberg, K.C Schwab, D. Bauerle, M. Aspelmeyer, and A. Zeilinger. **Self-cooling of a micromirror by radiation pressure**. *Nature*, **444**:67–70, 2006. 6

[22] H. van de Stadt and J.M. Muller. **Multimirror Fabry-Perot interferometers**. *Opt. Soc. Am. A*, **2**(8), 1985. 10, 11, 120

[23] **S.J. Hogeveen and Herman van de Stadt**. *Appl. Opt.*, **25**(22), 1986. 10, 120

[24] Frank L. Pedrotti, Leno M. Pedrotti, and Leno S. Pedrotti. *Introduction to Optics*. Addison-Wesley, 2006. 12

[25] M. J. Lawrence, B. Willke, M. E. Husman, E. K. Gustafson, and R. L. Byer. **Dynamic response of a Fabry-Perot interferometer**. *J. Opt. Soc. Am. B*, **16**(4):523–532, Apr 1999. 13, 16

[26] V.B. Braginsky, S.E. Strigin, and S.P. Vyatchanin. % bf Parametric oscillatory instability in Fabry-Perot interferometer. *Physics Letters A*, **287**(56):331 – 338, 2001. 13, 15, 16, 17, 131

[27] J. Cooper. **Scattering of Electromagnetic Fields by a Moving Boundary: The one Dimensional Case**. *IEEE Trans. Antennas Propaga.,*, **AP-28**(6), 1980. 13, 15

[28] M. Rakhmanov, R. L. Savage Jr, D. H. Reitze, and D. B. Tanner. **Dynamic resonance of light in Fabry-Perot cavities**. *Phys. Lett. A*, **305**:239–244, 2005. 16

REFERENCES

[29] H. Padamsee, J. Knoblock, and T. Hays. *RF Superconductivity for Accelerators*. Wiley-VCH Velag GmbH & Co. KGaA, Weinheim, 2008. 21, 53, 68, 72, 91

[30] V.B. Branginskii and A. B. Manukin. *Sov. Phys. JETP*, **25**:653, 1967. 22, 107, 111

[31] V.B. Branginskii, A. B. Manukin, and M. Yu. Tikhonov. *Sov. Phys. JETP*, **58**:1549–1552, 1970. 22, 107

[32] Werner Buckel and Reinhold Kleiner. *Superconductivity*. Wiley-VCH, 2004. 23

[33] Raymond Chiao. **Conceptual Tensions Between Quantum Mechanics and General Relativity**. *ArXiv*, **gr-qc/10208024v3**, 2002. 24

[34] C.P. Poole, H.A. Farach, R.J. Creswick, and R. Prozorov. *Superconductivity*. Superconductivity Series. Elsevier Science, 2010. 29, 30, 31, 32

[35] J. Bardeen, L. N. Cooper, and J. R. Schrieffer. **Microscopic Theory of Superconductivity**. *Phys. Rev.*, **106**:162–164, Apr 1957. 29

[36] J. Bardeen, L. N. Cooper, and J. R. Schrieffer. **Theory of Superconductivity**. *Phys. Rev.*, **108**:1175–1204, Dec 1957. 29

[37] R. E. Glover and M. Tinkham. **Conductivity of Superconducting Films for Photon Energies between 0.3 and** $40kT_c$. *Phys. Rev.*, **108**:243–256, Oct 1957. 31

[38] K. Fossheim and A. Sudboe. *Superconductivity: Physics and Applications*. Wiley, 2004. 32

[39] Jack W. Ekin. Oxford University Press Inc., New York, 2007. 33, 35

[40] Jonas Zmuidzinas. **Superconducting Microresonators: Physics and Applications**. *Annual Review of Condensed Matter Physics*, **3**(1):169–214, 2012. 35

[41] CA Regal and KW Lehnert. **From cavity electromechanics to cavity optomechanics**. *Journal of Physics: Conference Series*, **264**(1):012025, 2011. 35

[42] K. Yoshii, H. Yamamoto, K. Saiki, and A. Koma. **Superconductivity and electrical properties in single-crystalline ultrathin Nb films grown by molecular-beam epitaxy**. *Phys. Rev. B*, **52**:13570–13575, Nov 1995. 36

[43] J. H. Quateman. **Tc Suppression and critical fields in thin superconducting Nb films**. *Phys. Rev. B*, **34**:1948–1951, Aug 1986. 36

[44] M. S. M. Minhaj, S. Meepagala, J. T. Chen, and L. E. Wenger. **Thickness dependence on the superconducting properties of thin Nb films**. *Phys. Rev. B*, **49**:15235–15240, Jun 1994. 36

[45] S.I. Park and T.H. Geballe. **Tc depression in thin Nb films**. *Physica B+C*, **135**(13):108 – 112, 1985. 36

[46] I.G. Wilson, C.W. Schramm, and J.P. Kinzer. *Bell Syst. Tech. J.*, **25**, 1952. 43, 61, 70, 71

[47] Simon Ramo, John R. Whinnery, and Theodore Van Duzer. *Fields and Waves in Communication Electronics*. John Wiley & Sons, Inc., New York., 1965. 61, 62

[48] M. Reagor, H. Paik, G. Catelani, L. Sun adn C. Axline, E. Hollan, I. M. Pop, N. A. Masluk, T. Brecht, L. Frunzio, M. H. Devoret, L. Glazman, and R. J. Schoelkopf. **Reaching 10 ms single photon lifetimes for superconducting aluminum cavities**. *App. Phys. Lett.*, **102**(19):192604, 2013. 61

[49] J. C. Slater. *Microwave Electronics*. Van Nostrand, Princeton, N.J., 1950, p.81 et seq., 1950. 63

[50] Singiresu S. Rao. *Vibration of Membranes*, pages 420–456, 607–646,700–706. John Wiley & Sons, Inc., 2007. 74, 75, 76

[51] G. N. Watson. *A Treatise on the Theory of Bessel Functions, 2nd ed.* Cambridge University Press, 1966. 78

[52] P. K. Kthe, P. Puri, and M. R. Sch´aferkotter. *Partial Differential Equations and Mathematica*. Fla: CRC Press, 1997. 78

[53] Singiresu S. Rao. *Vibration of continuous systems*. John Wiley & sons, Inc. Hoboken, New Jersey, 2007. 79

[54] David J. Griffiths. *Introduction to Electrodynamics, 3rd ed.* Prentice-Hall, Inc. Upper Saddle River, New Jersey, 1999. 85

[55] N. Marcuvitz. *Waveguide Handbook*. McGraw-Hill Book Co. Inc.,, 1951. 121

[56] Robert E. Collin. *Foundations for Microwave Engineering*, page chp. 4. Jonh Wiley & Sons, Inc., 2001. 121, 122, 124

[57] Gary B. Eastham and Kai Chang. **Analysis and Closed-Form Solutions of Circular and Rectangular Apertures in te Transverse Plane of a Circular Waveguide**. *IEEE*, **39**(4):718–723, 1991. 121, 124

[58] H. A. Bethe. **Theory of Diffraction of Small Holes**. *Phys. Rev.*, **66**(7-8):163–182, 1944. 121

[59] Seymour B. Cohn. **Microwave Coupling by Large Apertures**. *I.R.E*, pages 696–699, 1952. 121, 125

[60] Seymour B. Cohn. **Determination of Aperture Parameters by Electrolytic-Tank Measurements**. *I.R.E*, pages 1416–1421, 1951. 125

Declaration

I herewith declare that I have produced this paper without the prohibited assistance of third parties and without making use of aids other than those specified; notions taken over directly or indirectly from other sources have been identified as such. This paper has not previously been presented in identical or similar form to any other domestic or foreign examination board.

The thesis work was conducted from 2008 to 2014 under the supervision of Professor Raymond Chiao at the University of California.

MERCED,